

# Luminosity Functions and Host-to-host Scatter of Dwarf Satellite Systems in the Local Volume

Scott G. Carlsten , Jenny E. Greene, Annika H. G. Peter , Rachael L. Beaton, and Johnny P. Greco, and Johnny P. Gr Department of Astrophysical Sciences, 4 Ivy Lane, Princeton University, Princeton, NJ 08544, USA; scottgc@princeton.edu Department of Physics, The Ohio State University, 191 W. Woodruff Ave., Columbus OH 43210, USA <sup>3</sup> Department of Astronomy, The Ohio State University, 140 W. 18th Ave., Columbus OH 43210, USA <sup>4</sup> Center for Cosmology and AstroParticle Physics (CCAPP), The Ohio State University, Columbus, OH 43210, USA The Observatories of the Carnegie Institution for Science, 813 Santa Barbara St., Pasadena, CA 91101, USA Received 2020 June 3; revised 2020 November 15; accepted 2020 November 30; published 2021 February 17

#### Abstract

Low-mass satellites around Milky Way (MW)-like galaxies are important probes of small-scale structure and galaxy formation. However, confirmation of satellite candidates with distance measurements remains a key barrier to fast progress in the Local Volume (LV). We measure the surface brightness fluctuation distances to recently cataloged candidate dwarf satellites around 10 massive hosts within D < 12 Mpc to confirm association. The satellite systems of these hosts are complete and mostly cleaned of contaminants down to  $M_g \sim -9$  to -10, within the area of the search footprints. Joining this sample with hosts surveyed to comparable or better completeness in the literature, we explore how well cosmological simulations combined with common stellar to halo mass relations (SHMR) match observed satellite luminosity functions in the classical satellite luminosity regime. Adopting an SHMR that matches hydrodynamic simulations, we find that the predicted overall satellite abundance agrees well with the observations. The MW is remarkably typical in its luminosity function among LV hosts. We find that the host-to-host scatter predicted by the model is in close agreement with the scatter between the observed systems, once the different masses of the observed systems are taken into account. However, we find significant evidence that the observed systems have more bright and fewer faint satellites than the SHMR model predicts, possibly necessitating a higher normalization of the SHMR around halo masses of  $10^{11} M_{\odot}$  or significantly greater scatter than present in common SHMRs. These results demonstrate the utility of nearby satellite systems in inferring the galaxy-subhalo connection in the low-mass regime.

Unified Astronomy Thesaurus concepts: Dwarf galaxies (416); Galaxy dark matter halos (1880); Galaxy distances (590); Luminosity function (942)

#### 1. Introduction

For over two decades, the satellites of the Milky Way (MW) have been an important testing ground for the  $\Lambda$ CDM model of structure formation. Within the last few years, hydrodynamic simulations have been able to resolve the formation of the bright MW "classical" ( $M_* \gtrsim 10^5 M_{\odot}$ ) satellites. Results from the APOSTLE (Sawala et al. 2016a), FIRE (Wetzel et al. 2016; Garrison-Kimmel et al. 2019), and NIHAO (Buck et al. 2019) projects have demonstrated that the inclusion of baryonic physics leads to simulated satellite systems that have satellite numbers and internal kinematics similar to observed satellites of the MW and M31. Together, this ensemble of results suggests baryonic resolutions of the long-standing "Missing Satellites" (Klypin et al. 1999; Moore et al. 1999) and "Too Big to Fail" problems (Boylan-Kolchin et al. 2011, 2012) that are associated with dissipationless dark-matter-only (DMO) simulations of structure formation.

In recent years, solutions to the "Missing Satellites" problem have shifted to determining what stellar to halo mass relation (SHMR) can reproduce the observed abundance of dwarf satellites of the MW and comparing that to the SHMR predicted from hydrodynamic simulations of galaxy formation. The SHMR is an important observational benchmark and can help refine the importance of the physical processes involved in dwarf galaxy formation (e.g., Agertz et al. 2020). While

SHMRs proposed in the literature reproduce the abundance of MW satellites and also appear to broadly agree with predictions from suites of hydrodynamic simulations (e.g., Garrison-Kimmel et al. 2014, 2017a), there is still significant uncertainty in the details of the SHMR over the mass regime of the MW classical satellites (Garrison-Kimmel et al. 2017a; Read et al. 2017; Wheeler et al. 2019).

However, by only considering the dwarf satellites of the MW (and sometimes M31), there is the risk of overtuning the models to reproduce the abundance and properties of the MW satellites. There is still no consensus on what a "normal" satellite system is and, thus, no way of ascertaining if the MW satellite system is abnormal. Therefore, there is a strong motivation to study the satellites of host galaxies other than the MW (and M31). We would be able to define, for the first time, what a "normal" satellite system is for MW-like galaxies. By probing MW analogs, the host-to-host scatter in the satellite systems can be quantified. The host-to-host scatter in observed satellite systems is sensitive to both the statistics of the DM subhalo populations around MW-like hosts and also to the stochasticity of galaxy formation on these small scales. Additionally, by broadening the range of properties spanned by the set of MW analogs, both in terms of mass and host environment, the effect of these on the satellite systems can be explored.

Despite considerable investment by a number of groups, the challenge of both identifying and confirming the low-mass companions of  $L^*$  hosts has limited such study. To date, only a

<sup>&</sup>lt;sup>6</sup> Hubble Fellow.

NSF Astronomy & Astrophysics Postdoctoral Fellow.

handful of galaxies have been surveyed at a level comparable to the classical satellites of the MW. These include M31 (McConnachie et al. 2009, 2018; Martin et al. 2016), M81 (Chiboucas et al. 2009, 2013), Centaurus A (Crnojević et al. 2014, 2019; Müller et al. 2015, 2017, 2019), M94 (Smercina et al. 2018), and M101 (Bennet et al. 2017, 2019, 2020; Danieli et al. 2017; Carlsten et al. 2019a).

Complementary to large-area searches of the nearest galaxies, the Satellites Around Galactic Analogs Survey (SAGA; Geha et al. 2017; Mao et al. 2020) characterized the bright ( $M_r < -12.3$ ) satellites of eight MW analogs at larger distances in the range 20 < D < 40 Mpc (i.e., beyond the Local Volume, LV). At these distances, SAGA is only sensitive to roughly the brighter half of the classical satellite regime. However, the full survey will include  $\sim 3$  times more hosts than are available out to 10 Mpc.

The early observational results suggest that the host-to-host scatter between satellite systems of nearby MW analogs is larger than anticipated by DMO ACDM simulations. More specifically, Geha et al. (2017) noted that the scatter in satellite richness between hosts appeared to be larger than that predicted from abundance matching (AM) applied to DMO simulations. In a focused study, Smercina et al. (2018) found only two satellites with  $M_V < -9$  in the inner projected 150 kpc volume around the MW analog M94 (compared to seven in this range found around the MW). They argue that common AM relations applied to the DMO results from the EAGLE Project (Schaye et al. 2015) produce too many satellites and have far too little scatter to explain M94's anemic satellite population. Smercina et al. suggest that significantly increasing the slope and scatter in the SHMR could explain M94's satellite system. However, Smercina et al. considered all observed satellite systems together as "MW analogs," whereas the different host stellar masses (and presumably halo masses) among the surveyed hosts will contribute to the observed scatter in satellite abundances. Thus, isolating the true host-to-host scatter requires carefully controlling for the observed host mass when comparing to simulations, which is one goal of the current paper. This requires a large sample of observed satellite systems, which we assemble for the first time.

Measuring distances to individual candidates is a major challenge in this work. Many more hosts have been surveyed for candidates (e.g., Kim et al. 2011; Park et al. 2017; Müller et al. 2018; Park et al. 2019; Byun et al. 2020) than have distance-confirmed satellite populations. For the systems with distance-confirmed satellites, the contamination from unrelated background galaxies can be quite high. Carlsten et al. (2019a) and Bennet et al. (2019) found that the contamination from of the candidate satellite catalog of Bennet et al. (2017) for M101 was  $\sim\!\!80\%$ . These contaminants will obfuscate the interpretation of host-to-host scatter in satellite number. While some science questions can be overcome by careful statistical subtraction of a background luminosity function (LF; e.g., Nierenberg et al. 2016), our goal is to study satellite systems that are fully confirmed with distance measurements.

In this paper, we use surface brightness fluctuations (SBFs) to confirm candidate satellites recently uncovered around nearby hosts in the LV in Carlsten et al. (2020a). SBF has been shown to be a very efficient distance measure for low surface brightness (LSB) dwarfs (e.g., Jerjen et al. 1998, 2000, 2001, 2004; Jerjen 2003; Mieske et al. 2007, 2006; Carlsten et al. 2019b). Carlsten et al. (2019b) determined that the SBF-based distances reproduced the tip of the red giant (TRGB) distances to dwarfs with  $\sim 15\%$ 

accuracy, even for  $\mu_0 \sim 26$  mag arcsec<sup>-2</sup> dwarfs. This precision is sufficient in the Local Volume (D < 12 Mpc), in almost all cases, to distinguish a candidate as a real satellite or a background galaxy. SBF measurements can be performed using the same ground-based data that was used to discover the candidate satellites, obviating the need for expensive follow-up (either Hubble Space Telescope, HST, or spectroscopic).

Using this much-expanded sample of cleaned satellite systems around the hosts in Carlsten et al. (2020a), we produce the LFs for low-mass satellites. We compare these LFs to each other, as well as drawing conclusions on the ensemble. We explore how well SHMRs applied to modern cosmological simulations reproduce the observed LFs for a total of 12 systems, a sample large enough to examine the host-to-host scatter. In a companion paper, Carlsten et al. (2020b), we explore the radial distributions of satellite systems and compare with simulations.

This paper is structured as follows: in Section 2 we describe the candidate sample and data reduction, in Section 3 we outline the SBF methodology used for our study, in Section 4 we derive an absolute SBF calibration for the r band, and in Section 5 we present our distance results. In Section 6, we collate all of the satellite systems currently surveyed in the LV. In Section 7 we introduce the simulations and models that we use to compare with the data, in Section 8 we discuss the results of the comparison, and, finally, we conclude in Section 9. Readers interested primarily in the analysis of the satellite systems and comparison with models can skip to Section 6.

#### 2. Data

The foundation of this paper is the catalog of candidate satellites from Carlsten et al. (2020a). Carlsten et al. (2020a) searched for candidate satellites around 10 massive primaries in the LV using wide-field, deep archival Canada–France–Hawaii Telescope (CFHT)/MegaCam imaging. The surveyed hosts are NGC 1023, NGC 1156, NGC 2903, NGC 4258, NGC 4565, NGC 4631, NGC 5023, M51, M64, and M104 (see Table 1 of Carlsten et al. for characteristics of these hosts). The area and surface-brightness completeness were heterogeneous, but several of the hosts were nearly completely surveyed within a projected radius of 150 kpc. Through careful mock recovery tests, we determine that we are complete at  $\gtrsim$ 90% for satellites down to  $\mu_{r,0} \sim$ 26–26.5 mag arcsec<sup>-2</sup>.

For the SBF measurements in this paper, we use the same archival CFHT/MegaCam (Boulade et al. 2003) imaging data as used by Carlsten et al. (2020a). Either g and r or g and i band imaging is used, depending on the availability in the CFHT archive. Exposure times are characteristically  $\sim 1$  hr in each of the bands. The data reduction follows that in Carlsten et al. (2020a), and we refer the reader to that paper for details.

Carlsten et al. (2020a) used the object-detection algorithm of Greco et al. (2018), which is specifically optimized for LSB galaxies, to detect 155 candidate satellite galaxies around these 10 hosts. While the detection algorithm focused on LSB galaxies, Carlsten et al. (2020a) also cataloged many high-surface-brightness candidates. We use the catalogs of Carlsten et al. (2020a) as the basis for the SBF analysis presented here. While most of the cataloged galaxies have no prior distance

 $<sup>^8</sup>$  However, the distance precision required to infer the three-dimensional location of a satellite within the host virial volume still necessitates HST.

information, some have redshifts and some even have TRGB distances. Where possible, we take these into account when determining the nature of a candidate. We refer the reader to Carlsten et al. (2020a) for the full catalogs of candidates.

## 3. SBF Methodology

In this section, we describe the methodology we use in the SBF analysis. We follow the procedure detailed in Carlsten et al. (2019b), which largely follows the usual SBF measurement process (e.g., Blakeslee et al. 2009; Cantiello et al. 2018). We briefly outline the important steps here. The analysis starts with modeling the smooth surface-brightness profile for each candidate. Then the amount of fluctuation in the brightness profile relative to the smooth profile is quantified. This quantity is expressed in terms of the apparent SBF magnitude. The absolute SBF magnitude for a certain stellar population is defined as

$$\bar{M} = -2.5 \log \left( \frac{\sum_{i} n_i L_i^2}{\sum_{i} n_i L_i} \right) + \text{z.p.}$$
 (1)

where  $n_i$  is the number of stars with luminosity  $L_i$  in the stellar population, and z.p. is the zero-point of the photometry. To determine this quantity for a given candidate, we use the calibration of Carlsten et al. (2019b) that relates the absolute SBF magnitude to the broadband color of the stellar population. Bluer stellar populations have brighter SBF magnitudes because those populations have, on average, brighter stars. With an apparent and absolute SBF magnitude in hand, we determine the distance modulus to the candidate.

We use the Sérsic profile (Sérsic 1963) fits reported by Carlsten et al. (2020a) as the model for the smooth surfacebrightness profile. While the light profiles are often more complex (e.g., lopsided or twisted) than is captured by a single Sérsic, the candidates are generally too small and faint to use nonparametric modeling as a function of radius. Using a Sérsic profile as a model for the smooth underlying profile where, in reality, the profile is more complicated can lead to spurious fluctuation power in the SBF measurement that can bias the distance significantly. To overcome this, for a subsample of the galaxies, we produce new Sérsic fits that are restricted to the outer regions of the galaxies, which are often much smoother and more amenable to SBF than the inner structured regions. A small subsample ( $\sim$ 10%) of the galaxies are too irregular to attempt an SBF measurement in any form. For these galaxies, we use other distance measures (TRGB and redshift) where possible or just leave the candidate as a "possible/unconfirmed" satellite, as described more in Section 5.

Using the fits for the smooth brightness profile, the fluctuation power is measured in the usual Fourier way described in detail in Carlsten et al. (2019b). The main steps in the SBF measurement are shown in Figure 1 for six example candidates in our catalog. Each of these dwarfs is confirmed to be at the distance of their host. Many of the dwarfs are LSB with  $\mu_{0,g} \sim 26$  mag arcsec<sup>-2</sup>, but SBF measurements with high signal-to-noise ratio (S/N) are still possible with the depth of the archival imaging.

To turn the SBF measurement into a distance constraint, we use the empirical calibration of Carlsten et al. (2019b). This calibration accounts for the dependence of SBF on stellar population via the integrated g - i color of a galaxy and provides the absolute SBF magnitude in the i band. However, for seven of our hosts, our

imaging data is in the g and r bands, not g and i. In Section 4, we extend the calibration of Carlsten et al. (2019b) into the r band using simple stellar population isochrone models and the subsample of calibrator galaxies of Carlsten et al. (2019b) that also have r-band imaging data. This calibration produces the absolute r-band SBF magnitude as a function of integrated g-r color.

Using either calibration, we follow the same procedure to turn the SBF measurement into a distance constraint. Here, we use a Monte Carlo approach. For each of 10,000 iterations, we sample a color from a Gaussian with mean equal to the measured color of the galaxy and standard deviation equal to the estimated uncertainty in the color. With this color, we use the SBF calibration to derive an absolute SBF magnitude. To account for the uncertainties in the calibration, in each iteration, we sample the calibration (slope and y-intercept) parameters from the Markov Chain Monte Carlo (MCMC) chains produced in the calibration fit of Carlsten et al. (2019b). This step accounts for the strong covariance between the slope and y-intercept in the calibration formula. We are left with a distribution of distances that is consistent with the measured SBF and color for a galaxy. From this distribution, we calculate a median distance and  $\pm 1\sigma$  and  $\pm 2\sigma$  distance bounds.

For much of the candidate sample, the measured SBF level is very low, and it is possible to show that these must be background galaxies. Stated differently, a dwarf satellite at the distance of the host should show a certain level of SBF, the lack of which provides a meaningful constraint. Following Carlsten et al. (2019a), we consider any dwarf whose  $2\sigma$ distance lower bound is beyond the distance of the host to be in the background of the host. It is important to emphasize that the lack of detected SBF is not due to limited S/N. Rather, the S/N is sufficient to firmly establish a lack of fluctuation at the level expected. Additionally, classifying these candidates as background is not simply due to the galaxies being too faint to measure SBF. The uncertainty of the SBF measurement accounts for the faintness and is thus included in the distance constraint. Carlsten et al. (2019a) concluded that many candidate satellites of M101 were background, and this has since been confirmed by HST imaging (Bennet et al. 2019), demonstrating that SBF distance lower bounds set in this way are reliable.

Some of the galaxies that we confirm to be background appear to have relatively strong fluctuation signals. The apparent signal is often actually residuals from the parametric profile fit rather than true SBF. The conclusion that these galaxies are background is, however, reliable because even with this added fluctuation power, the galaxies do not show the fluctuations that would be expected for a galaxy at the distance of the host.

Examples of galaxies that we conclude to be background along with examples of galaxies that we conclude to be real satellites from the same host are shown in Appendix A.

## 4. r-band SBF Calibration

Carlsten et al. (2019b) provides a calibration for  $\bar{M}_i$  as a function of g-i color. However, many of the host galaxies in this work only have imaging in r, or the r coverage is substantially deeper than the i band. Therefore, in this section we derive an absolute SBF calibration for the r band. While SBF is less prominent in the r band and the seeing is generally worse than in the i band (Carlsten et al. 2018), robust SBF

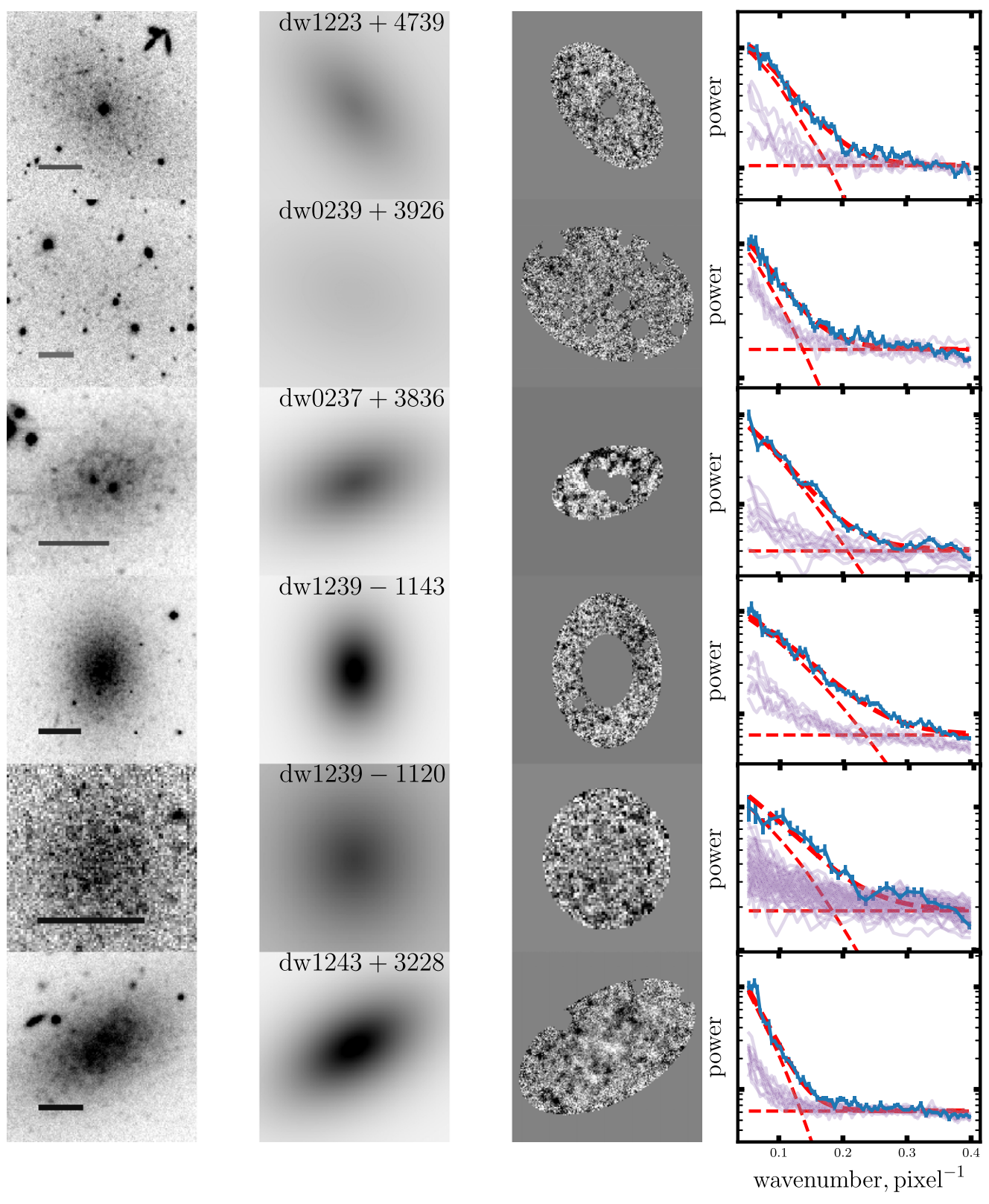


Figure 1. Demonstration of the SBF measurement process adopted in this work. The stacked r- or i-band images of the dwarfs are shown in the left column. The black bars in each image indicate 10". The Sérsic fit used to model the smooth galaxy profile is shown in the second column. This smooth model is subtracted from the galaxy and used to normalize the galaxy. Any contaminating point sources are masked, and an annulus is chosen within which to measure the SBF. This result is shown in the third column. The azimuthally averaged (and normalized) power spectrum of the image is shown in the right column along with the fitted combination of PSF power spectrum and white noise. The faint purple lines are the power spectrum measured in nearby background fields. The fluctuation power measured in these fields is subtracted from that measured from the galaxy. Note that even though dw0239 + 3926 (second from top) is very low in surface brightness, a high  $S/N \sim 15$  measure of the SBF is possible.

**Table 1**Galaxies Used in the *r*-band Calibration

Name	TRGB Distance (Mpc)
FM1	3.78
KDG 061	3.66
BK5N	3.7
UGCA 365	5.42
DDO 044	3.21
d0939 + 71	3.7
d0944 + 71	3.4
LVJ1218 + 4655	8.28
NGC 4258-DF6	7.3
KDG 101	7.28
M101-DF1	6.37
M101-DF2	6.87
M101-DF3	6.52
UGC 9405	6.3

distances are still possible in the r band. In this section, we extend the work of Carlsten et al. (2019b) and provide a calibration for  $\bar{M}_r$  as a function of g-r color. Twelve of the galaxies used in the calibration of Carlsten et al. (2019b) have r-band data, and we measure the r-band SBF magnitudes for these galaxies. We supplement this sample with two additional dwarf satellites in the M81 group that have CFHT g- and r-band imaging and HST TRGB distances (Chiboucas et al. 2009, 2013). These 14 galaxies are listed in Table 1 (we refer the reader to Carlsten et al. 2019b for more details on the sample).

Unfortunately, there are significantly fewer calibration galaxies available for the r band than for the i band. Therefore, we do not simply fit an  $\bar{M}_r$  versus g-r calibration but instead convert the  $\bar{M}_i$  versus g-i calibration into the r band using theoretical isochrones. We show that the calibration is consistent with the SBF observations of the galaxies in Table 1. The uncertainties associated with the filter transform are smaller than the uncertainties that will come from fitting the limited sample of calibrator galaxies. Carlsten et al. (2019b) found good agreement with the theoretical  $\bar{M}_i$  versus g-irelation predicted by either the MESA Isochrones and Stellar Tracks (MIST; Choi et al. 2016) or Padova (Bressan et al. 2012; Marigo et al. 2017) isochrone models for colors  $g-i \ge 0.5$ . In that work, it was unclear whether to attribute the disagreement at bluer colors to the isochrone models or the SBF measurements. However, recently, Greco et al. (2020) demonstrated good agreement between that calibration and MIST models at bluer colors if, instead of assuming a single stellar population, a double-burst star formation history is adopted for the bluest galaxies. Either way, we are not using the isochrones to provide an independent, absolute r-band calibration but rather to convert the existing, empirical i-band calibration into the r band, and this is more reliable.

To do the filter conversion, we transform  $\bar{M}_i$  to  $\bar{M}_r$  and g-i to g-r using simple stellar population (SSP) models from the MIST project with ages between 3 and 10 Gyr and metallicities in the range  $-2 < [{\rm Fe}/{\rm H}] < 0$ . Both conversions are fitted by linear functions in the g-r color. These conversions are shown in Appendix B. The  $\bar{M}_i$  to  $\bar{M}_r$  conversion is fit only in the color range g-r < 0.6, which is the range appropriate for the low-mass galaxies studied here.

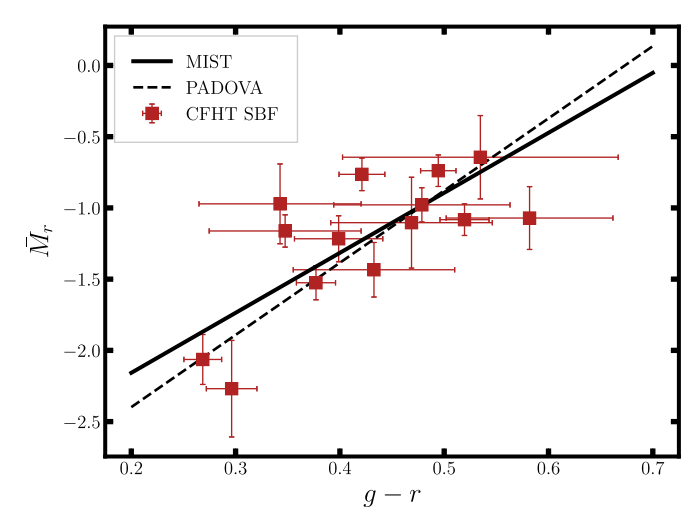


**Figure 2.** The SBF *r*-band calibration determined and used in this work. The black lines show the *i*-band calibration of Carlsten et al. (2019b) transformed into the *r* band using theoretical isochrones, as described in Section 4. The points are CFHT SBF measurements of galaxies with known TRGB distances, as listed in Table 1.

With filter conversion functions of the form

$$\bar{M}_i - \bar{M}_r = a(g-r) + b$$
  
 $(g-r) - (g-i) = a_2(g-r) + b_2$  (2)

and the i-band calibration of the form

$$\bar{M}_i = \alpha(g - i) + \beta, \tag{3}$$

the r-band calibration can be written as

$$\bar{M}_r = (\alpha - a - \alpha a_2)(g - r) - b - \alpha b_2 + \beta. \tag{4}$$

Performing the fits, we find a = -0.92, b = -0.243,  $a_2 = -0.530$ , and  $b_2 = 0.0319$  to determine a final calibration (using  $\alpha/\beta$  from Carlsten et al. 2019b):

$$\bar{M}_r = 4.21(g - r) - 3.00.$$
 (5)

To calculate distance uncertainties resulting from this calibration, we sample parameters from the chains in the MCMC fit of Carlsten et al. (2019b) and convert those into uncertainties in  $\bar{M}_r$  using Equation (4). Using the chains is crucial to capturing the covariance between the slope and *y*-intercept in the calibration. As shown in Appendix B, the uncertainty stemming from the filter transforms is  $\lesssim 0.1 \, \text{mag}$  (5% in distance) and is sufficiently subdominant to other sources of error that we do not include it.

The calibration given in Equation (5) is shown in Figure 2 along with the 14 calibrator galaxies. The agreement in the color range 0.3 < g - r < 0.6 is good between the observations and the converted *i*-band calibration, particularly in the *y*-intercept. It is unclear how well the slope of the data points matches that of the converted calibration. We calculate a reduced  $\chi^2$  (e.g., Equation (5) of Carlsten et al. 2019b) of the data points relative to the MIST line of  $\chi^2_{\rm red} = 2.0$  (including the whole color range), indicating the agreement is acceptable. We take this as evidence that the systematic uncertainties involved in the filter transform are minimal. Also shown in the dashed line is the calibration that results from using PADOVA isochrones instead of MIST isochrones. We see that the

Table 2
Overview of the SBF Results for Each Host

Host Name	Host Distance (Mpc)	Host $M_K$	Number Confirmed	Number Possible	Number Background
NGC 1023	10.4	-23.9	15	6	10
NGC 1156	7.6	-19.9	0	2	1
NGC 2903	8.0	-23.5	2	2	0
NGC 4258	7.2	-23.8	7	4	22
NGC 4565	11.9	-24.3	4	15	2
NGC 4631	7.4	-22.9	10	0	7
NGC 5023	6.5	-19.3	0	1	1
M51	8.6	-24.2	2	6	8
M64	5.3	-23.3	0	0	1
M104	9.55	-24.9	12	12	3

difference is minimal in the color range 0.3 < g - r < 0.6 that describes the majority of the galaxies in this paper.

#### 5. SBF Distances to Local Volume Satellites

In this section, we measure SBF and apply the calibration in Carlsten et al. (2019b) to determine an SBF-based distance for each candidate. Based on these distances, we classify each candidate into one of three categories: confirmed physical satellites, confirmed background contaminants, or galaxies where no SBF constraint is possible that we will refer to as "unconfirmed" or "possible" satellites. This last category is generally composed of galaxies that were so faint that the uncertainty in the SBF measurement is large. Additionally, some galaxies that were markedly non-Sérsic or had other problems (for instance, being behind a saturation spike) making the SBF measurement impossible are conservatively put into this category. We label a dwarf to be a confirmed satellite if the SBF is measured at an S/N > 5 and the distance is within  $\sim 2\sigma$ of the host's distance. We define the SBF S/N as simply the measured SBF variance level divided by its estimated uncertainty.5

A summary of the SBF-based candidate classifications is given in Table 2. We list the number of confirmed satellites, confirmed background galaxies, and unconfirmed galaxies. In this table, we give the number of candidates confirmed via any method (including TRGB or redshift), although the vast majority are confirmed via SBF. Details for each host (including what outside information is used in the confirmation of satellites) are given in Appendix A. As discussed in Appendix A, when TRGB and SBF distances exist for the same dwarf, the SBF distances agree very well with the TRGB distances

Overall, 52 of the 155 candidates of Carlsten et al. (2020a) are confirmed as physical satellites, while 55 are constrained to be background. We confirm 41 candidates as real satellites via SBF. A further 11 are confirmed via other distance measures available in the literature, particularly TRGB and redshift. The SBF results constrain 49 candidates to be background, and other distance measurements from the literature constrain a further six to be background. The remaining 48 candidates are still unconstrained. Only 25 of these are above our fiducial completeness limit of  $M_V < -9$ , assuming they are at the distance of the hosts. Deeper imaging or (most likely) spacebased imaging will be required to ascertain the distances to these candidates. Our results broadly demonstrate the power of

SBF in mapping and characterizing the dwarf galaxy population in the Local Volume.

For NGC 4631, extremely deep archival Subaru/Hyper Suprime-Cam (HSC) imaging exists for several of the candidate satellites. We acquired and reduced this data (described in detail in Appendix A) and used it to analyze the SBF of dwarfs around this host, as a check for the CFHT data. As detailed in the appendix, we find very close agreement with the shallower CFHT data. Additionally, we are able to constrain an additional candidate to be background that was ambiguous from the CFHT data.

#### 5.1. Classification Details

Here we discuss more details of the satellite confirmation process.

# 5.1.1. Setting the SBF S/N Threshold

We determine the SBF S/N threshold using image simulations performed by injecting dwarfs with SBF into the CFHT imaging; we refer the reader to Carlsten et al. (2019b) for details of the SBF image simulations. We find that dwarfs with  $M_g \sim -9$  mag and moderate surface brightness ( $\mu \sim 25$  mag arcsec<sup>-2</sup>) have SBF measurable with S/N  $\sim 5$  with the depth of the CFHT data. Almost all calibration galaxies of Carlsten et al. (2019b, all of which had TRGB distances) had S/N > 5 and spanned the same luminosity, surface brightness, and distance range as the candidate satellites in the current sample. Galaxies whose SBF distance result is consistent with the host's distance but the SBF is of low significance (S/N < 5) are placed in the "unconfirmed" category.

Using our prior work on M101, the S/N threshold we use here is conservative enough to prevent false-positive satellite confirmation. Carlsten et al. (2019a) confirmed two satellites around M101 using SBF. These satellites had SBF S/N  $\geqslant$  7, which means they would be confirmed by the threshold used here. Both of these have been confirmed by the *HST* imaging of Bennet et al. (2019). Carlsten et al. (2019a) also highlighted two other candidates as promising follow-up targets that had reasonably strong signal with S/N  $\sim$ 2-3. The *HST* imaging of Bennet et al. (2019) showed that this signal was not from SBF and the galaxies were background contaminants. The signal instead appeared to be coming from unmasked background galaxies. Using the threshold adopted here, these two candidates would be conservatively included in the "unconfirmed" candidate category.

<sup>&</sup>lt;sup>9</sup> For very noisy measurements, this quantity can be negative if the inferred SBF variance is negative.

#### 5.1.2. Visual Inspection

We also carefully visually inspect each candidate to make sure that the SBF signal is coming from the bulk stellar population of the galaxy and not from twists or other irregularities in the light profile. This visual inspection check is an important step to prevent false positives, particularly for the smaller candidates. From our experience with the calibration sample (Carlsten et al. 2019b), SBF should be clearly visible in dwarfs of the same luminosity, surface brightness, and distance as the current candidates. We emphasize that we do not discard galaxies or conclude galaxies are background based on the visual check alone. In a handful of cases (≤5%), we conservatively move a candidate from the "confirmed" bin into the "unconfirmed" bin if its visual appearance generates concern that the fluctuation signal is not actually coming from SBF.

### 5.1.3. False Negatives

Additionally, it is possible to have false negatives in the SBF analysis. The most likely cause is if the color of the candidate is measured incorrectly. We estimate the error in the galaxy colors using image simulations that should, in principle, capture the systematic uncertainty associated with the sky subtraction. However, it is possible that significant systematic errors in the sky subtraction linger. If the candidate was measured to be bluer than it actually is, the SBF distance can be greatly overestimated and vice versa. For our analysis, the most likely impact of this failure mode is for galaxies that are too faint for a meaningful SBF distance constraint. If one of these galaxies is measured to be significantly bluer than it actually is, we could falsely conclude it must be background because it lacks the strong SBF expected at that blue color. Note that erroneously measuring one of these galaxies to be too red would not have the same effect and would not change the categorization of this galaxy from being an "unconfirmed" candidate.

## 5.2. Completeness of Satellite Systems

The completeness of the catalogs of candidate satellites is quantified in detail in Carlsten et al. (2020a), but we give some overview here. In that work, we conducted extensive mock injection tests to quantify the detection efficiency as a function of dwarf luminosity and surface brightness. Most of the hosts had fairly similar completeness levels. Completeness was generally  $\gtrsim$ 90% for dwarfs down to a central surface brightness of  $\mu_{0,V} \sim 26.5 \, \mathrm{mag \ arcsec^{-2}}$  and for sizes greater than  $r_e \gtrsim 4''$ . Thus, the catalogs are likely complete down to luminosities of  $M_V \sim -9$  mag at the distances of these hosts over the survey footprints. We note that roughly half of the unconstrained or inconclusive satellite candidates are actually below this fiducial completeness limit. For the discussion below, we assume these hosts are 100% complete to  $M_V \sim -9$  mag and to  $\sim \mu_{0,V} \sim$ 26.5 mag arcsec<sup>-2</sup> over the survey footprint. The survey footprints are given in Carlsten et al. (2020a) and cover roughly the inner 150 kpc projected area for the six best-surveyed hosts (NGC 1023, NGC 4258, NGC 4565, NGC 4631, M51, M104), which are the focus for the rest of the paper.

A few of the hosts (e.g., NGC 1023) are located in regions of the sky with significant amounts of cirrus. Cirrus will generally make finding the faintest LSB dwarfs difficult, effectively setting the completeness limit to brighter total magnitudes. We expect the point-spread function (PSF)-scale fluctuations from cirrus to be small, but if present, that power should be subtracted during our background correction in the SBF measurement. The effect of cirrus on the detection of dwarfs will be largely accounted for in the mock injection tests that were done in Carlsten et al. (2020a). Because these hosts (even NGC 1023) are generally  $\gtrsim 90\%$  complete for dwarfs up to a central surface brightness of  $\mu_{0,V} \sim 26.5$  mag arcsec<sup>-2</sup> and down to luminosities of  $M_V \sim -9$  mag, cirrus does not seem to be a significant limitation to the goals of our work at present.

## 5.3. Structural Parameters of Confirmed Satellites

Tables giving the properties of the confirmed and possible satellites, including physical sizes and absolute luminosities, are given in Appendix C. For the physical quantities, we assume that the confirmed and possible satellites are at the distance of the host, instead of using the individual SBF distances, to prevent artificially inflating the scatter of these quantities due to the lower precision of the SBF distances. This implicitly assumes that the confirmed satellites are likely within the virial radius of the host along the line of sight and, hence, at about the same distance. <sup>10</sup>

Figure 3 shows various structural parameters for the confirmed satellites of the 10 hosts. They show close agreement with the scaling relations of the MW and M31 classical satellites. The confirmed satellites show better agreement with the Local Group (LG) dwarfs than the entire sample shown in Figure 6 of Carlsten et al. (2020a). Many of the objects in Carlsten et al. (2020a) were smaller than the LG dwarfs at fixed luminosity, indicating they were likely background. As seen in all three panels of Figure 3, the surface brightness completeness of Carlsten et al. (2020a) is  $\mu_{0,V} \sim 26.5$  mag arcsec<sup>-2</sup>.

# 5.4. The Importance of Distances

It is worth discussing why it is important that we consider only satellite systems with full (or nearly full) distance constraints on all candidate satellites. We could consider many more surveyed satellite systems if we relaxed this requirement and used a statistical background subtraction (e.g., Wang & White 2012) to remove background contaminants. However, as shown in Table 2, a majority of candidate satellites often turn out to be background. Furthermore, the scatter between hosts in the amount of background contamination is immense, due to differing amounts of structure along the line of sight. Including the six systems NGC 1023, NGC 2903, NGC 4258, NGC 4631, M51, and M104 that had good SBF results (with relatively few inconclusive candidates) and M101 from Carlsten et al. (2019a), we find that the rms scatter in confirmed background contaminants is  $\sim$ 11 per host (over roughly the inner 150 kpc projected area). This is significantly more than the rms scatter in confirmed satellites of  $\sim$ 5 per host over the same area. Therefore, the scatter introduced by any statistical background subtraction will overwhelm the true, intrinsic host-to-host scatter in satellite abundance, and  $\sim$ 5 times the host sample size would be required to get a similar constraint on the average number of satellites. To do a detailed analysis of the satellite abundances in nearby systems, distance constraints for

 $<sup>\</sup>overline{^{10}}$  While we do expect some of the confirmed satellites to be nearby field objects ( $\sim$ 500–1000 kpc in front of or behind the host), the dSph morphology of the majority of the confirmed satellites strongly implies that the majority are bona fide virialized satellites of their hosts. From our experience with the simulations (see below), we expect this population of nearby field dwarfs to constitute  $\sim$  10%–15% of the confirmed dwarfs.

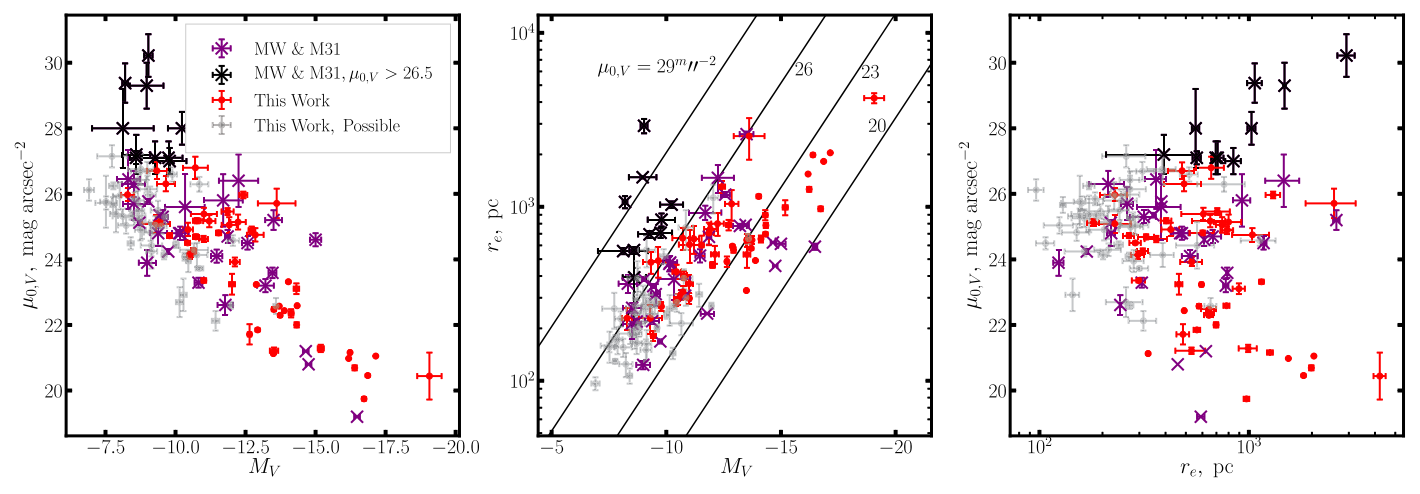


Figure 3. Structural parameters of the confirmed satellites (red). Shown in purple are the classical ( $M_V < -8$ ) MW and M31 satellites from McConnachie (2012), with black indicating the satellites with  $\mu_{0,V} > 26.5$  mag arcsec<sup>-2</sup>, which we consider the surface brightness limit of our survey. The gray points show the possible or unconfirmed satellites from the current work. Generally these are smaller and have lower surface brightness than the confirmed satellites.

the majority of candidate satellites are crucial, either from SBF/TRGB or redshift (e.g., Sales et al. 2013; Geha et al. 2017).

## 6. Satellite Systems from the Literature

In this section, we assemble the information on satellite systems of the nearby hosts that have been previously surveyed in the literature and combine these with the new hosts from the current work. For the rest of the paper, we only consider the six best-surveyed hosts from the current work (those whose surveys cover roughly the inner 150 kpc): NGC 1023, NGC 4258, NGC 4565, NGC 4631, M51, and M104. As discussed in the Introduction, there are six other nearby systems that have been well searched for satellites previously. We give an overview of the literature that gives the satellite properties, along with estimates of the completeness for each system. All of the satellites in these systems have been confirmed with distance measurements, and the surveys are complete down to at least  $M_V \sim -10$  to -9 over a large fraction of the host's virial volume. For reference, we list all of the satellite properties for each host in tables in Appendix C.

### 6.1. Previously Surveyed Systems

Positions for the MW classical satellites are taken from McConnachie (2012). Luminosities are taken from Muñoz et al. (2018) where available, and McConnachie (2012) otherwise. The distances are taken from the compilation of Fritz et al. (2018), and individual references are given in the appendix. We assume that the census of MW classical satellites is complete throughout the virial volume. For the LF, we assume the MW has an absolute magnitude of  $M_V = -21.4$  (Bland-Hawthorn & Gerhard 2016).

We take the sample of M31 satellites from Martin et al. (2016) and McConnachie et al. (2018). The luminosities come from McConnachie et al. (2018), altered to account for updated distances. The distances themselves come from a variety of sources (references are provided in the appendix), prioritizing HST distances over ground-based and variable star over TRGB, where possible. Due to the faintness of these satellites, the RGB is often not well populated, leading to relatively uncertain TRGB distances. The PandAS survey is sensitive to ultrafaint satellites of M31 with  $M_V \lesssim -6$ , but their imaging covers the

inner projected 150 kpc volume. However, with Pan-STARRS, the census of M31 satellites is likely complete through the virial volume down to  $M_V \sim -9$  (e.g., Martin et al. 2013a, 2013b). We assume an absolute magnitude of M31 of  $M_V = -22$  (Walterbos & Kennicutt 1987; Geha et al. 2017).

The satellites of Centaurus A come from Crnojević et al. (2019) and Müller et al. (2019). Crnojević et al. (2019) estimate their completeness at 90% for dwarfs brighter than  $M_V \sim -9$  over their Magellan/Megacam survey footprint, which roughly covers the inner projected 150 kpc. Similarly, Müller et al. (2019) estimate that they are complete down to  $M_V \sim -10$  over the inner projected 200 kpc.

The list of satellites of M81 comes from Chiboucas et al. (2013, 2009). The photometry for NGC 3077, M81, M82, NGC 2976, IC 2574, and DDO 82 comes from Gil de Paz et al. (2007). The photometry for IKN, BK5N, KDG061, and KDG064 comes from the recent HSC imaging of Okamoto et al. (2019). The rest come from Chiboucas et al. (2013). We convert the r magnitudes reported in Chiboucas et al. (2013) into V magnitudes assuming  $M_V \sim M_r + 0.4$  (Crnojević et al. 2019). The TRGB distances come from Chiboucas et al. (2013) and Karachentsev et al. (2013). We do not include any of the dwarfs that Chiboucas et al. (2013) consider to be tidal dwarf galaxies. We assume that the census of satellites of M81 is complete for all "classical"-like satellites ( $M_V \lesssim -8$ ) throughout the inner projected 250 kpc volume.

The satellite system of M101 comes from Tikhonov et al. (2015), Danieli et al. (2017), Carlsten et al. (2019a), and Bennet et al. (2019). The photometry for M101 uses the updated distance of Beaton et al. (2019). To convert from the B magnitudes reported by Tikhonov et al. (2015), we assume  $M_V = M_B - 0.3$ . We use the HST photometry of Bennet et al. (2019) for dwA and dw9. We use the *HST* photometry for DF1, DF2, and DF3 (S. Danieli 2020, private communication). We note that the magnitudes we take for these objects are significantly ( $\sim 1-2$  mag) brighter than those listed by Bennet et al. (2019). This is likely due to the aggressive sky subtraction used in the CFHT Legacy Survey data (Gwyn 2012) used in Bennet et al. (2017). We also include UGC 8882 among the M101 satellites. Carlsten et al. (2019a) gives an SBF distance to UGC 8882 of  $8.5 \pm 1.0$  Mpc, which is marginally consistent with the distance of M101 ( $D = 6.52 \,\mathrm{Mpc}$ ). The Carlsten et al.

SBF distance agrees well with that of Rekola et al. (2005), D=8.3 Mpc, who use a completely different (albeit somewhat outdated) calibration. To investigate this dwarf more closely, we measured its SBF distance in the r band of the CFHT Legacy Survey, which interestingly gives a somewhat smaller distance of D=7 Mpc, close to that of M101. We also measured its SBF with completely independent data using a color from DECaLS (Dey et al. 2019) and SBF magnitude from archival HSC r-band imaging, which agreed with the CFHT r-band distance. Thus, we tentatively include this object as a satellite of M101. Its extremely regular, quenched (Huchtmeier et al. 2009) dSph morphology supports this association. We assume that the satellite system of M101 is complete down to  $M_V \sim -8.5$  within the inner projected 200 kpc (see Figure 1 of Carlsten et al. 2019a for the different search footprints covering M101).

The properties of the satellites of M94 come from Smercina et al. (2018). We assume the census is complete to  $M_V \sim -9$  throughout the inner projected 150 kpc volume.

For these previously surveyed hosts, we do not include satellites that have lower surface brightness than  $\mu_{0,V}=26.5$  mag arcsec<sup>-2</sup>. As discussed above and in Carlsten et al. (2020a), this is the surface brightness limit of the satellite systems surveyed in this work. Satellites with significantly fainter surface brightness are detectable around the MW and M31 (and, to a lesser extent, M81 and CenA) from resolved stars, so to compare all systems on equal footing, these satellites are not included in the following. The tables in Appendix C indicate which satellites satisfy this criterion. Additionally, several (but not all) of the extremely LSB satellites, for instance AndXIX, are clearly the result of tidal stripping, and it is unclear if these satellites are appropriate to include in the comparison with simulations below. The subhalos hosting such stripped systems might not be recognized by the halo finders used in the simulations, as discussed more below.

We note that two of the confirmed satellites from the hosts in the current work are below the  $\mu_{0,V} = 26.5$  mag arcsec<sup>-2</sup> limit. They are also excluded in the LF comparisons below and are marked in the tables in Appendix C. However, we note that our conclusions do not qualitatively change if we keep this population of very LSB satellites. In the future, we will work to quantify the number of satellites with  $M_V < -9$  that are nevertheless missed due to surface brightness constraints.

### 6.2. MW Analogs versus Small Group Hosts

For the rest of this paper, we consider these six previously surveyed systems from the literature along with the six bestsurveyed hosts from the current work in more detail. In some of the comparisons below, we do not consider all 12 LV hosts together but instead roughly split them into hosts we argue are MW-like in halo mass and hosts that are more massive, which we term "small group." It is important to recognize that several of the surveyed LV hosts are significantly more massive than the MW and should not be directly compared to the MW. The specific mass bins that we choose are somewhat arbitrary, but these two bins at least allow us to consider trends with crudely matching halo masses. The MW-sized halos are those with halo mass roughly in the range  $0.8-3\times 10^{12}~M_{\odot}$ , and the small groups have halo mass in the range  $3-8\times 10^{12}M_{\odot}$ . These rough limits come from dynamical estimates of the total mass of these hosts from the literature. For the dynamical mass estimates, the relative velocities of satellites are used along with the satellites' projected separations from their hosts in a virial theorem-like mass estimator. In most of these cases, the satellites' projected separations are in the range

Table 3
Rough Dynamical Halo Mass Estimates for the LV Hosts

Name	$M_{\rm halo}~(\times 10^{12}~M_{\odot})$	Source
	MW-like Hosts	
MW	~1	1, 2
M31	~1.5	3, 4,5
M101	$1.5\pm1$	6, 7
M94	7	
NGC 4258	$3\pm1$	7
M51		
NGC 4631		
NGC 4565	•••	
	Small Group Hosts	
M81	$5\pm1$	7
Cen A	$7\pm2$	7,8
M104	$30 \pm 20$	7
NGC 1023	~6	9

Note. Sources: (1) Callingham et al. (2019), (2) Watkins et al. (2019), (3) Watkins et al. (2010), (4) González et al. (2014), (5) Peñarrubia et al. (2014), (6) Tikhonov et al. (2015), (7) Karachentsev & Kudrya (2014), (8) Woodley (2006), (9) Trentham & Tully (2009).

100–300 kpc, which is of the order of the virial radii,  $R_{200}$ , of these halos. Therefore, this dynamical mass should be roughly comparable to the virial mass,  $M_{200}$ , of these halos. Table 3 lists these estimates where available for our sample of hosts. For the halo estimates of NGC 4258, M94, and M104, the estimates from Karachentsev & Kudrya (2014) are likely overestimated. The estimates come from the dynamics of nearby group members, but considering that some of the group members included are likely not actual group members (many do not have redshift-independent distances), the dynamical mass is almost certainly overestimated. While the estimated mass of M104 is ostensibly above the upper end of our "small-group" mass range, we include M104 in the small-group category because this mass is likely overestimated as well, but we note that it might be more massive. We do not list dynamical mass estimates of NGC 4565, NGC 4631, and M51. Based on their stellar mass and peak rotation speed, we put NGC 4565, NGC 4631, and M51 into the MW-like group (see Carlsten et al. 2020a for these quantities).

As we will see below, this distinction by halo mass of the hosts is also reflected in the LFs. The small-group hosts have significantly richer satellite systems than the MW analogs do. We note that the small-group hosts are different from the MW analogs in other ways as well. The small-group hosts include the only two ellipticals in the whole sample (M104 and CenA) and the only S0. M81 is also unique in including two central late-type galaxies of similar stellar mass (M81 and M82 with  $M_{\star}=5\times10^{10}~M_{\odot}$  and  $M_{\star}=3\times10^{10}~M_{\odot}$ , respectively).

In closing this section, we caution the reader that these dynamical mass estimates are still relatively uncertain. For much of the quantitative analysis undertaken later in this paper, we investigate and model the satellite abundance as a continuous function of host stellar mass, not relying on this division into "MW-like" and "small group." However, we do assert that some of the hosts that are often compared to the MW as "analogs" (particularly M81 and CenA) do appear to have significantly more massive halos, based on these estimates. The ambiguity in how to construct a sample of MW analogs underscores the point that care must be taken when comparing nearby satellite systems. Understanding how best to compare

models to observed hosts with incomplete and imperfect halo mass estimates will be an important direction for future work in this area

#### 7. Theoretical Models

In this section, we introduce the theoretical models that we compare against and use to interpret our observed satellite systems. We primarily compare the observed satellite systems with those predicted from DMO simulations combined with an SHMR. We could have alternatively used hydrodynamic simulations (obviating the need to use an SHMR) or a semianalytic model (SAM) combined with a cosmological simulation. The public hydrodynamic simulations (e.g., Illustris and EAGLE) do not have sufficient baryonic resolution to comfortably resolve satellites of the luminosity we probe  $(M_V < -9 \text{ mag})$ . However, we can still make meaningful comparisons with hydrodynamic simulations for the brighter ( $M_V < -16$  mag) satellites. While SAMs could be used to explore the properties of satellites of virtually any mass, their added complication over a simple SHMR makes extracting physical interpretations more complicated. Therefore, as our primary point of comparison, we use halo catalogs from DMO simulations combined with an SHMR to populate the halos, but we also compare the bright satellite populations with those predicted from public hydrodynamic simulations.

#### 7.1. Simulation Suites

For the DMO simulations, we use the halo catalogs from the IllustrisTNG-100 project (Marinacci et al. 2018; Naiman et al. 2018; Nelson et al. 2018, 2019; Pillepich et al. 2018; Springel et al. 2018) and the high-resolution ELVIS zoom simulations (Garrison-Kimmel et al. 2014). Each simulation suite has its strength. TNG has a better constraint on the host-to-host scatter because of the large number of MW-like hosts (>1000) within the simulated volume, more than the 48 simulated hosts in the ELVIS project. On the other hand, the higher resolution of ELVIS allows us to consider the effect of resolution on the halo catalogs.

While the baryonic results of TNG will not resolve all of the satellites we are interested in (baryonic particle mass  $\sim 10^6~M_{\odot}$ ), the DM particle mass of  $7.5\times 10^6~M_{\odot}$  implies that DM subhalos hosting the satellites of interest ( $M_{\rm vir}\sim 5\times 10^9~M_{\odot}$ , see below) will be resolved. Note that we do not use the explicit DMO TNG simulation; instead, we use the dark matter halo catalog from the full baryonic run. This will capture any effect that the baryons might have on the halo abundances. In particular, this accounts for the enhanced destruction of subhalos by the baryonic disk, which has been shown to have a dramatic impact on subhalo abundance, particularly near the host galaxy (e.g., D'Onghia et al. 2010; Brooks et al. 2013; Errani et al. 2017; Garrison-Kimmel et al. 2017b; Kelley et al. 2019).

For the TNG simulation, we select host halos from the friends-of-friends (FoF) group catalog provided in the TNG public data release. To avoid any problems with the periodic boundary conditions, we only select halos that are more than 1.5 Mpc from a simulation box edge. We employ several different selection criteria for the hosts, as described below. When selecting on halo mass, we use the  $M_{200}$  value given in the FoF group catalog. When selecting on stellar mass, we use the stellar mass (from the hydro run) of the most massive subhalo in each FoF group. This corresponds to the stellar mass

of the central host (i.e., the MW). We use the SubFind catalog of subhalos to procure a list of subhalos in each FoF group.

For our fiducial SHMR (see below), the native resolution of TNG is adequate to resolve nearly all relevant subhalos. However, we are also interested in exploring alternative SHMRs with very high (2 dex) scatter in stellar mass at fixed halo mass. The resolution of TNG is inadequate to model this high-scatter case, which draws from significant numbers of halos below the DM mass resolution of the simulation. In order to account for these unresolved, low-mass subhalos, we "patch" the TNG subhalo catalog and insert these subhalos in a statistical fashion, extrapolating the subhalo mass function (SMF) down to lower masses. We account for the fact that the host-to-host scatter in subhalo abundance is super-Poissonian for low-mass subhalos using the results of Boylan-Kolchin et al. (2010). The details of this extrapolation process are given in Appendix D. We note that the results using the fiducial (low-scatter) SHMR are unchanged whether this extrapolation process is used or not.

The ELVIS suite consists of 24 isolated MW-sized hosts and 12 pairs of hosts in an LG-like configuration. We treat all 48 of these hosts in the same way. The ELVIS hosts range in mass fairly uniformly between 1 and  $3 \times 10^{12}~M_{\odot}$ . While this does cover the range we expect for the MW-sized observed hosts, due to the halo mass function (e.g., Tinker et al. 2008), it is more likely that an observed host occupies a  $10^{12}~M_{\odot}$  halo than a  $3 \times 10^{12}~M_{\odot}$  halo. Therefore, we expect the ELVIS hosts to be, in general, more rich in subhalos than the corresponding MW-like hosts from TNG.

As the ELVIS simulations are purely DMO, they will not account for the enhanced destruction of subhalos by a central disk. To account for this, we use the fitting formula of Samuel et al. (2020) that gives the survival rate of a subhalo based on its 3D separation from the host when comparing DMO and fully hydrodynamic runs of the same hosts in the FIRE simulation suite. Each subhalo in the ELVIS catalogs is given a survival probability based on its z=0 distance from the host and the Samuel et al. (2020) fitting formula. This has the effect of reducing the number of satellites predicted with ELVIS by roughly a factor of two in the inner 150 kpc, where our surveys are generally focused.

In some comparisons, we also make use of the hydrodynamic results of IllustrisTNG. With baryonic particle mass  $1.4 \times 10^6~M_{\odot}$ , the simulations will resolve a  $M_V = -16$  dwarf with roughly 100–200 stellar particles. Thus, we can meaningfully compare the full hydrodynamic results to the bright  $M_V < -16$  end of the satellite LFs. The halos and subhalos are selected as described above, and we directly use the  $M_V$  quantities reported in the TNG subhalo catalogs.

# 7.2. Stellar to Halo Mass Relation

With a catalog of subhalos in hand, we populate the halos with luminous galaxies using an SHMR. We use the peak virial mass of each subhalo,  $M_{\rm peak}$ , to determine the stellar mass of the galaxy. This is important to account for the effect of tidal stripping once a halo becomes a subhalo of a more massive galaxy. To determine  $M_{\rm peak}$ , we use the TNG merger trees and record the peak virial mass that each subhalo attains along its main progenitor branch. The ELVIS halo catalogs list  $M_{\rm peak}$  directly.

The well-known SHMRs from AM (e.g., Behroozi et al. 2013; Moster et al. 2013) are only valid for  $M_* \gtrsim 10^8~M_\odot$ , which is larger than the stellar masses of many satellites in our

sample. It is possible to extrapolate these relations down, but it is known that the SHMR of Behroozi et al. (2013) will overpredict the LF of MW and M31 satellites (Garrison-Kimmel et al. 2014). A steeper relation between stellar mass and halo mass is needed.<sup>11</sup>

We take as our primary SHMR the relation from Garrison-Kimmel et al. (2014) and Garrison-Kimmel et al. (2017a). This relation has the same functional form as the Behroozi et al. (2013) SHMR but uses a steeper power-law slope at the low-mass end. Garrison-Kimmel et al. (2014) used the Galaxy and Mass Assembly (GAMA) survey stellar mass function (Baldry et al. 2012) to infer a power-law slope of 1.92 ( $M_* \propto M_{\rm halo}^{1.92}$ ), as opposed to the slope of 1.412 inferred in Behroozi et al. (2013) using a Sloan Digital Sky Survey (SDSS)-derived stellar mass function. Garrison-Kimmel et al. (2014) showed that this SHMR could reproduce the stellar mass function of LG dwarfs down to  $M_* \sim 5 \times 10^5 \ M_{\odot}$ . Garrison-Kimmel et al. (2017a) found that a slightly shallower slope of 1.8 fits the LG dwarf stellar mass functions a little better. The SHMR of Garrison-Kimmel et al. (2017a) is a popular relation often referenced in the literature.

Thus, as our fiducial model, we use the functional form of the Behroozi et al. (2013) SHMR but modified to have a power-law slope of 1.8 at the low-mass end ( $M_{\rm halo} \lesssim 10^{11.5}~M_{\odot}$ ). All of the parameters other than the low-mass slope are taken from Behroozi et al. (2013). For this fiducial model, we assume a fixed lognormal scatter of 0.2 dex about this relation. While the scatter in the SHMR will likely increase for lower halo masses (e.g., Munshi et al. 2017), there is no current understanding (observational or theoretical) of specifically what the scatter should be. Thus we assume the scatter is the same as it is constrained to be at higher masses (e.g., Behroozi et al. 2013).

Garrison-Kimmel et al. (2017a) also suggest a second, higher-scatter SHMR that is able to reproduce the observed abundance of MW and M31 satellites. They find that the scatter and slope of the SHMR at the low-mass end are covariant, and the predicted number of classical satellites can be kept roughly the same if the slope and scatter are both increased in lockstep. In particular, they propose an SHMR with a slope of 2.6 and scatter of 2 dex that both well matches the MW LF (including a somewhat better fit at the bright end than the model with a slope of 1.8) and also offers a possible solution to the "Too Big to Fail" problem since the massive MW satellites could feasibly be hosted by relatively low-mass subhalos with this amount of scatter. We find that a slope of 2.4 and scatter of 2 dex more closely reproduce the satellite abundance of the fiducial model using TNG, and, thus, we consider this as an "alternative" SHMR throughout the analysis. Note that, for this model, we assume a constant 2 dex scatter for all halo masses, which is unphysical in the sense that scatter will likely be a smooth function of halo mass.12

The SHMR is used to assign a stellar mass to each subhalo. We assume a fixed mass-to-light ratio of  $M_{\ast}/L_{V} = 1.2$  to convert this stellar mass into a V-band magnitude. This mass-to-light ratio is roughly the average ratio inferred for the MW satellites (Woo et al. 2008). We note that our sample of satellites does not exhibit

a noticeable color-luminosity trend, and, thus, a constant mass-to-light ratio for all satellite luminosities is justified.

We do not attempt to assign a size or surface brightness to the model satellite galaxies. We simply assume that all galaxies above our fiducial luminosity limit of  $M_V \sim -9$  mag would be detectable. Relaxing this assumption will be an important step in future work.

Finally, another consideration to note is that we do not account for the possibility of dark subhalos. Presumably, some low-mass subhalos exist that do not contain a luminous galaxy as the UV background associated with cosmic reionization completely suppressed star formation in those halos. The halo mass scale at which this process becomes important is often estimated as a few  $\times 10^9~M_{\odot}$  (e.g., Okamoto et al. 2008; Okamoto & Frenk 2009; Ocvirk et al. 2016; Sawala et al. 2016b), but recent work is pushing this scale down to smaller masses (e.g., Kim et al. 2018; Graus et al. 2019; Wheeler et al. 2019; Nadler et al. 2020). These masses are at the low end of (or well below) the halo masses expected for classical-sized satellites, so we do not expect this to be a relevant physical process for the type of satellites we consider here.

## 8. Dwarf Satellite System LFs

In this section, we show the results of comparing the observed satellite systems to the ones predicted from the SHMR model described above. We show four main comparisons. First, we simply compare the observed systems with each other. We clearly see that observed hosts with higher inferred halo masses have richer satellite systems. Second, we compare the LFs for each observed host to those predicted from the models for each host. Third, we explore the number of satellites as a function of host stellar mass. This comparison demonstrates that the scatter between observed satellite systems closely matches that predicted by the simulations, once the mass of the host is accounted for. Finally, we look more closely at the average shape of the LFs by comparing the combined LF of all observed systems to the simulated systems to show that, while the total number of satellites agrees between observations and simulations, the observed hosts have more bright satellites and fewer faint systems than the SHMR model predicts.

## 8.1. Observed LFs

In this section, we directly compare the observed satellite systems with each other. Figure 4 shows the cumulative LFs for the hosts considered here split into the two groups (MW-like versus small group; see Section 6) by halo mass. To address the very different survey footprints for the different hosts, only satellites within 150 kpc (3D distance for the MW and M31, projected for the other hosts) are included, but further area correction is not performed. We note that 150 kpc is roughly half the virial radius for the MW-like hosts, but less for the more massive hosts.

We highlight a few interesting things in Figure 4. First, the MW appears to have a typical satellite LF compared to the other MW-like hosts. Second, there is large scatter in the LFs within each host class. The scatter would be even more if we compared the two mass bins together, emphasizing the

<sup>11</sup> We note that the more recent SHMR of Behroozi et al. (2019) does show a steeper slope.

<sup>&</sup>lt;sup>12</sup> Without the "patch" for low-mass subhalos that we make in the TNG catalogs, this alternative SHMR produces far too few satellites, confirming our assertion that the native TNG resolution is not adequate for exploring high-scatter SHMRs.

 $<sup>\</sup>overline{^{13}}$  The LF of M31 appears quite similar to that of the MW in Figure 4. Compared to other works in which they appear quite different, we have truncated the satellites at 150 kpc, which removes more satellites in M31 than from the MW, as well as applied a surface brightness cut of  $\mu_{0,V} > 26.5$  mag arcsec<sup>-2</sup> that removes a handful of M31 satellites but no MW satellites at these luminosities.

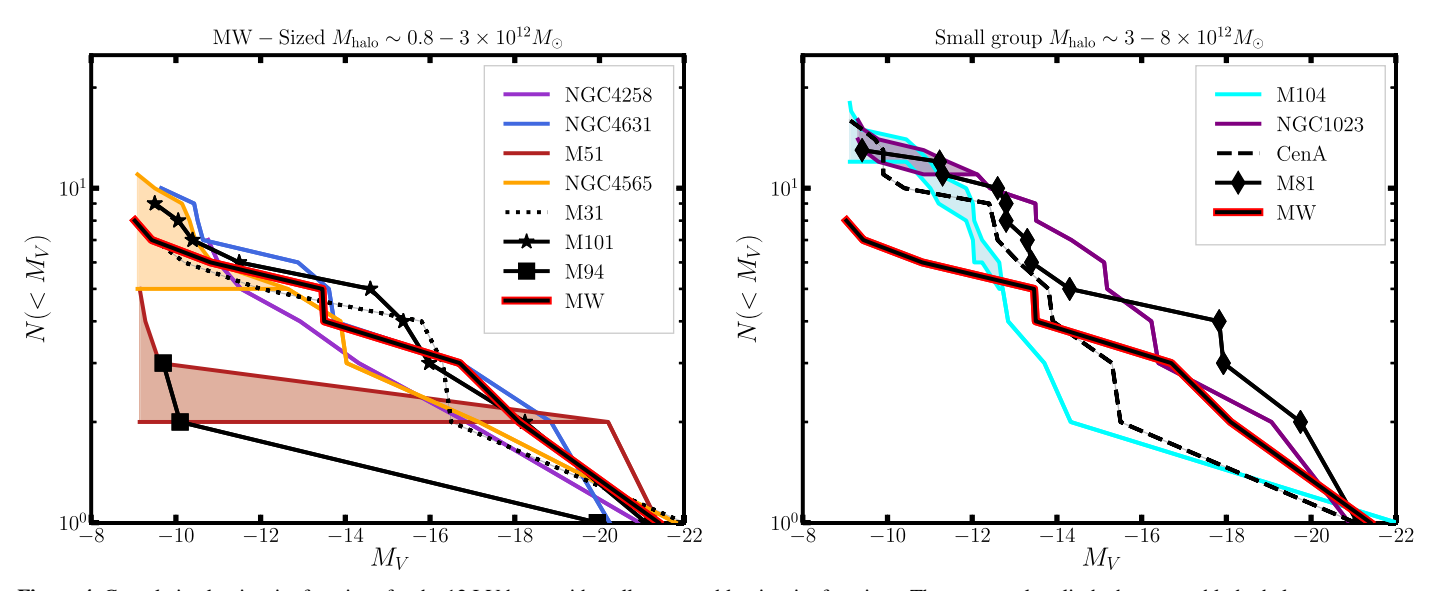


**Figure 4.** Cumulative luminosity functions for the 12 LV hosts with well-measured luminosity functions. The two panels split the hosts roughly by halo mass; see text for details. The MW is only shown in the right panel for comparison. The spread in some of the LFs indicates the membership uncertainty for the candidates where the SBF analysis was ambiguous. Both lower and upper bounds for the luminosity function are given. All hosts are restricted to the inner 150 kpc radius, but no further area corrections are applied.

importance of considering them separately. We will quantify the host-to-host scatter in Section 8.3.

#### 8.2. Individual LFs

In this section, we compare the individual observed LFs with those of matched simulated hosts from the IllustrisTNG simulations, using the fiducial SHMR. In Figure 5, we compare the observed LFs with those predicted from the models for the 12 observed hosts. The IllustrisTNG hosts are selected based on their stellar mass from the hydro results to roughly match the stellar mass of each observed host. In particular, each TNG host is given a probability to be included given by a Gaussian distribution in log stellar mass centered on the stellar mass of the observed host with spread 0.2 dex. We assume 0.2 dex is an appropriate estimate of the error in determining the stellar mass of nearby massive galaxies (e.g., Bell & de Jong 2001; Leroy et al. 2019). Thus the distribution of the stellar mass of selected TNG hosts is peaked at the observed stellar mass of the LV host but allows some spread due to possible measurement error. There are roughly 500-1000 TNG hosts selected for each observed host following this prescription.

To account for the different survey area coverage between the observed hosts, for each observed host, the models are forward modeled through the survey area selection function for that specific host. For comparison with the MW and M31, all model satellites within 300 kpc (three-dimensional distance) of the host are included. For the hosts surveyed in the current work, the area coverage of each host is taken from the survey footprints shown in Figure 1 of Carlsten et al. (2020a). For each observed host (other than the MW and M31), the model hosts are mock-observed from a random direction at the distance of the real host, and satellite galaxies are selected that project into the survey footprint. For the noncircular footprints shown in Figure 1 of Carlsten et al. (2020a), a random direction is taken to be north.

To account for uncertainties in the distances to the dwarf satellites, model satellites are selected within 500 kpc of the host along the line of sight. This will include some splash-back

satellites and field dwarfs that have not yet fallen into their host, but presumably the observed satellite systems include a few of these dwarfs as well. The 500 kpc limit is chosen as a compromise between the hosts that have had their satellites confirmed with TRGB and those that have had their satellites confirmed with SBF. HST TRGB can yield distances accurate to 5%, which at D=7 Mpc is  $\sim$ 300 kpc, whereas SBF, as applied here, can yield distances accurate to 15%, which at D=7 Mpc is  $\sim$ 1 Mpc. Our results are qualitatively unchanged if a larger (1 Mpc) line-of-sight limit is used instead.

For the systems that had inconclusive SBF distance constraints for some of their candidate satellites, Figure 5 shows the spread of possible LFs, given the uncertain or possible members.

In Appendix E, we show the comparison between the observed LFs and those predicted using the ELVIS high-resolution zoom DMO simulations. The results are similar to Figure 5, demonstrating that the resolution of IllustrisTNG does not appear to be affecting our results. The ELVIS-predicted LFs are somewhat richer than the TNG LFs because the ELVIS host halos are more massive, on average, than the TNG "MW-like" hosts, as discussed above. Recall that the TNG hosts are selected to have stellar masses similar to the observed hosts (most often with halo masses around  $\sim 1 \times 10^{12} M_{\odot}$ ), but the ELVIS hosts have halo masses fairly evenly distributed between 1 and  $3 \times 10^{12} M_{\odot}$ .

## 8.3. Satellite Richness versus Stellar Mass

The main goal of this section is to quantify the host-to-host scatter in the observations and compare with that of the models. More massive halos are expected to host more subhalos. While we have rough halo mass estimates for each host in our sample (see above), these estimates are not accurate enough to explore how satellite richness depends on halo mass. Instead, in this section we explore how satellite richness depends on stellar mass, which we use as a proxy for halo mass.

Figure 6 shows the relation between satellite richness and stellar mass for the observed hosts and the simulated hosts

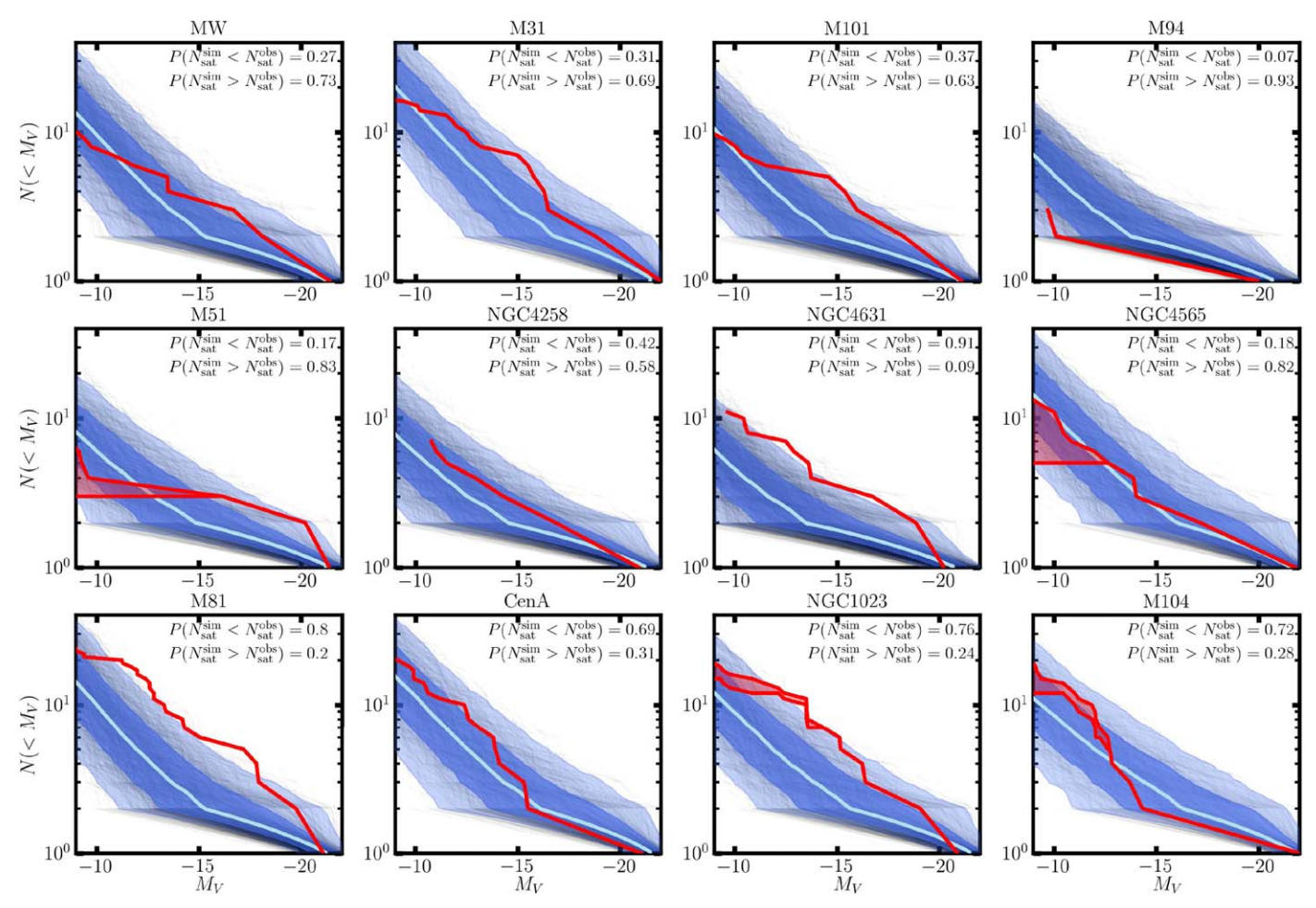


Figure 5. Cumulative luminosity functions for the 12 hosts in our sample (red). The thin black lines show the predicted LFs using the fiducial SHMR described in the text. The simulation hosts have been selected to have roughly the same stellar mass as the corresponding observed host. The blue regions show the  $\pm$  1,  $2\sigma$  spread in the models. The luminosity completeness is different for each host but is  $M_V \sim -9$  mag in all cases. For each host, the model satellite systems have been forward modeled considering the survey area selection function for each specific host. For the hosts that had inconclusive results from the SBF distances, a spread of possible LFs is shown, accounting for uncertain membership. The numbers in the corner of each panel give the fraction of simulated hosts that have more (and fewer) satellites with  $M_V < -9$  than the observed host.

using both the fiducial and alternative, high-scatter SHMR. We show the comparison when we select TNG hosts based on halo mass in the range  $0.8 \times 10^{12} < M_{200} < 8 \times 10^{12}~M_{\odot}$  and also on stellar mass in the range  $10^{10.3} < M_{\star} < 10^{11.2}~M_{\odot}$ . This shows that the results are largely unaffected by the specifics of how we select the simulated hosts.

To account for the different area coverage of the different hosts, only the satellites within 150 projected kpc are included, and we make the assumption that each observed host is complete to this radius. For the MW and M31, for which we have detailed 3D locations of the satellites, the observed satellite systems are mock-observed, in projection, at a distance of 7 Mpc (which is roughly the average distance of the LV hosts), and satellites are selected with a line-of-sight (LOS) distance constraint of  $\pm 500$  kpc from the host. The error bars show the spread ( $\pm 1\sigma$ ) in the satellite number for many different viewing directions. For the systems with inconclusive SBF results, the error bars show the spread ( $\pm 1\sigma$ ) in possible satellite richness accounting for this uncertainty. The simulated systems are mock-observed at a distance of 7 Mpc, and satellites are selected with an LOS distance constraint of

 $\pm 500$  kpc from the host. Only satellites brighter than  $M_V < -9$  are included. For the simulations, the stellar mass used for each host is the actual stellar mass for that host predicted by the hydrodynamic component of IllustrisTNG, not a stellar mass from AM (the results are unchanged if we use a stellar mass predicted from the SHMR).

There is clearly a positive relation between host stellar mass and satellite richness, in both the observed hosts and the simulated hosts. The steepness of the relation between host stellar mass and satellite richness appears to agree quite well between the observations and the model predictions, using either SHMR. The lines show the average trends of the simulated hosts, using each SHMR. We simply fit a line to this relation because of the relatively small dynamic range in host mass probed, but we note that from the SHMR, this relation will be nonlinear. The right panels of Figure 6 show the number of satellites corrected for the general trend of the models with host stellar mass. Both the models and observations are symmetric around zero, indicating that both SHMRs we consider accurately reproduce the normalization of the satellite LFs. Also shown in the plot is the rms scatter of the observed systems and the simulated systems. They agree well, indicating that the host-to-host scatter in the observed systems

 $<sup>\</sup>overline{^{14}}$  Specifically, each uncertain member is given a 50–50 chance of being a real satellite.

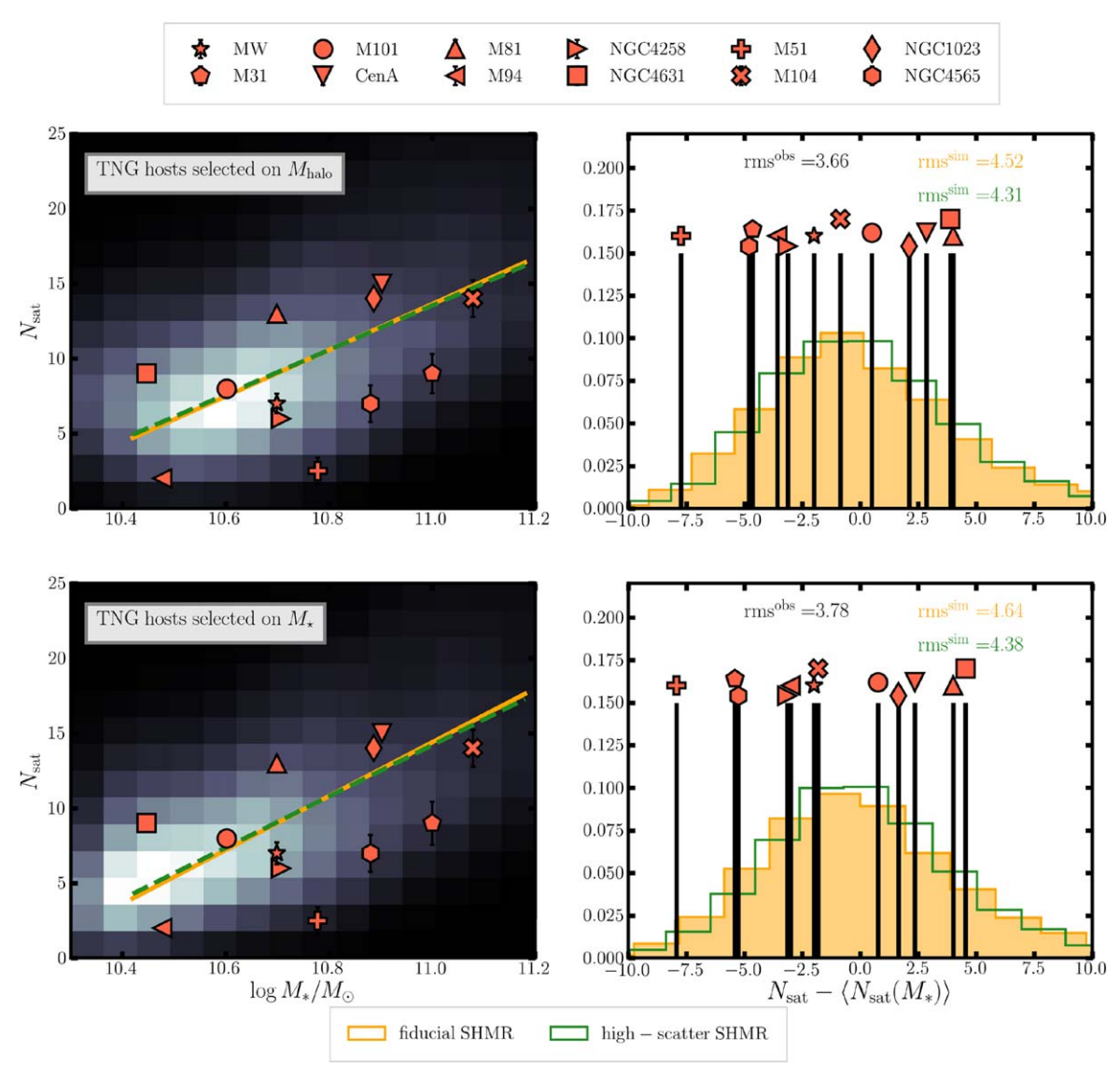


Figure 6. Left column: number of satellites  $M_V < -9$  mag within a projected radius of 150 kpc for each observed host (indicated by the symbols) as a function of host stellar mass. The simulated hosts are hosts drawn from IllustrisTNG-100 combined with both the fiducial SHMR and the high-scatter SHMR of Garrison-Kimmel et al. (2017a). The lines show the average relation for the simulated hosts. The background color map shows the results for the simulated hosts using the fiducial SHMR. Right column: the residual in the number of satellites, corrected for the average relation of the simulated hosts. The observations are corrected using the relation for the fiducial SHMR. The rms scatter agrees fairly well between the simulated and observed hosts. The top panels use TNG hosts selected on halo mass, while the bottom panels use a stellar mass cut on TNG hosts.

is quantitatively what one would expect from the models, once variations in the host mass are accounted for. Doing a two-sample Kolmogorov–Smirnov test between the observational sample and the simulated sample, we find p-values that the two samples are drawn from the same distribution of  $\sim\!0.4$ –0.8 for both ways of selecting the TNG hosts and both SHMRs, indicating good quantitative agreement. We note that, framed this way, M51 is even more deficient in satellites than the M94 system, considering its higher stellar mass.

The high-scatter SHMR results are shown as well, and somewhat counterintuitively, the high-scatter SHMR does not actually result in significantly greater host-to-host scatter in satellite abundance. Apparently, since both SHMR models produce roughly the same number of satellites, the distribution in satellite abundance for a population of hosts also is quite similar between models. The observed hosts across the whole range in stellar mass can be well explained by either SHMR.

These results show that the observed host-to-host scatter in satellite richness among nearby MW-like systems is comparable to that predicted by ACDM simulations using "standard" halo occupation models (i.e., the fiducial SHMR). Thus, we do not confirm the conclusions of Smercina et al. (2018), who argued that significantly increased scatter is required to explain M94's satellite system. We come to a different conclusion for a few reasons. First, we show that much of the observed scatter between hosts is due to the difference in host halo masses (as proxied by stellar mass). This is important to take into account when inferring host-to-host scatter. M94 has a low abundance of satellites largely because M94 has a relatively small stellar mass among "MW analogs." Second, our sample of 12 systems offers much improved statistics over the five considered by Smercina et al. (2018). Finally, the average number of satellites that our model predicts is significantly lower than that of Smercina et al. (2018). M94 appears to be a  $>3\sigma$  outlier from their simulated LFs (using their "standard" halo occupation

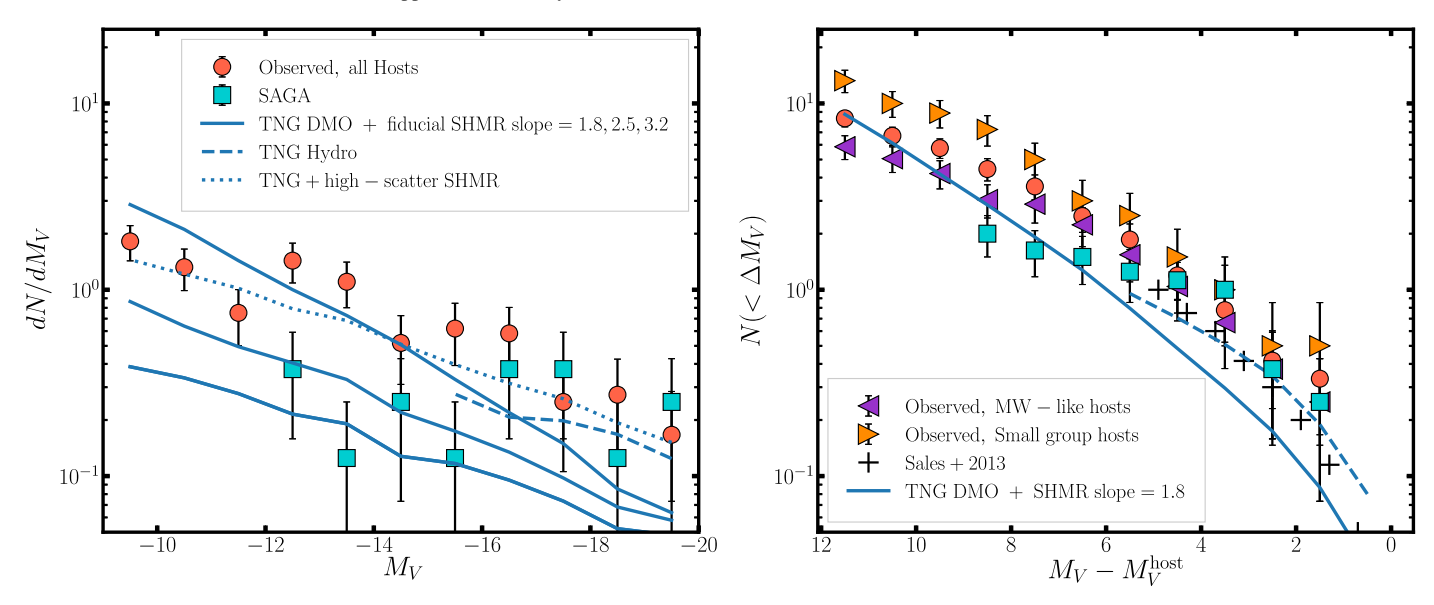


Figure 7. Left: average differential LF of the satellite systems within 150 kpc projected of all 12 observed hosts. The average simulated LFs are shown in blue. Curves corresponding to three different values of the low-mass slope of the fiducial SHMR are shown. The smallest slope value corresponds to the highest (most rich) LF. Note that no matter the slope used in the low-scatter SHMR, the simulated LF cannot match the shape of the observed LF. There are too many observed bright satellites. The alternative, high-scatter SHMR predicts a flatter LF, more in line with the observations. Right: the same observational samples are shown as a cumulative LF where the satellite luminosities have been scaled by the luminosity of the host. The LV host samples are shown all together and are also split into the MW-like hosts and "small-group" hosts (see Section 6 for discussion and definition). The average SAGA (Geha et al. 2017) LF is shown in turquoise. The SAGA results agree well with the Local Volume hosts for the bright satellites ( $M_V < -14$ ), but include fewer faint satellites. The satellite LF function results from the SDSS analysis of Sales et al. (2013) for hosts in the mass range  $10.5 < \log M_* < 11$  are also shown. Error bars show the Poisson scatter in the total number of satellites in each magnitude bin.

model), while it is only  $\sim 1-2\sigma$  for ours (see Figure 5). It is unclear where this discrepancy originates. However, we note that our model reproduces the mean observed satellite abundance well (Figure 6), while the model of Smercina et al. (2018) produces too many satellites compared to all five observed hosts they compare with (including CenA and M81, which are substantially more massive than the MW).

Smercina et al. (2018) find much better agreement in satellite abundance when considering a high-slope, high-scatter model, similar to the alternative model we consider here. It appears that much of the better agreement seen by Smercina et al. (2018) comes from the model predicting overall lower satellite abundances, which can be explained by using a steeper slope in the SHMR (i.e., an increase in scatter is not needed). Smercina et al. (2018) argue that a simultaneous increase in scatter is required, however, to explain M94's lack of a bright  $M_{\star} > 10^{7}$   $M_{\odot}$  satellite. This conclusion appears to likely be the result of limited resolution in the simulations. A high-scatter, high-slope SHMR has the effect of raising and flattening the LF (i.e., producing relatively more bright satellites compared to faint satellites). The EAGLE simulations used by Smercina et al. (2018) are even lower resolution than the raw TNG simulations.

On a larger note, we find that the distribution of total satellite abundances between hosts is not actually discriminatory to the scatter in the SHMR. The two SHMRs that we consider appear to equally well fit the relation between satellite abundance and host stellar mass, including normalization, slope, and scatter. We emphasize that this finding is likely only true for the classical satellite regime. For lower-mass satellites, the stochasticity of galaxy formation introduced by reionization suppression might lead to a qualitatively different picture. More discriminatory power, at least in the classical satellite regime, will come from the shape of the LFs, which is what we turn to next.

#### 8.4. Average LF Shape

In this section, we explore the shape of the LFs in detail. The shape of the LF is a sensitive probe of the low-mass slope of the SHMR. To make the comparison, we construct the average differential LF of the 12 observed hosts by considering the total number of satellites in different magnitude bins. We then compare this LF with the average LF of the simulated hosts. Figure 7 (left panel) shows this comparison for satellites with  $M_V < -9$  mag (and also  $\mu_{0,V} < 26.5 \,\mathrm{mag \ arcsec^{-2}}$ ) within a projected separation of 150 kpc of their host, assuming all 12 observed hosts are complete at this level. Therefore, the average LF will be a lower bound to the true LF since our hosts are not quite complete to 150 kpc. MW and M31 satellites are viewed in projection and selected as in Section 8.3. To account for the effect of projection angle on the satellite systems of the MW and M31, we average over many different projection angles. The uncertain membership of some satellites is also accounted for by averaging over all possible combinations of the uncertain satellites being members or not.

We compare with the TNG simulation results. Subhalos around the simulated hosts are selected in the same way as in the previous section. The TNG hosts are selected based on halo mass in the range  $0.8 \times 10^{12} < M_{200} < 8 \times 10^{12} M_{\odot}$ . We compare the observed average LF to the average simulated LF using the fiducial SHMR (with low-mass slope of 1.8), along with the results of using a slope of 2.5 and 3.2. The left panel of Figure 7 shows that no matter the slope used in the low-scatter SHMR of Garrison-Kimmel et al. (2017a), the average simulated LF will not quite match the shape of the observed LF. The observed LF has too many bright satellites and an overall flatter LF.

We also show the results of the alternative high-slope, high-scatter SHMR. This qualitatively shows the effect of increasing the slope and scatter in the SHMR. As found by Garrison-Kimmel et al. (2017a), the LF is elevated at the bright

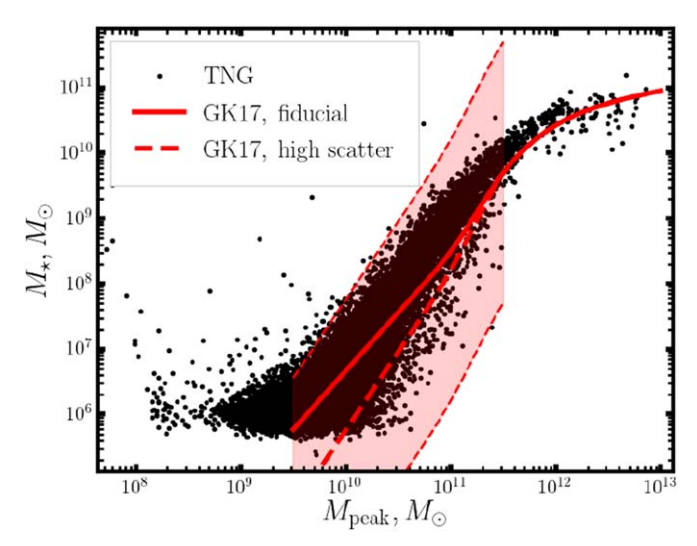


**Figure 8.** Inferred SHMR for satellites of hosts in the stellar mass range  $10^{10.3} < M_{\star} < 10^{11.2}~M_{\odot}$  in the hydrodynamic results of the IllustrisTNG simulation. Satellites are selected as subhalos within 300 kpc of their hosts. Note the higher normalization of the hydro SHMR compared to that of Garrison-Kimmel et al. (2017a) around  $M_{\rm peak} \sim 10^{11}~M_{\odot}$ .

end and flattened, leading to better agreement with the observed hosts.

Finally, we make use of the full hydrodynamic results of the TNG simulation and compare with the bright  $(M_V < -16 \text{ mag})$ end of the observed satellite LF. In this case, the agreement with the observations is better than with the fiducial SHMR, although they are still lower than the observed LF. Part of this might be due to the set of observed hosts having more numerous, massive "small-group" hosts than the set of simulated halos. We estimate four out of 12 of the observed hosts are in this more massive category, while one-fifth of the simulated halos are in that mass range. It appears that the TNG hydrodynamic results are in better agreement with the observations because halos with  $M_h \sim$  $10^{11} M_{\odot}$  end up with more stars than predicted with the fiducial SHMR. The stellar and halo mass of galaxies in the hydrodynamic TNG results are shown in Figure 8 compared to both SHMRs of Garrison-Kimmel et al. (2017a). The hydrodynamic results have a noticeably higher normalization at  $M_h \sim 10^{11} M_{\odot}$ , which effectively leads to a higher abundance of bright satellites.

To explore whether the spread in host luminosities is affecting the average LF shape, we normalize by the host luminosity in the right panel of Figure 7. This approach has been used before to look at the shape of the average LF when including hosts of different luminosity (and mass; e.g., Sales et al. 2013; Nierenberg et al. 2016). Framed this way, the observed satellite systems still have more bright satellites than the fiducial SHMR model predicts. The hosts all have  $M_V$  values within roughly 1–2 mag of each other, so this normalization does not greatly affect the shape of the LF.

We also compare with the results from SDSS reported in Sales et al. (2013). The results of Sales et al. (2013) come from spectroscopically confirmed satellites in SDSS. Sales et al. (2013) report  $\Delta M_r$ , which we assume is roughly equivalent to  $\Delta M_V$ . Additionally, their results include all satellites within the virial radius of the hosts ( $\sim$ 300 kpc). To roughly compare with our satellite LFs that only include satellites in the inner 150 kpc, we simply divide their satellite counts by two. This is roughly the fraction of satellites that the SAGA Survey (Geha et al. 2017) finds within 150 kpc of the host compared to within 300 kpc. We

find fair agreement with their satellite counts in the region of overlap. Their results extend only to  $\Delta M = 5$ , whereas our results extend seven magnitudes fainter in satellite luminosity.

In this figure, we compare with the average observed LF of the eight MW analogs of the first SAGA release (Geha et al. 2017). We estimate that eight out of our 12 hosts would qualify as "MW analogs" according to the criteria of Geha et al. (2017), including some of the "small-group" hosts, so this is a fairly reasonable comparison. Only one host (M104) is above their sample range of  $M_K$  (-23 <  $M_K$  < -24.6), and one (NGC 4631) is actually below this range. Two others (M51 and M81) would not qualify, due to the presence of a bright nearby companion (NGC 5195 and M82, respectively). 15 In comparing with the SAGA results, we assume  $M_V \sim M_r + 0.2$  and only take satellites within 150 kpc of their host. The SAGA hosts also show a surplus of bright satellites and a flatter LF slope. This was noticed by Geha et al. (2017) and Zhang et al. (2019). The SAGA hosts appear to have fewer satellites in the range  $-14 < M_V < -12$  than our observed hosts. Even conservatively limiting to our "MW-like" hosts, the LV hosts are richer at these magnitudes. This is possibly indicating some incompleteness in the SDSS catalogs used in SAGA, although a more detailed comparison of the host samples is needed to understand this difference.

The observed systems are the most discrepant from the fiducial SHMR predictions around  $M_V \sim -16$  to -17, but they are in surplus at even brighter, LMC-like magnitudes as well. This holds for both the "MW-like" and "small-group" hosts. Several observational results have argued that Magellanic Cloud (MC) analogs are fairly rare around MW analogs (e.g., Liu et al. 2011; Tollerud et al. 2011). Liu et al. (2011) find that 81% of MW analogs in SDSS do not have any MC-like satellite within a projected 150 kpc, with 11% having one and 4% having two. They define an MC analog as a satellite between two and four magnitudes fainter than the host. We note that five (NGC 4631, MW, M31, <sup>16</sup> M81, and M101) of the 12 LV hosts would qualify as having one or more MC analogs according to this definition. Similarly, six out of eight of the SAGA hosts have at least one satellite within two and four magnitudes fainter than the host and within 150 kpc projected. Liu et al. (2011) define an MW analog as having  $-21.4 < M_r < -21.0$ . Most of the SAGA hosts are within this range, while some of our hosts are above and some are below.

We note that we are assuming a constant  $M/L_V$  ratio in the AM model for all of the simulated galaxies. It does seem feasible that the discrepancy in the LF could be due to changing  $M/L_V$  ratio for different luminosity satellites due to different star formation histories. Brighter satellites will likely continue to form stars longer after infall than very faint satellites (Fillingham et al. 2015). However, as mentioned above, the satellites do not exhibit a strong color versus luminosity trend.

## 8.5. Summary and Implications for the SHMR

In Section 8, we have used an SHMR combined with DMO simulations to generate model satellite systems and compared them with the observed systems. In particular, as a fiducial model, we used the low-scatter SHMR of Garrison-Kimmel et al. (2017a). This SHMR is well reproduced in several high-resolution zoom hydrodynamic simulations. Both the FIRE

 $<sup>\</sup>overline{^{15}}$  It is unclear how the second environmental cut that SAGA uses, which removes hosts that are within two virial radii of a 5  $\times$  10<sup>12</sup>  $M_{\odot}$  host from the 2MASS group catalog, would restrict the LV sample.

<sup>&</sup>lt;sup>16</sup> Depending on whether M33 is projected within 150 kpc.

(Fitts et al. 2017) and NIHAO (Buck et al. 2019) projects produce galaxies that fall on or near this relation (see Figure 6 of Garrison-Kimmel et al. 2017a for a detailed comparison with simulation results). In particular, Buck et al. (2019) find an SHMR with a slope of 1.89 for their simulated dwarf satellites, very similar to the slope we adopt here. We note, however, that there is still significant scatter in the predicted SHMR among different simulation projects (see, e.g., Agertz et al. 2020).

We found that the overall number of satellites and the hostto-host scatter of the observations were closely matched by both the fiducial, low-scatter SHMR and the alternative, highscatter SHMR. Satellite abundance alone is not discriminatory to the scatter in the SHMR, at least in the classical satellite regime probed here. However, we find that the fiducial SHMR does not quite match the observed shape of the composite satellite LF. This is independent of the slope used in the lowmass regime, suggesting that the problem is in the normalization of the standard Behroozi et al. (2013) SHMR around  $\sim 10^{11} M_{\odot}$ . We find a similar result if we use other popular SHMRs from the literature, including that of Rodríguez-Puebla et al. (2017) and Moster et al. (2018). Both of these SHMRs have the same or lower normalizations than Behroozi et al. (2013), causing a lack of bright satellites. The SHMR of Brook et al. (2014), which comes directly from AM the LG satellites, has a higher normalization at  $\sim 10^{11} M_{\odot}$  and does more closely match the average observed LF. Recently, the second data release of the SAGA Survey (Mao et al. 2020) also noted an overabundance of bright satellites compared to their galaxysubhalo connection model. They mentioned that increasing the normalization of the GAMA field LF (used to anchor the SHMR used in that work) within its quoted  $2\sigma$  uncertainty could resolve this overabundance.

On the other hand, when comparing with the high-scatter, high-slope SHMR of Garrison-Kimmel et al. (2017a), we find that the predicted LF is flatter and in better agreement with the observations. This provides another avenue to reconcile the predicted and observed LFs and might indicate that high scatter is needed, after all, in the SHMR in the low-mass regime.

At this point, it is unclear which of these options (higher normalization or higher scatter in the SHMR) is the best option. The higher normalization option should be testable with observations of the dwarf galaxy field stellar mass function. However, it is possible that the surveys upon which current stellar mass function measurements are based (e.g., SDSS and GAMA) are incomplete to dwarfs with  $M_{\star} < 10^9~M_{\odot}$  due to, for example, LSB. This leads to the lower normalization seen in the common SHMRs (e.g., Moster et al. 2018; Behroozi et al. 2019). Next-generation spectroscopic surveys, which will have better sensitivity and surface brightness completeness, will be an important test of this.

We also note that the scatter of 2 dex that is used here is large enough that it should be noticeable from the dynamics of MW classical satellites (e.g., Read & Erkal 2019). Fitting for an SHMR is beyond the scope of the current paper but will be an important avenue for future work. It will also be important to explore how a different SHMR might change our conclusion that the host-to-host scatter in satellite abundance for simulated galaxies closely matches that of observed galaxies. On a broader note, the LFs shown in Figure 7 show that the statistics are already sufficient with the current sample of LV satellite systems to place powerful constraints on what the SHMR can be in the low-mass regime.

#### 9. Conclusions

The dwarf satellites of the MW are a premier probe of smallscale structure formation and the properties of dark matter. Dwarf galaxies are also important probes of galaxy formation, particularly of the effect of stellar feedback, and dwarf satellites, in particular, are sensitive to the effect of quenching by a massive host. The effectiveness of these processes may differ on a host-to-host or even satellite-to-satellite basis. To get a full picture of small-scale structure, satellite systems beyond the MW must be studied to comparable levels of detail. We do not yet have a sense of what a "normal" satellite system is and, thus, no way of knowing if the MW satellites (in properties or abundance) are "typical." In studying the lowmass satellites around hosts other than the MW, the limiting step is usually the difficulty in getting distances to candidate satellites to confirm their association with a host. In this paper, we measure the distance to candidate satellites around a large number of hosts and perform an in-depth analysis of their satellite LFs to investigate the SHMR of low-mass dwarf galaxies.

We used SBF measurements to confirm satellite candidates identified in Carlsten et al. (2020a) around several hosts in the Local Volume. The SBF analysis cleans the satellite systems of background contaminants, allowing for an in-depth analysis of the satellite abundance and properties, previously only possible for a handful of very nearby systems. There were six hosts (NGC 1023, NGC 4258, NGC 4565, NGC 4631, M51, and M104) whose survey footprints were a significant portion of the host's virial volume and had usable SBF results. The remaining four (NGC 1156, NGC 2903, NGC 5023, and M64) either had ambiguous SBF results, with most candidates remaining unconstrained, or had very limited survey area coverage.

The systems with nearly complete distance constraints show significant scatter in the amount of background contamination present in each field. This scatter completely overwhelms the true host-to-host scatter in the abundance of satellites, highlighting the importance of getting distances to candidate satellites discovered around nearby galaxies.

For the group of well-surveyed systems, we explore the LFs of these satellite systems in more detail. We combine this sample of six with a sample of six nearby hosts that have been previously well surveyed for satellites. This is by far the largest sample of nearby, roughly MW-sized hosts whose satellite systems have been surveyed down to approximately the faintest classical satellites. The sample of 12 hosts naturally divides into a group of eight hosts that are MW-like (NGC 4258, NGC 4565, NGC 4631, M51, MW, M31, M94, and M101) and a group of four hosts that are somewhat more massive (NGC 1023, M104, CenA, M81), which we refer to as "small-group" hosts. The division is based on available estimates of the hosts' dynamical masses. The more massive systems clearly have more rich satellite systems than the MW-like hosts, and we see a clear correlation between satellite abundance and host stellar mass (see Figures 4 and 6). We find that the LF of MW satellites is remarkably typical compared to the other MW-like hosts.

To further interpret the LFs of the observed satellite systems, we develop a simple model based on *N*-body cosmological simulations coupled with an SHMR. Luminous galaxies are painted onto the DMO results with an SHMR. The fiducial SHMR we use comes from Garrison-Kimmel et al. (2017a) and

is known to reproduce the normalization of the LF of the MW and agrees fairly well with the results of high-resolution hydrodynamic simulations from multiple projects. The predicted satellite systems from this model are able to reproduce both the normalization and spread of the observed satellite systems, for both the "MW-like" hosts and the "small-group" hosts (see Figure 5).

We consider the satellite richness as a function of the host stellar mass, which we use as a rough proxy for the host halo mass. Both the observed systems and simulated systems show a similar positive relation between satellite number and host stellar mass. Using this relation, we quantitatively show, for the first time, that the observed systems exhibit the same host-to-host scatter as the simulated systems once host mass is accounted for. Thus, we do not confirm previous results that conclude the observed scatter is more than expected from simulations (e.g., Geha et al. 2017; Smercina et al. 2018), assuming standard halo occupation models. This difference is due to our use of a larger sample of observed hosts, which allowed us to take the different stellar/halo host masses into account explicitly.

In parallel, we also consider an alternative high-slope, highscatter SHMR as proposed by Garrison-Kimmel et al. (2017a). We find that this model predicts a similar average abundance of satellites and host-to-host scatter. Interestingly, greatly increasing the scatter in the SHMR does not appear to significantly increase the host-to-host scatter in satellite abundance, at least in the classical satellite regime, as long as the average satellite abundance is held roughly constant by also increasing the slope of the SHMR. In order to use this SHMR, we had to statistically insert subhalos into the TNG catalogs, effectively correcting for the relatively low resolution of the simulation. It will be important to check these results when cosmological volume simulations become available that have the resolution of current zoom-in simulations. It will also be important to investigate whether the same result holds for the abundance of lower-mass satellites (below the classical regime) in which the suppressing effect of reionization will play a larger role.

Finally, we consider the average shape of the observed LF and compare with the average simulated LF. We find that while the simulations and the fiducial SHMR can produce the right total number of satellites, the simulations seem to underproduce bright satellites and overproduce faint ones (see Figure 7). This appears to be independent of the power-law slope of the SHMR in the low-mass regime, as long as the SHMR is fixed to the relation of Behroozi et al. (2013) at higher masses (halo mass  $\sim 10^{11} M_{\odot}$ ). The hydrodynamic results of IllustrisTNG over the range in satellite luminosities that are resolved in the hydrodynamic simulation ( $M_V < -16$  mag) seem to show better agreement with the observations. Our observations seem to require a higher normalization of the SHMR around a halo mass of  $\sim 10^{11} M_{\odot}$  in order to match the observed abundance of massive satellites. Alternatively, the high-slope, high-scatter SHMR predicts a flatter LF, with more bright satellites, in better agreement with the observations than the fiducial SHMR. We will investigate in future work which of these options, a higher normalization of the SHMR or greatly increased scatter, is better able to match the observed satellite abundances.

We find that our average LF agrees quite well with the initial SAGA Survey (Geha et al. 2017) results at the bright end, which show a similar surplus of bright satellites. The LV

systems do show significantly more faint ( $M_V \sim -13$ ) satellites than the SAGA results, however.

The true SHMR valid for this low-mass regime remains a significant open question in the field of dwarf galaxy formation and near-field cosmology. In the future, the observed satellite systems around the MW and similar nearby hosts will continue to play a significant role in constraining the SHMR. With the Vera Rubin Observatory, the observational sample has the potential to grow tremendously, with SBF playing a facilitating role in providing distances to low-mass satellites in systems out to 20 Mpc (e.g., Greco et al. 2020).

Support for this work was provided by NASA through Hubble Fellowship grant No. 51386.01 awarded to R.L.B. by the Space Telescope Science Institute, which is operated by the Association of Universities for Research in Astronomy, Inc., for NASA, under contract NAS 5-26555. J.P.G. is supported by an NSF Astronomy and Astrophysics Postdoctoral Fellowship under award AST-1801921. J.E.G. is partially supported by the National Science Foundation grant AST-1713828. S.G.C. acknowledges support by the National Science Foundation Graduate Research Fellowship Program under grant No. DGE-1656466. A.H.G.P. is supported by National Science Foundation grant Nos. AST-1615838 and AST-1813628.

This work is based on observations obtained with Mega-Prime/MegaCam, a joint project of CFHT and CEA/IRFU, at the Canada–France–Hawaii Telescope (CFHT), which is operated by the National Research Council (NRC) of Canada, the Institut National des Science de l'Univers of the Centre National de la Recherche Scientifique (CNRS) of France, and the University of Hawaii.

Software: SExtractor (Bertin & Arnouts 1996), sep (Barbary 2016), Scamp (Bertin 2006), SWarp (Bertin 2010), astropy (Astropy Collaboration et al. 2018), imfit (Erwin 2015).

# Appendix A Details of the SBF Results

The main results of the SBF analysis are given in Tables 4–14. In these tables, we only list the galaxy name and the SBF results. We remind the reader that we split the dwarfs into three categories: confirmed physical satellites, confirmed background contaminants, or galaxies where no SBF constraint is possible that we refer to as "unconfirmed" or "possible" satellites. More information, including photometry, can be found in Carlsten et al. (2020a). For convenience, we include the photometry for the confirmed and possible satellites in Appendix C. Physical sizes and absolute magnitudes are included in those tables. In the following subsections, we go through each host and discuss the SBF results in detail, focusing on the dwarfs that are exceptions to our general classification guidelines of confirmed/background/unconstrained. We also describe any auxiliary distance information used in confirming or discarding satellites.

To show examples of these three categories, Figure 9 shows examples of galaxies that we conclude to be background along with examples of galaxies that we conclude to be real satellites from the same host. The galaxies that we constrain to be background are roughly the same surface brightness as the confirmed satellites but show visibly smoother surface-brightness profiles without any SBF. The example background

**Table 4** NGC 1023 SBF Results

Name	Confirmed SBF S/N	Distance (Mpc)	Name	Possible SBF S/N	Distance (Mpc)	Name	Background SBF S/N	Distance (Mpc)
dw0233+3852	5.7	$12.5^{+2.0,4.5}_{-1.7,3.1}$	dw0238+3805			dw0234+3800	4.8	> 17.5
dw0235+3850	11.3	$11.7^{+0.9,1.9}_{-0.9,1.8}$	dw0239+3910	2.2	$11.8^{+4.4,\infty}_{-2.6,4.4}$	dw0236+3752	5.5	> 11.9
IC 239		•••	dw0241+3852	2.1	$15.3^{+6.3,\infty}_{-3.4,5.6}$	dw0236+3925	1.5	> 14.1
dw0237+3855*	37.5	$7.1^{+0.5,1.0}_{-0.5,1.0}$	dw0241+3829	1.9	$12.7^{+5.7,\infty}_{-2.5,3.9}$	dw0237+3903	1.9	> 13.1
dw0237+3836	20.8	$10.6^{+0.8,1.6}_{-0.8,1.7}$	dw0242+3757	0.4	$16.0^{+\infty,\infty}_{-7.5,9.8}$	dw0238+3808	-0.7	> 16.8
dw0239+3926	14.4	$10.8^{+0.7,1.4}_{-0.7,1.5}$	dw0243+3915	0.9	$14.0^{+\infty,\infty}_{-4.3,6.2}$	dw0239+3824	1.3	> 13.3
dw0239+3903	8.2	$8.6^{+1.8,3.9}_{-1.6,3.0}$				dw0240+3844	7.0	> 16.7
dw0239+3902	7.0	$11.5^{+1.2,2.7}_{-1.1,2.1}$				dw0240+3829	-0.2	> 21.6
UGC 2157 dw0240+3854	 19.1	$11.2^{+0.5,1.0}_{-0.4,0.8}$				dw0241+3923 dw0241+3934	0.4 1.6	> 15.2 > 13.5
dw0240+3903 dw0240+3922 dw0241+3904*	6.3 22.2	$11.6^{+1.2,2.8}_{-1.0,1.9}$ $12.4^{+0.5,1.1}_{-0.5,0.9}$						
UGC 2165 dw0242+3838	47.5 6.2	$10.7^{+0.8,1.5}_{-0.8,1.8} \\ 9.9^{+1.2,2.6}_{-0.9,1.7}$						

Note. SBF results for candidates around NGC 1023 (D=10.4 Mpc). Objects are ordered as confirmed satellites, then possible (still unconfirmed) satellites, and then confirmed background contaminants. The SBF distances give  $+1\sigma$ ,  $+2\sigma$  errors in superscript and  $-1\sigma$ ,  $-2\sigma$  errors in subscript. Lower distance limits ( $2\sigma$ ) are given for the background objects. Objects with dashes through the measurements were too irregular, and no SBF measurement was attempted. The objects that are confirmed without SBF measurements have redshifts. Objects with asterisks are exceptions to the confirmation criteria outlined in Section 5; see text for details.

**Table 5** NGC 1156 SBF Results

	Confirmed			Possible			Background	
Name	SBF S/N	Distance (Mpc)	Name	SBF S/N	Distance (Mpc)	Name	SBF S/N	Distance (Mpc)
			dw0300 + 2514*	5.4	$6.4^{+1.7,3.8}_{-1.4,2.5}$	dw0300+2518	0.7	>7.8
			dw0301 + 2446	4.5	$3.3^{+1.7,4.4}_{-1.2,2.0}$			

Note. Same as Table 4 for NGC 1156 (D = 7.6 Mpc). Objects marked with an asterisk are discussed in detail in the text.

**Table 6** NGC 2903 SBF Results

Name	Confirmed SBF S/N	Distance (Mpc)	Name	Possible SBF S/N	Distance (Mpc)	Name	Background SBF S/N	Distance (Mpc)
dw0930+2143	5.8	$8.4^{+1.0,2.3}_{-0.8,1.5}$	dw0933+2114	1.3	$6.1^{+6.1,\infty}_{-1.9,3.0}$			
UGC 5086	10.1	$8.7^{+0.9,1.9}_{-0.9,1.7}$	dw0934+2204	2.9	$7.8^{+2.3,6.6}_{-1.6,2.8}$			

**Note.** Same as Table 4 for NGC 2903 (D = 8.0 Mpc).

galaxy from the NGC 4258 region (dw1219+4705) was confirmed to be background by Cohen et al. (2018) as well.

Figure 10 shows an example dwarf that is too low in surface brightness to be confirmed as either a satellite or background contaminant with the current data.

# A.1. NGC 1023

Table 4 gives the SBF results for candidate satellites in the field of NGC 1023. Several of the dwarfs had very strong SBF signals that put them at the distance of NGC 1023 ( $D=10.4\,\mathrm{Mpc}$ ). For four of the candidates, we did not attempt an SBF measurement, either because the candidate was too irregular or because there was too much scattered light from a nearby star. For three of these, IC 239, UGC 2157, and dw0240+3903, the candidates have redshifts from Trentham & Tully (2009) that are within

 $\pm 300 \,\mathrm{km \, s^{-1}}$  of NGC 1023. Trentham & Tully (2009) consider these three to be high-confidence members for the NGC 1023 group, and we consider these to be confirmed members as well. All three have visible SBFs that look similar to other confirmed members of similar color. Two objects, dw0237p3855 and dw0241p3904, had very strong (S/N  $\gtrsim$  20) SBF signals but distances that were slightly inconsistent with NGC 1023. As discussed in Carlsten et al. (2020a), NGC 1023 has contamination from scattered light from bright stars, due to its low galactic latitude. Both of these objects were heavily contaminated by scattered light, which is likely causing the discrepant distances. Both objects had SBFs that were visually similar to other confirmed objects, and we consider it very likely that both are genuine members of the group. We note that there are a few candidates that we consider to be background with strong fluctuation signal and  $2\sigma$  distance lower bounds only slightly

**Table 7** NGC 4258 SBF Results

Name	Confirmed SBF S/N	Distance (Mpc)	Name	Possible SBF S/N	Distance (Mpc)	Name	Background SBF S/N	Distance (Mpc)
NGC 4248	49.5	$7.6^{+0.4,0.9}_{-0.5,1.0}$	dw1218+4623	3.7	$5.4^{+1.9,4.4}_{-1.4,2.4}$	dw1214+4726	0.1	>12.3
LVJ1218+4655	7.6	$7.4^{+0.7,1.4}_{-0.6,1.0}$	dw1220+4922	4.4	$6.7^{+1.2,2.8}_{-1.0,1.8}$	dw1214+4621	4.5	>12.2
dw1219+4743	8.6	$7.6^{+0.8,1.8}_{-0.8,1.5}$	dw1220+4748	2.1	$11.3^{+5.9,\infty}_{-3.3,5.4}$	dw1214+4743	-0.3	>9.5
UGC 7356	22.8	$6.3^{+0.7,1.4}_{-0.7,1.4}$	dw1223+4848	1.3	$10.0^{+9.7,\infty}_{-2.7,4.3}$	dw1216+4709	-0.5	>9.4
dw1220+4729	5.2	$9.2^{+2.6,6.1}_{-2.0,3.5}$			<del>-</del> 1.,	dw1217+4639	0.3	>20.2
dw1220+4649	9.2	$7.9^{+1.1,2.3}_{-1.0,1.9}$				dw1217+4703*	1.8	>3.8
dw1223+4739	8.9	$7.4^{+0.8,1.8}_{-0.8,1.5}$				dw1217+4759	13.8	>8.3
		0.0,1.5				dw1217+4747	2.4	>9.8
						dw1217+4656	9.4	>10.6
						dw1218+4748	2.0	>8.1
						dw1218+4801	0.0	>7.4
						dw1219+4921	1.6	>8.5
						dw1219+4718	3.8	>10.1
						dw1219+4727	4.4	>12.7
						dw1219+4705	1.5	>13.0
						dw1219+4939	-0.8	>18.1
						dw1220+4919	3.7	>7.9
						UGC 7392	16.5	>12.7
						dw1220+4700	3.6	>11.5
						UGC 7401	7.8	>12.7
						dw1222+4755	2.8	>15.3
						dw1223+4920	2.0	>12.4

Note. Same as Table 4 for NGC 4258 (D = 7.2 Mpc). dw1217+4703 is constrained to be background by HST imaging; see text for details. Objects marked with an asterisk are discussed in detail in the text.

**Table 8** NGC 4565 SBF Results

Name	Confirmed SBF S/N	Distance (Mpc)	Name	Possible SBF S/N	Distance (Mpc)	Name	Background SBF S/N	Distance (Mpc)
dw1234+2531	9.4	$11.9^{+0.9,2.0}_{-0.9,1.8}$	dw1233+2535	2.1	$9.7^{+3.8,\infty}_{-1.8,2.8}$	dw1235+2606*	3.7	>6.9
NGC 4562*	13.3	$10.1^{+0.6,1.2}_{-0.6,1.2}$	dw1233+2543	2.4	$13.1^{+4.0,\infty}_{-2.3,3.8}$	dw1238+2536	-1.0	>16.5
IC 3571			dw1234+2627	1.1	$11.5^{+\infty,\infty}_{-3.7,5.6}$			
dw1237+2602	8.9	$11.0^{+0.8,1.6}_{-0.7,1.4}$	dw1234+2618	2.2	$7.1^{+2.6,15.6}_{-1.3,2.1}$			
		***,***	dw1235+2616	1.6	$13.2^{+8.8,\infty}_{-3.4,5.6}$			
			dw1235+2534	0.2	>10.9			
			dw1235+2637	0.6	$17.8^{+\infty,\infty}_{-9.8,13.5}$			
			dw1235+2609	1.3	$12.1^{+12.6,\infty}_{-3.5,5.4}$			
			dw1236+2616	2.7	$6.8^{+2.0,6.4}_{-1.2,2.2}$			
			dw1236+2603	1.3	$15.8^{+\infty,\infty}_{-4.5,7.0}$			
			dw1236+2634	0.3	>11.3			
			dw1237+2605	4.6	$7.7^{+1.6,3.7}_{-1.3,2.3}$			
			dw1237+2637	0.4	$16.2^{+\infty,\infty}_{-7.8,10.0}$			
			dw1237+2631	1.5	$7.4^{+5.6,\infty}_{-2.1,3.4}$			
			dw1238+2610	0.9	$10.5^{+\infty,\infty}_{-3.7,5.5}$			

Note. Same as Table 4 for NGC 4565 (D = 11.9 Mpc). Objects marked with an asterisk are discussed in detail in the text.

beyond NGC 1023 (e.g., dw0236p3752). These galaxies do not suffer from the same amount of contamination as the confirmed candidates with discrepant distances, and there is no reason to believe the SBF distance is biased in these cases.

# A.2. NGC 1156

The SBF results for NGC 1156 are shown in Table 5. We do not confirm any of the candidates to be genuine satellites. One of

the candidates is likely background, and the other two are possible satellites. One of the possible satellites (dw0300p2514) was above our fiducial S/N>5 threshold and had distance consistent with NGC 1156, but due to the galactic cirrus, we could not visually confirm this signal was actual SBF. Thus, we conservatively include this galaxy into the unconfirmed/possible satellite category. dw0300p2514 and dw0301p2446 are the two objects cataloged by Karachentsev et al. (2015) and are both promising targets for follow-up.

**Table 9** NGC 4631 SBF Results

Name	Confirmed SBF S/N	Distance (Mpc)	Name	Possible SBF S/N	Distance (Mpc)	Name	Background SBF S/N	Distance (Mpc)
	<b>SBI</b> 5/11	Distance (Mpc)	Truine	5B1 5/11	Distance (Mpc)	rune	5B1 5/11	Bistance (Mpc)
NGC 4656						UGCA 292		
dw1239+3230	7.3	$7.3^{+0.8,1.7}_{-0.7,1.2}$				dw1240+3239	9.2	>10.2
dw1239+3251	7.0	$5.9^{+1.5,3.2}_{-1.2,2.3}$				dw1242+3224	9.0	>9.6
dw1240+3216	12.0	$6.7^{+0.8,1.6}_{-0.7,1.4}$				dw1242+3231*	9.2	>6.0
dw1240+3247	9.5	$7.2^{+6.4,17.5}_{-3.4,5.3}$				dw1242+3227*	3.5	>4.8
dw1241+3251*	15.0	$6.2^{+0.5,1.0}_{-0.4,0.8}$				dw1243+3229	17.9	>8.6
NGC 4627		•••				dw1243+3232	3.6	>11.5
dw1242+3237	8.8	$7.2^{+2.9,7.1}_{-2.1,3.7}$						
dw1242+3158	6.9	$7.1^{+0.9,2.0}_{-0.8,1.6}$						
dw1243+3228	18.3	$8.1^{+0.4,0.9}_{-0.4,0.9}$						

Note. Same as Table 4 for NGC 4631 (D = 7.4 Mpc). Note that UGCA 292 is not background but significantly in the foreground of NGC 4631. Objects marked with an asterisk are discussed in detail in the text.

Table 10 NGC 4631 SBF Results Using HSC

Name	SBF S/N	Distance (Mpc)
dw1242+3227, HSC-1	3.7	>10.4
dw1243+3232, HSC-5	10	>11.0
dw1243+3228, HSC-6	18	$6.6 \pm 0.8$
dw1240+3239, HSC-7	21	>8.6
dw1241+3251, HSC-8	57	$7.0 \pm 0.8$
dw1240+3216, HSC-9	21	$7.4 \pm 0.9$
dw1242+3158, HSC-10	17	$7.0 \pm 0.8$

**Note.** SBF results for candidates around NGC 4631 (D=7.4 Mpc), using the extremely deep HSC data of Tanaka et al. (2017). For the distance lower bounds,  $2\sigma$  lower bounds are given. For the distances,  $\pm~1\sigma$  uncertainties are given.

### A.3. NGC 2903

Table 6 lists the SBF results for NGC 2903. We confirm two candidates as satellites and consider two more as possible/unconfirmed satellites. Our SBF distance of UGC 5086 is trustworthy given the smooth, round morphology of that galaxy. The other confirmed satellite, dw0930+2143, is bluer, more irregular, and H I-rich (Irwin et al. 2009), so the SBF distance is less certain. Irwin et al. (2009) measured a redshift for this dwarf via H I observations that is close to that of NGC 2903 ( $\Delta cz \sim 30 \, \mathrm{km \, s^{-1}}$ ). Given the redshift and the fact that the SBF distance is at least consistent with that of NGC 2903, we consider this dwarf a confirmed satellite.

# A.4. NGC 4258

The results for NGC 4258 are shown in Table 7. Many candidates are shown to be background, while only a few were inconclusive. Seven satellites are confirmed with the SBF. Four of these have TRGB distances that put them at the distance of NGC 4258: NGC 4248 (Sabbi et al. 2018), dw1219p4743 (Cohen et al. 2018), UGC 7356, and LVJ1218+4655 (Karachentsev et al. 2013). The SBF distances agree well in these cases. We confirm another three that had no prior distance information. Several of the confirmed background galaxies are worth discussing in detail. dw1217p4703 only has a distance lower bound of ~4 Mpc. However, Cohen et al. (2018) used *HST* imaging to show that this galaxy is in the background of

NGC 4258. Furthermore, Cohen et al. (2018) showed that dw1219p4705 and dw1220p4700 are also background, which agrees with the SBF results.

Also classified as background are two candidates that Spencer et al. (2014) considered to be confirmed satellites via their redshifts. These two are dw1214+4621 and dw1217+4759. They have fairly strong fluctuation signals, but it is visually clear that this signal is coming from their irregular morphology, not a true SBF. Even with this added power, the analysis indicated they are background galaxies. Neither show any visible SBF, which should be quite apparent given their blue colors  $(g-r\sim0.3)$ . Both of these had redshifts within 250 km s<sup>-1</sup> of NGC 4258. These results highlight the dangers of confirming satellites with only redshifts, especially if there are multiple groups at different distances projected onto the same area of sky, as is the case for NGC 4258.

Two candidate dwarfs around NGC 4258 have imaging in the HST archive: dw1219+4718 and dw1219+4727. In the HST images, these galaxies do not resolve into stars, which is expected at  $D \sim 7$  Mpc, indicating they are background. This is in line with the SBF results for these two candidates. Spencer et al. (2014) considered these both to be confirmed satellites, due to TRGB distances from Munshi & Macri (2007). It is unclear how a TRGB distance is possible since the dwarf galaxies are not resolved in the HST imaging.

The possible satellite dw1218+4623 is significantly fainter in Table 18 than in Carlsten et al. (2020a), due to a different sky-subtraction procedure we used here, which should be more accurate for this extremely LSB dwarf.

#### A.5. NGC 4565

The SBF results for NGC 4565 were inconclusive, as shown in Table 8. Only a few galaxies could be confirmed as either satellites or background due to NGC 4565's larger distance of  $D=11.9\,\mathrm{Mpc}$  and the poor seeing in the CFHT data. NGC 4562 is irregular, such that the SBF distance is likely underestimated. Given that the redshift is within 100 km s<sup>-1</sup> of NGC 4565, this galaxy is likely a companion of NGC 4565. The candidate dw1234p2531 has an SDSS redshift that is 600 km s<sup>-1</sup> less than that of NGC 4565. This candidate has a

 $<sup>\</sup>overline{^{17}}$  We note that this reference is an AAS abstract, and no further details on the TRGB distances can be found.

Table 11 NGC 5023 SBF Results

	Confirmed			Possible			Background	
Name	SBF S/N	Distance (Mpc)	Name	SBF S/N	Distance (Mpc)	Name	SBF S/N	Distance (Mpc)
			dw1314+4420	0.2	$21.0^{+\infty,\infty}_{-12.3,15.1}$	dw1310+4358	0.2	>7.6

**Note.** Same as Table 4 for NGC 5023 (D = 6.5 Mpc).

Table 12 M51 SBF Results

Name	Confirmed SBF S/N	Distance (Mpc)	Name	Possible SBF S/N	Distance (Mpc)	Name	Background SBF S/N	Distance (Mpc)
NGC 5195 NGC 5229*	29.3	7.6 <sup>+0.3,0.6</sup>	dw1327+4637 dw1327+4626 dw1328+4703 dw1330+4731 dw1331+4654 dw1331+4648	-0.6 1.4 2.7 1.6 -0.1 0.3	>4.8 $9.9^{+8.8,\infty}_{-2.7,4.2}$ $6.8^{+2.0,6.9}_{-1.2,2.1}$ $12.1^{+8.8,\infty}_{-3.6,5.7}$ >5.6 $19.1^{+\infty,\infty}_{-10.3,12.7}$	dw1327+4654 dw1328+4718 dw1329+4634 dw1329+4622* dw1330+4708* dw1330+4720 dw1332+4703	1.7 6.9 1.1 2.6 1.6 2.2 0.5	>9.1 >11.8 >13.2 >6.4 >7.0 >15.0 >9.7
						dw1332+4705 dw1333+4725	3.0	>13.1

Note. Same as Table 4 for M51 (D = 8.6 Mpc). Objects marked with an asterisk are discussed in detail in the text.

Table 13 M64 SBF Results

-	Confirmed			Possible			Background	
Name	SBF S/N	Distance (Mpc)	Name	SBF S/N	Distance (Mpc)	Name	SBF S/N	Distance (Mpc)
						dw1255+2130	3.8	>5.4

Note Same as Table 4 for M64 (D = 5.3 Mpc).

**Table 14** M104 SBF Results

Name	Confirmed SBF S/N	Distance (Mpc)	Name	Possible SBF S/N	Distance (Mpc)	Name	Background SBF S/N	Distance (Mpc)
dw1237-1125	6.4	$7.5^{+2.0,4.6}_{-1.8,3.2}$	dw1238-1208	0.7	$11.6^{+\infty,\infty}_{-5.5,7.9}$	dw1237-1110	1.8	>10.6
dw1239-1152	6.9	$8.2^{+1.1,2.4}_{-0.9,1.8}$	dw1238-1116	4.8	$9.2^{+2.4,5.7}_{-1.8,3.3}$	dw1240-1155	15.0	>16.9
dw1239-1159	6.2	$11.3^{+1.4,3.2}_{-1.2,2.3}$	dw1238-1122		•••	dw1241-1210	3.1	>12.5
dw1239-1143	21.5	$9.4^{+0.6,1.2}_{-0.6,1.3}$	dw1238-1102	2.5	$8.5^{+3.0,11.0}_{-1.8,3.1}$			
dw1239-1113	12.8	$7.9^{+1.2,2.4}_{-1.2,2.3}$	dw1239-1154	2.9	$7.3^{+2.4,6.7}_{-1.6,2.8}$			
dw1239-1120	11.7	$9.7^{+0.6,1.3}_{-0.6,1.2}$	dw1239-1118	1.7	$11.2^{+6.1,\infty}_{-2.5,4.1}$			
dw1239-1144	9.6	$9.0^{+1.5,3.1}_{-1.3,2.5}$	dw1239-1106	-0.1	>8.3			
dw1240-1118	35.4	$8.8^{+0.5,1.0}_{-0.6,1.2}$	dw1241-1123	0.0	>8.0			
dw1240-1140*	5.8	$4.2^{+0.6,1.3}_{-0.5,1.1}$	dw1241-1105	2.4	$8.4^{+2.7,10.7}_{-1.6,2.7}$			
dw1241-1131	6.1	$7.2^{+1.2,2.5}_{-1.0,2.0}$	dw1242-1116*	2.0	$14.5^{+5.9,\infty}_{-2.9,4.7}$			
dw1241-1153	6.1	$11.2^{+1.4,2.9}_{-1.2,2.2}$	dw1242-1129	1.6	$15.3^{+9.7,\infty}_{-3.8,6.2}$			
dw1241-1155	16.3	$9.0^{+0.8,1.5}_{-0.8,1.6}$	dw1243-1137	2.5	$5.3^{+1.7,6.7}_{-1.0,1.8}$			

Note. Same as Table 4 for M104 (D = 9.55 Mpc). Objects marked with an asterisk are discussed in detail in the text.

very regular, nucleated dSph morphology, which means the SBF will be trustworthy. The signal is certainly coming from the SBF of the bulk stellar population. We therefore consider this candidate as a confirmed satellite and note that the SDSS redshift might be inaccurate. Looking at the SDSS spectrum, we believe it is likely that the SDSS pipeline erroneously identified an artifact as  $H\alpha$  emission from the galaxy, leading to a spurious redshift. IC 3571 was too irregular to attempt an

SBF measurement but has a redshift consistent with NGC 4565, so we consider it a likely satellite. Zschaechner et al. (2012) noted a bridge in H I between this galaxy and NGC 4565, in line with this conclusion. The candidate dw1235  $\pm$ 2606 is located directly in the middle of the H I warp on the northwest edge of the disk of NGC 4565. Radburn-Smith et al. (2014) used *HST* observations to show that there is a clump of young ( $\pm$ 600 Myr) stars located in the warp, which is

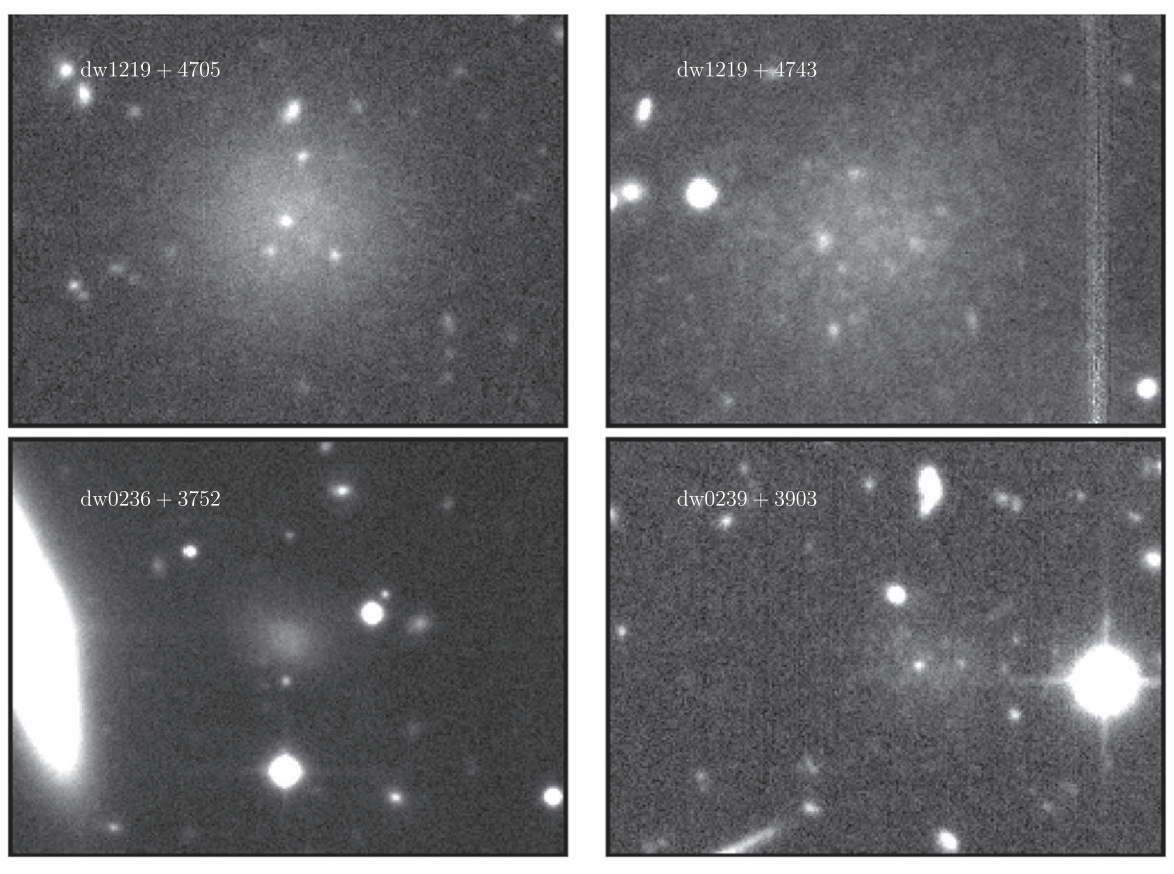


**Figure 9.** The left column shows examples of galaxies that we constrain to be background in the SBF analysis, and the right column shows examples of confirmed satellites. The top row of galaxies are from the NGC 4258 (D = 7.2 Mpc) region, and the bottom row are from NGC 1023 (D = 10.4 Mpc). The real satellites exhibit clearly visible SBF, while the background galaxies are nearly perfectly smooth. The pairs of galaxies from each region are roughly matched in surface brightness, size, and color. Each image is 45'' wide. The top row is the r band, and the bottom row is i.

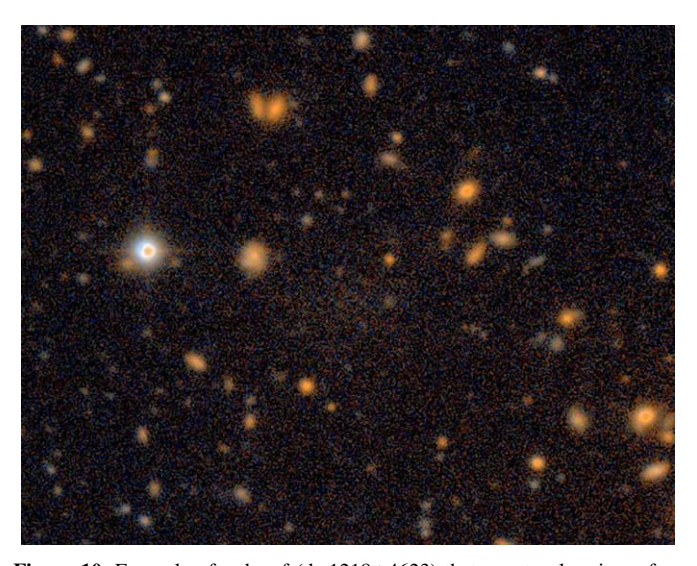


**Figure 10.** Example of a dwarf (dw1218+4623) that was too low in surface brightness to be either confirmed as a satellite or constrained to be background.

likely what our detection algorithm identified as a candidate satellite. They argue that these stars formed in situ in the warp. In this case, this candidate should not be considered a real satellite, and we include it in the "background" category. We note that Gilhuly et al. (2020) interpret this candidate as the core of an accreted satellite whose disruption produced other LSB structures seen in their data. However, since

Radburn-Smith et al. (2014) did not find an old stellar population along with the young, the in situ star formation scenario seems more likely.

# A.6. NGC 4631

Table 9 shows the SBF analysis results for NGC 4631. There are 10 confirmed satellites, and no candidates that are possible/ unconfirmed. dw1242p3231 is an exception to our usual criteria. It has a strong SBF signal that is consistent with being at the distance of NGC 4631. However, it is a small, compact system that is projected onto the outskirts of the disk of NGC 4631. The SBF signal appears to be coming from the outer disk stars of NGC 4631. This dwarf has archival HST imaging in which it does not resolve into stars, strongly suggesting that it is background. Thus we include it in the "background" category. The confirmed candidate dw1241p3251 is barely inconsistent with the distance of NGC 4631 within  $2\sigma$ . This galaxy is somewhat non-Sérsic, so the distance is likely underestimated. This galaxy also has a redshift consistent with NGC 4631 ( $\Delta cz \sim 60 \, \mathrm{km \, s^{-1}}$ ). We do not attempt an SBF measurement for NGC 4627, but it is clear this galaxy is physically associated with NGC 4631, both from redshift and ongoing tidal disruption. The SBF distance error bars for dw1240p3247 are large (±4 Mpc), even though the SBF signal is strong. This is driven by the large error on the measured color of this galaxy. This galaxy is the progenitor of a large tidal stream around NGC 4631 and is clearly physically associated (Martínez-Delgado et al. 2015). UGCA 292 is a foreground dwarf galaxy, as evidenced by both a TRGB distance (Dalcanton et al. 2009) and the SBF distance. Several of the background galaxies are surprising given their LSB, spheroidal morphology, and no clear massive host in the background of NGC 4631. We note that the apparent SBF signal coming from the confirmed background galaxy dw1243 +3229 is from its irregular morphology and not a real SBF. dw1243+3229 has a redshift that is>250 km s<sup>-1</sup> larger than that of NGC 4631 and is almost certainly background. dw1242p3227 was too faint to have a robust distance constraint from the CFHT data alone.

Recently, Karunakaran et al. (2020) reported an HI redshift for dw1239+3230 of 613 km s<sup>-1</sup>, quite close to the systemic velocity of NGC 4631 (606 km s<sup>-1</sup>), reinforcing the SBF result that this dwarf is physically associated with NGC 4631.

To confirm our SBF results for many of the candidates found around NGC 4631, we used the much deeper HSC data of Tanaka et al. (2017). The CFHT/Megacam data we used for this region had  $\sim 1$  hr exposure times for most of the field. The HSC data, on the other hand, has  $\sim 10$  hr exposure times (on a telescope with twice the aperture of CFHT). The CFHT data has a wider field, however, so we identify a few candidates that were outside of the footprint of Tanaka et al. (2017).

To use the HSC data, we downloaded the raw data from the Subaru archive<sup>18</sup> and reduced it using version 4 of the HSC pipeline (Bosch et al. 2018). To save computing time, we only downloaded and stacked  $\sim$ 3 hr of g- and i-band data each. We then did an SBF analysis on cutouts for several of the candidates that are in the HSC footprint. Because the HSC pipeline does a local (128 × 128 pixel grid) background estimation and subtraction, we did not attempt an SBF analysis for dw1240+3247 or dw1242+3237. These two dwarfs are large and have LSB (and also near NGC 4631 in projection), and the pipeline sky subtraction was clearly oversubtracting some diffuse light from these galaxies. This oversubtraction can have a significant effect on the SBF results, so we did not look at these dwarfs. To turn the measured SBF magnitudes into distances, we used the i-band calibration of Carlsten et al. (2019b). As our goal is mostly just to confirm the CFHT results, we do not bother with any filter conversions to convert the CFHT/Megacam calibration into the HSC filter system. Both filter systems are based on SDSS filters, so they should not differ by much. We assume a 0.1 mag uncertainty in the g - i color of each galaxy.

Table 10 gives the SBF results for the HSC data. The results are remarkably consistent with what we found with the CFHT data. The HSC data confirm the surprising result above that several of the dSphs are actually background. These objects are prototypical dSphs and were clustered around NGC 4631. There does not appear to be an obvious possible massive host for these objects behind NGC 4631. The HSC data confirm that dw1243+3228, dw1240+3239, and dw1242+3227 are all background. In the CFHT data, the SBF results were ambiguous for dw1242+3227 given its extreme faintness, but with the HSC data, it is clearly background. For the remaining objects, the HSC data confirm them to be at the distance of NGC 4631 with much higher S/N than was possible with the CFHT data.

The consistency between the HSC results and the shallower CFHT results gives us confidence in the distance constraints we derive for candidates around other hosts in the CFHT data.

#### A.7. NGC 5023

Due to the shallower data for NGC 5023, we do not confirm any candidates as satellites. As listed in Table 11, one candidate is likely background, while the other is unconstrained from the SBF analysis.

#### A.8. M51

Table 12 gives the SBF results for the candidates found around M51. NGC 5229 shows a strong SBF and is clearly not far in the background. Sharina et al. (1999) give a brightest-stars distance of 5.1 Mpc, which would put it significantly in the foreground of M51. However, they quote a  $\pm 2$  Mpc uncertainty in that distance. Due to NGC 5229's disky morphology, the SBF results are not trustworthy. Still, we find an SBF distance of  $\sim$ 7.7 Mpc, which is likely somewhat underestimated and, therefore, suggestive of association with M51. The redshift of this galaxy is also consistent with being bound to M51 ( $\Delta cz \sim 100 \,\mathrm{km \, s^{-1}}$ ). Thus, we tentatively include this galaxy as a confirmed satellite, but we note that a firm confirmation will likely require an HST TRGB distance. There is one candidate, dw1329+4622, that had inconclusive SBF results but had a redshift that indicates it is background from Dalcanton et al. (1997). dw1330+4708 also had inconclusive SBF results but has archival HST imaging in which it is not resolved, strongly suggesting it is background.

#### A.9. M64

Carlsten et al. (2020a) only found one candidate satellite in the vicinity of M64, at least partly due to the small survey footprint and shallow data. As shown in Table 13, the SBF analysis indicates that this dwarf is background.

## A.10. M104

The SBF results for M104 are shown in Table 14. Due to the good seeing of the data and brightness of SBF in the i band, we were able to confirm a large number of the candidates to be at the distance of M104 (D = 9.55 Mpc). A few of the dwarfs were exceptions to our usual classification criteria. dw1240m1140 showed a strong SBF signal that put it significantly in the foreground. However, this dwarf is located very close to M104 in projection, and the halo of M104 could be adding signal to the SBF measurement, causing the distance to be underestimated. Considering its dSph morphology, proximity to M104, and SBF, we suspect this dwarf is physically associated with M104, and we include it in the "confirmed" category. The SBF measurement of dw1242m1116 indicated that it is background, but this dwarf only partially fell on a chip in the MegaCam data, which might make the measurement unreliable. Thus, we include this dwarf in the unconfirmed/possible category. dw1238m1122 was contaminated by a large saturation spike in the MegaCam data, so we did not attempt an SBF measurement of this galaxy.

# Appendix B r-band SBF Calibration

In Figure 11 we show the conversions between  $\bar{M}_r$  and  $\bar{M}_r$  and g-i and g-r that we use to derive the *r*-band calibration used in this work. The color–color transformation has quite low

https://smoka.nao.ac.jp/fssearch.jsp

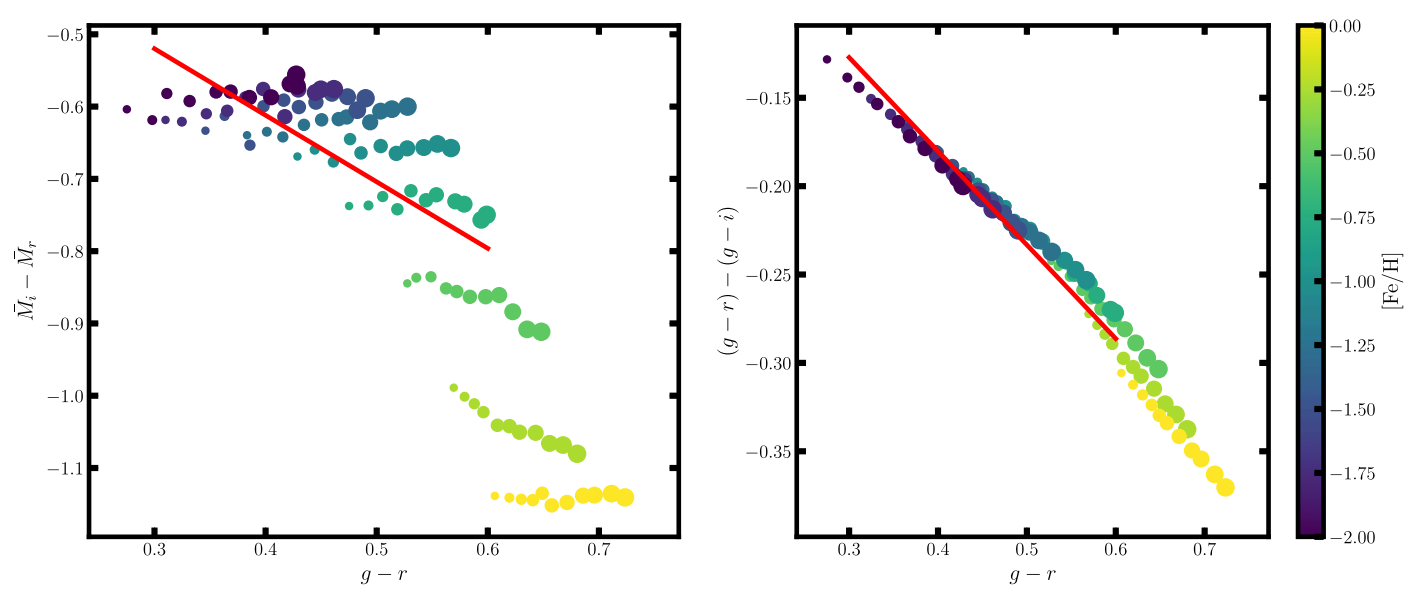


Figure 11. Filter conversions used in deriving the r-band calibration. The points show the SSP models where point size represents age (3 < age < 10 Gyr), with the biggest sizes indicating the oldest ages. The red lines show the fits that are used in the conversion.

scatter. The SBF magnitude transformation looks significantly worse, but we note that the galaxies we analyze in this paper all have  $g-r \lesssim 0.6$  where the scatter is  $\sim 0.1$  mag. An error of 0.1 mag in the conversion between i- and r-band SBF magnitudes will only introduce a 5% error in distance, which is less than the usual distance uncertainties we find in the SBF analysis. While a quadratic looks to be more appropriate for the SBF magnitude conversion, using a linear fit has the attractive property that the  $\bar{M}_r$  versus g-r relation will be linear as well.

# Appendix C Local Volume Satellite Systems

## C.1. Systems Surveyed in the Current Work

Tables 15–23 list the properties of the confirmed and possible satellites in the systems that we surveyed in Section 5 of this work. Position, magnitudes, and sizes are given for all system members, including the hosts. The host photometry

comes from Gil de Paz et al. (2007). For the satellites, the host distance is used to calculate absolute magnitudes and physical sizes and not the individual SBF distances. We are not able to resolve the 3D structure of these groups with the precision of SBF, and using the SBF distances would simply increase the scatter in size and magnitude.

In Carlsten et al. (2020a), R-band photometry from Trentham & Tully (2009) was used for some of the largest candidates around NGC 1023. We convert from R to V using  $V \approx R + 0.56$  (Fukugita et al. 1995). The rest of the dwarf photometry comes from Carlsten et al. (2020a). Errors are estimated from injecting mock galaxies into the data and measuring the spread in the recovered photometry.

## C.2. Surveyed Systems from the Literature

Tables 24–29 list the members of the previously surveyed systems. Positions, distances, and luminosities are given for all satellites, along with references.

Table 15 NGC 1023 Satellites

Name	RA (deg)	Dec (deg)	$M_g$	$M_V$	g-i	r <sub>e</sub> (pc)
NGC 1023	40.1000	39.0633		-20.9	•••	
			Confirmed Satelli	tes		
dw0233+3852	38.4278	38.8722	$-11.7 \pm 0.27$	$-11.92 \pm 0.27$	$0.52 \pm 0.11$	$745.3 \pm 49.7$
dw0235+3850	38.976	38.8362	$-13.27 \pm 0.15$	$-13.52 \pm 0.15$	$0.6 \pm 0.01$	$532.0 \pm 86.4$
IC 239	39.1161	38.969	-18.8 **	-19.1 **	0.72**	4003.0**
dw0237+3855	39.3276	38.9331	$-14.9 \pm 0.11$	$-15.19 \pm 0.11$	$0.72 \pm 0.01$	$992.1 \pm 98.3$
dw0237+3836	39.4144	38.6003	$-11.86 \pm 0.17$	$-12.12 \pm 0.17$	$0.65\pm0.07$	$533.0 \pm 63.0$
dw0239+3926	39.8328	39.4339	$-12.12 \pm 0.14$	$-12.42 \pm 0.14$	$0.75\pm0.02$	$1305.3 \pm 103.8$
dw0239+3903	39.8436	39.0554	$-9.02 \pm 0.49$	$-9.3 \pm 0.49$	$0.7 \pm 0.18$	$228.8 \pm 44.0$
dw0239+3902	39.946	39.0473	$-9.46 \pm 0.09$	$-9.79 \pm 0.09$	$0.82 \pm 0.02$	$267.3 \pm 15.8$
UGC 2157	40.1043	38.563	-16.1 **	-16.4 **	0.66**	1986.6**
dw0240+3854	40.1374	38.9004	$-13.32 \pm 0.03$	$-13.49 \pm 0.03$	$0.42 \pm 0.01$	$330.2 \pm 3.3$
dw0240+3903	40.1544	39.0593		-15.1	•••	
dw0240+3922	40.1649	39.3792	$-13.4 \pm 0.07$	$-13.51 \pm 0.07$	$0.26 \pm 0.01$	$644.2 \pm 53.4$
dw0241+3904	40.2515	39.0724	$-14.16 \pm 0.03$	$-14.34 \pm 0.03$	$0.42 \pm 0.01$	$781.8 \pm 25.9$
UGC 2165	40.3145	38.7441	$-15.88 \pm 0.04$	$-16.23 \pm 0.04$	$0.89 \pm 0.01$	$1261.0 \pm 40.3$
dw0242 + 3838	40.6026	38.6351	$-9.24 \pm 0.11$	$-9.43 \pm 0.11$	$0.45\pm0.06$	$181.0 \pm 12.3$
			Possible Satellite	es		
dw0238+3805	39.6707	38.0851	-13.4 **	-13.6 **	0.57**	656.2**
dw0239+3910	39.8421	39.173	$-7.74 \pm 0.24$	$-8.01 \pm 0.24$	$0.66 \pm 0.14$	$227.6 \pm 22.7$
dw0241+3852	40.3357	38.8673	$-8.75 \pm 0.44$	$-9.0 \pm 0.44$	$0.64 \pm 0.12$	$313.9 \pm 43.5$
dw0241+3829	40.4758	38.4982	$-10.6 \pm 0.13$	$-10.85 \pm 0.13$	$0.64 \pm 0.02$	$300.1 \pm 30.1$
dw0242+3757	40.5922	37.9568	$-7.88 \pm 0.28$	$-8.24 \pm 0.29$	$0.9 \pm 0.12$	$124.6 \pm 19.7$
dw0243+3915	40.979	39.2557	$-11.13 \pm 0.13$	$-11.43 \pm 0.13$	$0.74\pm0.04$	$313.7 \pm 47.2$

**Note.** Confirmed and possible satellites in the NGC 1023 system. The V band photometry is converted from our photometry, as described in \*\*\*. The asterisks mark systems which were not well fit by a Sérsic profile and the photometry might be biased. The photometry for dw0240+3903 comes from \*\*\*.

**Table 16** NGC 1156 Satellites

Name	R.A. (deg)	Decl. (deg)	$M_g$	$M_V$	g-r	r <sub>e</sub> (pc)
NGC 1156	44.9263	25.2378	•••	-18.3		
			Confirmed Satellite	s		
			Possible Satellites			
dw0300+2514 dw0301+2446	45.0743 45.3841	25.2489 24.7832	$-10.39 \pm 0.5$ $-10.36 \pm 0.35$	$-10.66 \pm 0.5$ $-10.76 \pm 0.37$	$0.46 \pm 0.11 \\ 0.69 \pm 0.21$	$213.7 \pm 31.0$ $387.7 \pm 49.8$

Note. Confirmed and possible satellites in the NGC 1156 system.

**Table 17** NGC 2903 Satellites

Name	R.A. (deg)	Decl. (deg)	$M_g$	$M_V$	g-r	$r_e$ (pc)
NGC 2903	143.0421	21.5008	•••	-20.47		
			Confirmed Satellites	3		
dw0930+2143	142.6666	21.7242	$-10.86 \pm 0.08$	$-11.01 \pm 0.09$	$0.26 \pm 0.03$	$297.6 \pm 21.5$
UGC 5086	143.2034	21.4656	$-13.79 \pm 0.08$	$-14.13 \pm 0.08$	$0.58\pm0.03$	$653.6\pm30.3$
			Possible Satellites			
dw0933+2114	143.3686	21.2334	$-8.1 \pm 0.49$	$-8.43 \pm 0.49$	$0.56 \pm 0.1$	$186.7 \pm 24.1$
dw0934+2204	143.5918	22.0816	$-10.1\pm0.1$	$-10.28 \pm 0.12$	$0.31 \pm 0.09$	$143.9\pm10.8$

Note. Confirmed and possible satellites in the NGC 2903 system.

Table 18 NGC 4258 Satellites

Name	R.A. (deg)	Decl. (deg)	$M_g$	$M_V$	g-r	$r_e$ (pc)
NGC 4258	184.7396	47.3040	•••	-20.94		
			Confirmed Satellites	3		
NGC 4248	184.4591	47.4093	$-16.57 \pm 0.02$	$-16.86 \pm 0.02$	$0.51 \pm 0.01$	$1824.1 \pm 17.1$
LVJ1218+4655	184.5465	46.9172	$-12.8 \pm 0.02$	$-12.93 \pm 0.02$	$0.22 \pm 0.01$	$564.8 \pm 20.4$
dw1219+4743	184.7756	47.7304	$-10.76 \pm 0.16$	$-11.0 \pm 0.16$	$0.41 \pm 0.04$	$361.4 \pm 43.8$
UGC 7356	184.7874	47.09	$-14.0 \pm 0.09$	$-14.32 \pm 0.1$	$0.53 \pm 0.05$	$896.4 \pm 60.2$
dw1220+4729 <sup>†</sup>	185.1258	47.4907	$-9.16 \pm 0.35$	$-9.33 \pm 0.35$	$0.28 \pm 0.12$	$479.8 \pm 68.2$
dw1220+4649	185.2287	46.8301	$-10.47 \pm 0.13$	$-10.76 \pm 0.14$	$0.5 \pm 0.05$	$402.9 \pm 23.6$
dw1223+4739	185.9424	47.6591	$-11.27 \pm 0.09$	$-11.54 \pm 0.09$	$0.45\pm0.04$	$601.6\pm80.9$
			Possible Satellites			
dw1218+4623	184.5111	46.3848	$-7.44 \pm 0.52$	$-7.73 \pm 0.53$	$0.49 \pm 0.13$	$259.7 \pm 60.5$
dw1220+4922	185.0599	49.381	$-9.34 \pm 0.09$	$-9.59 \pm 0.09$	$0.44 \pm 0.05$	$201.3 \pm 9.7$
dw1220+4748	185.2324	47.8165	$-7.31 \pm 0.38$	$-7.52 \pm 0.39$	$0.36 \pm 0.13$	$159.2 \pm 32.2$
dw1223+4848	185.8035	48.8157	$-8.39\pm0.22$	$-8.71 \pm 0.22$	$0.55\pm0.07$	$164.1 \pm 21.7$

Note. Confirmed and possible satellites in the NGC 4258 system. Satellites marked with  $\dagger$  are below the  $\mu_{0,V} = 26.5$  mag arcsec<sup>-2</sup> surface brightness limit we assume throughout this work.

**Table 19** NGC 4565 Satellites

Name	R.A. (deg)	Decl. (deg)	$M_{g}$	$M_V$	g-r	$r_e \  m (pc)$
NGC 4565	189.0866	25.9877	•••	-21.8		
			Confirmed Satellite	es		
dw1234+2531	188.6007	25.5223	$-13.73 \pm 0.03$	$-14.03 \pm 0.03$	$0.51 \pm 0.01$	$1148.5 \pm 28.2$
NGC 4562	188.8948	25.8504	$-16.88 \pm 0.01$	$-17.15 \pm 0.01$	$0.46 \pm 0.01$	$2043.7 \pm 8.0$
IC 3571	189.0835	26.0843	$-13.8^{**}$	$-13.9^{**}$	0.16**	491.1**
dw1237+2602	189.2549	26.036	$-12.41 \pm 0.06$	$-12.64 \pm 0.06$	$0.39 \pm 0.01$	$484.5 \pm 33.6$
			Possible Satellites	8		
dw1233+2535	188.2958	25.5987	$-11.73 \pm 0.07$	$-11.97 \pm 0.07$	$0.4 \pm 0.01$	$269.3 \pm 11.5$
dw1233+2543	188.3266	25.7264	$-9.81 \pm 0.1$	$-10.01 \pm 0.1$	$0.35 \pm 0.03$	$238.9 \pm 11.6$
dw1234+2627	188.6043	26.4546	$-8.53 \pm 0.26$	$-8.8 \pm 0.26$	$0.47 \pm 0.09$	$212.4 \pm 33.1$
dw1234+2618	188.7398	26.3141	$-10.13 \pm 0.06$	$-10.32 \pm 0.06$	$0.33 \pm 0.03$	$267.8 \pm 10.0$
dw1235+2616	188.843	26.2706	$-9.84 \pm 0.13$	$-10.15 \pm 0.13$	$0.52 \pm 0.03$	$259.1 \pm 51.5$
dw1235+2534	188.9063	25.5701	$-8.45 \pm 0.21$	$-8.66 \pm 0.22$	$0.36 \pm 0.09$	$246.2 \pm 45.2$
dw1235+2637	188.9259	26.6208	$-8.7 \pm 0.31$	$-8.74 \pm 0.34$	$0.07 \pm 0.25$	$387.9 \pm 97.8$
dw1235+2609	188.98	26.1654	$-7.64 \pm 0.21$	$-7.87 \pm 0.22$	$0.4 \pm 0.08$	$172.8 \pm 30.7$
dw1236+2616	189.0246	26.2738	$-7.5 \pm 0.15$	$-7.78 \pm 0.16$	$0.48 \pm 0.06$	$172.4 \pm 10.8$
dw1236+2603	189.1049	26.0552	$-8.93 \pm 0.19$	$-9.09 \pm 0.2$	$0.28 \pm 0.07$	$258.2 \pm 41.7$
dw1236+2634	189.2441	26.5786	$-9.2 \pm 0.18$	$-9.5 \pm 0.18$	$0.51 \pm 0.04$	$272.2 \pm 29.8$
dw1237+2605	189.3617	26.0858	$-10.6 \pm 0.32$	$-10.85 \pm 0.32$	$0.42 \pm 0.07$	$761.0 \pm 194.6$
dw1237+2637	189.4283	26.6243	$-10.15 \pm 0.08$	$-10.46 \pm 0.08$	$0.53 \pm 0.06$	$281.9 \pm 32.5$
dw1237+2631	189.4776	26.5189	$-7.86 \pm 0.36$	$-8.12 \pm 0.37$	$0.44 \pm 0.09$	$155.6 \pm 18.6$
dw1238+2610	189.6649	26.1669	$-8.39 \pm 0.29$	$-8.65 \pm 0.29$	$0.44 \pm 0.09$	$270.7 \pm 29.1$

Note. Confirmed and possible satellites in the NGC 4565 system.

**Table 20** NGC 4631 Satellites

Name	R.A. (deg)	Decl. (deg)	$M_g$	$M_V$	g-r	$r_e \  m (pc)$
NGC 4631	190.5334	32.5415	•••	-20.24		
			Confirmed Satellite	es		
dw1239+3230	189.7708	32.5043	$-10.19 \pm 0.09$	$-10.31 \pm 0.09$	$0.2 \pm 0.03$	$230.2 \pm 18.0$
dw1239+3251	189.8315	32.8609	$-9.31 \pm 0.31$	$-9.65 \pm 0.31$	$0.58 \pm 0.11$	$490.4 \pm 98.9$
dw1240+3216	190.2209	32.2822	$-10.35 \pm 0.1$	$-10.64 \pm 0.1$	$0.5 \pm 0.05$	$311.5 \pm 20.0$
dw1240+3247	190.2437	32.7903	$-13.28 \pm 0.64$	$-13.61 \pm 0.67$	$0.57 \pm 0.33$	$2549.6 \pm 684.5$
dw1241+3251	190.4464	32.8576	$-13.65 \pm 0.05$	$-13.74 \pm 0.05$	$0.14 \pm 0.02$	$644.4 \pm 33.3$
NGC 4627	190.4987	32.5739	$-16.5^{**}$	$-16.7^{**}$	0.37**	973.9**
dw1242+3237 <sup>a</sup>	190.5256	32.6219	$-10.47 \pm 0.43$	$-10.71 \pm 0.44$	$0.4 \pm 0.17$	$660.6 \pm 99.1$
dw1242+3158	190.6308	31.9692	$-10.22 \pm 0.1$	$-10.51 \pm 0.1$	$0.5 \pm 0.05$	$295.2 \pm 22.0$
dw1243+3228	190.8534	32.482	$-12.62 \pm 0.03$	$-12.88 \pm 0.03$	$0.45 \pm 0.01$	$593.9 \pm 10.7$
NGC 4656	190.9905	32.1681	•••	-18.9		

Possible Satellites

**Note.** Confirmed and possible satellites in the NGC 4631 system. Photometry for NGC 4565 comes from Gil de Paz et al. (2007). Satellites marked with a are below the  $\mu_{0,V} = 26.5$  mag arcsec<sup>-2</sup> surface brightness limit we assume throughout this work.

Table 21 NGC 5023 Satellites

Name	R.A. (deg)	Decl. (deg)	$M_g$	$M_V$	g-i	r <sub>e</sub> (pc)
NGC 5023	198.0525	44.0412	•••	-14.9		
			Confirmed Satellites			
dw1314+4420	198.6435	44.3342	Possible Satellites $-6.67 \pm 0.16$	$-6.91 \pm 0.18$	$0.58 \pm 0.18$	$96.4 \pm 8.2$

Note. Confirmed and possible satellites in the NGC 5023 system.

Table 22 M51 Satellites

Name	R.A. (deg)	Decl. (deg)	$M_g$	$M_V$	g-r	$r_e$ (pc)
M51	202.4696	47.1952	•••	-21.38	•••	
			Confirmed Satellites			
NGC 5195	202.4983	47.2661		-20.2		
NGC 5229	203.5123	47.9138	-15.9**	$-16.2^{**}$	0.4**	1543.2**
			Possible Satellites			
dw1327+4637	201.794	46.6323	$-8.33 \pm 0.24$	$-8.66 \pm 0.24$	$0.56 \pm 0.11$	$190.4 \pm 42.7$
dw1327+4626	201.971	46.4413	$-8.92 \pm 0.2$	$-9.14 \pm 0.2$	$0.38 \pm 0.03$	$163.6 \pm 31.7$
dw1328+4703	202.103	47.0652	$-9.27 \pm 0.11$	$-9.62 \pm 0.11$	$0.59 \pm 0.04$	$279.9 \pm 17.5$
dw1330+4731 <sup>a</sup>	202.6411	47.5259	$-9.67 \pm 0.15$	$-9.89 \pm 0.16$	$0.37 \pm 0.11$	$519.0 \pm 50.8$
dw1331+4654	202.7843	46.9077	$-7.45 \pm 0.08$	$-7.77 \pm 0.1$	$0.55 \pm 0.08$	$129.4 \pm 4.1$
dw1331+4648	202.7983	46.8159	$-9.07 \pm 0.16$	$-9.32 \pm 0.16$	$0.43 \pm 0.04$	$283.1 \pm 42.5$

**Note.** Confirmed and possible satellites in the M51 system. Photometry for NGC 5195 comes from Gil de Paz et al. (2007). Satellites marked with  $\mu_{0,V} = 26.5$  mag arcsec<sup>-2</sup> surface brightness limit we assume throughout this work.

Table 23 M104 Satellites

Name	R.A. (deg)	Decl. (deg)	$M_g$	$M_V$	g-i	$r_e \  m (pc)$
M104	189.9976	-11.6231	•••	-22.02		•••
			Confirmed Satellite	es		
dw1237-1125	189.2988	-11.433	$-11.62 \pm 0.06$	$-12.02 \pm 0.1$	$0.99 \pm 0.23$	$463.5 \pm 17.9$
dw1239-1152	189.7877	-11.8768	$-8.09 \pm 0.22$	$-8.29 \pm 0.23$	$0.49 \pm 0.1$	$229.0 \pm 33.4$
dw1239-1159	189.7877	-11.9867	$-11.0 \pm 0.22$	$-11.21 \pm 0.22$	$0.52 \pm 0.08$	$653.8 \pm 117.3$
dw1239-1143	189.8136	-11.7189	$-13.38 \pm 0.03$	$-13.7 \pm 0.03$	$0.8 \pm 0.01$	$577.7 \pm 11.9$
dw1239-1113	189.8864	-11.2267	$-11.9 \pm 0.27$	$-12.23 \pm 0.27$	$0.84 \pm 0.13$	$799.9 \pm 119.3$
dw1239-1120	189.9645	-11.3413	$-10.49 \pm 0.1$	$-10.73 \pm 0.1$	$0.59 \pm 0.03$	$320.6 \pm 29.2$
dw1239-1144	189.9787	-11.746	$-12.57 \pm 0.29$	$-12.85 \pm 0.3$	$0.7 \pm 0.14$	$1039.4 \pm 208.2$
dw1240-1118	190.0391	-11.3138	$-14.0 \pm 0.03$	$-14.32 \pm 0.03$	$0.81 \pm 0.01$	$697.1 \pm 16.9$
dw1240-1140	190.0733	-11.6794	$-10.63 \pm 0.45$	$-11.01 \pm 0.45$	$0.94 \pm 0.06$	$575.2 \pm 115.1$
dw1241-1131	190.2617	-11.5288	$-10.12 \pm 0.17$	$-10.44 \pm 0.18$	$0.8 \pm 0.11$	$423.3 \pm 40.8$
dw1241-1153	190.3002	-11.8916	$-11.53 \pm 0.19$	$-11.82 \pm 0.19$	$0.72 \pm 0.06$	$654.1 \pm 86.1$
dw1241-1155	190.328	-11.9252	$-12.42 \pm 0.11$	$-12.72 \pm 0.11$	$0.75\pm0.06$	$786.1 \pm 54.6$
			Possible Satellites			
dw1238-1208	189.5926	-12.1356	$-7.27 \pm 0.15$	$-7.52 \pm 0.21$	$0.61 \pm 0.37$	$155.8 \pm 10.0$
dw1238-1116	189.6296	-11.2738	$-8.83 \pm 0.34$	$-9.0 \pm 0.35$	$0.4 \pm 0.2$	$270.6 \pm 51.3$
dw1238-1122	189.6402	-11.3681	$-12.3^{**}$	$-12.6^{**}$	0.84**	648.9**
dw1238-1102	189.7429	-11.036	$-9.18 \pm 0.25$	$-9.38 \pm 0.26$	$0.5 \pm 0.16$	$234.8 \pm 26.1$
dw1239-1154	189.8434	-11.9066	$-8.47 \pm 0.45$	$-8.76 \pm 0.46$	$0.73 \pm 0.18$	$386.1 \pm 60.9$
dw1239-1118	189.9059	-11.3092	$-8.31 \pm 0.13$	$-8.54 \pm 0.14$	$0.58 \pm 0.1$	$184.3 \pm 18.5$
dw1239-1106	189.9245	-11.1001	$-9.02 \pm 0.18$	$-9.27 \pm 0.19$	$0.61 \pm 0.09$	$272.7 \pm 39.9$
dw1241-1123	190.2897	-11.3987	$-8.82 \pm 0.38$	$-9.14 \pm 0.38$	$0.8 \pm 0.09$	$565.5 \pm 116.6$
dw1241-1105	190.2925	-11.0972	$-8.01 \pm 0.11$	$-8.4 \pm 0.11$	$0.99 \pm 0.06$	$104.4 \pm 10.7$
dw1242-1116	190.6825	-11.2739	$-11.81 \pm 0.22$	$-12.05 \pm 0.22$	$0.58 \pm 0.07$	$1127.6 \pm 213.2$
dw1242-1129	190.7067	-11.4893	$-8.82 \pm 0.23$	$-9.11 \pm 0.24$	$0.73 \pm 0.13$	$150.5 \pm 22.3$
dw1243-1137	190.8251	-11.6258	$-8.34 \pm 0.19$	$-8.75\pm0.2$	$1.03 \pm 0.07$	$203.7 \pm 36.1$

Note. Confirmed and possible satellites in the M104 system.

Table 24 MW Satellites

		MW, $M_* =$	$5\times10^{10}M_{\odot}$		
Name	R.A. (deg)	Decl. (deg)	m-M (mag)	$M_V$	Source
MW		•••		-21.4	•••
LMC	05:23:34	-69:45:22	$18.477 \pm 0.026$	-18.1	1,12,1
SMC	00:52:44	-72:49:43	$18.91 \pm 0.1$	-16.7	1,13,1
Sgr	18:55:19	-30:32:43	$17.13 \pm 0.11$	-13.5	1, 2, 14
Fornax	02:39:59	-34:26:57	$20.72 \pm 0.04$	-13.5	1, 3, 1
Leo 1	10:08:28	+12:18:23	$22.15 \pm 0.1$	-11.8	1, 4, 14
Sculptor	01:00:09	-33:42:33	$19.64 \pm 0.13$	-10.8	1, 5, 14
Leo 2	11:13:28	+22:09:06	$21.76 \pm 0.13$	-9.7	1, 6, 14
Sextans*	10:13:03	-01:36:53	$19.67 \pm 0.15$	-8.7	1, 7, 14
Ursa Minor	15:09:08	+67:13:21	$19.40 \pm 0.11$	-9.0	1, 8, 1
Carina	06:41:36	-50:57:58	$20.08 \pm 0.08$	-9.4	1, 9, 14
Draco	17:20:12	+57:54:55	$19.49 \pm 0.17$	-8.7	1, 10, 14
CVn 1*	13:28:03	+33:33:21	$21.62 \pm 0.05$	-8.8	1, 11, 14

Note. Known satellites of the MW. Satellites marked with \* are below the  $\mu_{0,V}=26.5$  mag arcsec<sup>-2</sup> surface brightness limit we assume throughout this work. Distance modulus is given relative to the Sun (not the galactic center). Sources for position, distance, and luminosity (in order): (1) McConnachie (2012),(2) Hamanowicz et al. (2016), (3) Rizzi et al. (2007), (4) Stetson et al. (2014), (5) Martínez-Vázquez et al. (2016); Pietrzyński et al. (2008), (6) Bellazzini et al. (2005), Gullieuszik et al. (2008), (7) Mateo et al. (1995), (8) Carrera et al. (2002), Bellazzini et al. (2002), (9) Coppola et al. (2015), Vivas & Mateo (2013), (10) Bonanos et al. (2004), Kinemuchi et al. (2008), (11) Kuehn et al. (2008), (12) Pietrzyński et al. (2019), (13) Hilditch et al. (2005), (14) Muñoz et al. (2018).

Table 25 M31 Satellites

M31, $M_* = 10.3 \times 10^{10} M_{\odot}$ (Sick et al. 2015)					
Name	R.A. (deg)	Decl. (deg)	$D_{\odot}$ (Mpc)	$M_V$	Source
M31	00:42:44	+41:16:09	0.780	-22	1, 2, 3
M33	01:33:50	+30:39:37	0.821	-18.8	1, 2, 1
NGC 205	00:40:22	+41:41:07	$0.824 \pm 0.027$	-16.5	1, 4, 1
M32	00:42:41	+40:51:55	$0.781 \pm 0.02$	-16.3	1, 5, 1
NGC 147	00:33:12	+48:30:32	0.713	-15.8	1, 2, 1
IC 10	00:20:17	+59:18:14	$0.798 \pm 0.029$	-15.0	1, 6, 1
NGC 185	00:38:58	+48:20:15	0.619	-15.5	1, 2, 1
AndVII	23:26:31	+50:40:33	$0.763 \pm 0.035$	-13.2	1, 4, 1
AndXXXII	00:35:59.4	+51:33:35	$0.871_{0.016}^{0.018}$	-12.5	1, 8, 1
AndII	01:16:29.8	+33:25:09	$0.679 \pm 0.040$	-12.7	1, 9, 1
AndI	00:45:39.8	+38:02:28	$0.791 \pm 0.050$	-12.0	1, 9, 1
AndXXXI	22:58:16.3	+41:17:28	$0.794_{0.013}^{0.018}$	-11.8	1, 8, 1
AndIII	00:35:33.8	+36:29:52	$0.745 \pm 0.039$	-10.2	1, 9, 1
$AndXXIII^*$	01:29:21.8	+38:43:8	$0.809_{0.01}^{0.022}$	-9.9	1, 8, 1
AndVI	23:51:46.3	+24:34:57	$0.783 \pm 0.025$	-11.5	1, 4, 1
AndXXI*	23:54:47.7	+42:28:15	$0.851_{0.011}^{0.019}$	-9.2	1, 8, 1
$And XXV^*$	00:30:8.9	+46:51:7	$0.832_{0.015}^{0.021}$	-9.2	1, 8, 1
LGS3	01:3:55.0	+21:53:6	$0.769 \pm 0.023$	-10.1	1, 4, 1
AndXV	01:14:18.7	+38:7:3	$0.766 \pm 0.042$	-8.4	1, 9, 1
AndV	01:10:17.1	+47:37:41	$0.774 \pm 0.028$	-9.5	1, 4, 1
$AndXIX^*$	00:19:32.1	+35:2:37	0.805	-10.1	1, 2, 1
$AndXIV^*$	00:51:35.0	+29:41:49	$0.847_{0.015}^{0.021}$	-8.8	1, 8, 1
AndXVII	00:37:7.0	+44:19:20	$0.866_{0.013}^{0.025}$	-8.1	1, 8, 1
AndXXIX	23:58:55.6	+30:45:20	$0.820_{0.015}^{0.017}$	-8.5	1, 8, 1
$AndIX^*$	00:52:53.0	+43:11:45	$0.769_{0.012}^{0.021}$	-8.8	1, 8, 1
AndXXX	00:36:34.9	+49:38:48	$0.628_{0.015}^{0.016}$	-8.	1, 8, 1
AndXXIV	01:18:30.0	+46:21:58	$0.724_{0.081}^{0.099}$	-8.0	1, 8, 1
AndXXXIII	03:1:23.6	+40:59:18	$0.755_{0.009}^{0.018}$	-10.2	1, 8, 1
AndXXVIII	22:32:41.2	+31:12:58	$0.769 \pm 0.038$	-8.8	1, 9, 1
AndXVIII	00:2:14.5	+45:5:20	$1.219_{0.013}^{0.029}$	-9.2	1, 8, 1

Note. Known satellites of M31 with  $M_V < -8$ . Satellites marked with \* are below the  $\mu_{0,V} = 26.5$  mag arcsec<sup>-2</sup> surface brightness limit we assume throughout this work. For the distances without error bars, Conn et al. (2012) provides the entire distance posterior, which is what is used. For these cases, the median distance is reported. Sources for position, distance, and luminosity (in order): (1) McConnachie et al. (2018), (2) Conn et al. (2012), (3) Sick et al. (2015), (4) McConnachie et al. (2005), (5) Watkins et al. (2013), Tonry et al. (2001), Jensen et al. (2003), Monachesi et al. (2011), Sarajedini et al. (2012), Fiorentino et al. (2012), (6) Sanna et al. (2008), (7) Richardson et al. (2011), (8) Weisz et al. (2019), (9) Martínez-Vázquez et al. (2017).

Table 26 M81 Satellites

M81, $M_* = 5 \times 10^{10} M_{\odot}$ (Cook et al. 2014)						
Name	R.A. (deg)	Decl. (deg)	$D_{\odot}$ (Mpc)	$M_V$	Source	
M81	09:55:33.2	+69:03:55	3.69	-21.1	1, 3, 2	
M82	09:55:52.4	+69:40:47	3.61	-19.75	1, 3, 2	
NGC 3077	10:03:19.1	+68:44:02	3.82	-17.93	1, 3, 2	
NGC 2976	09:47:15.5	+67:54:59	3.66	-17.83	1, 3, 2	
IC 2574	10:28:23.6	+68:24:43	3.93	-17.19	1, 3, 2	
DDO 82	10:30:36.58	+70:37:06	3.93	-15.06	1, 3, 2	
KDG 61	9:57:02.7	+68:35:30	3.66	-13.4	1, 3, 4	
BK5N	10:04:40.3	+68:15:20	3.70	-11.23	1, 3, 4	
IKN	10:08:05.9	+68:23:57	3.75	-14.3	1, 3, 4	
FM1	9:45:10.0	+68:45:54	3.78	-11.3	1, 3, 1	
KDG 64	10:07:01.9	+67:49:39	3.75	-13.3	1, 3, 4	
F8D1	09:44:47.1	+67:26:19	3.75	-12.8	1, 3, 1	
d0944p69	09:44:22.5	+69:12:40	3.84	-6.4	1, 3, 1	
d1014p68*	10:14:55.8	+68:45:27	3.84	-9.0	1, 3, 1	
KK77	9:50:10.0	+67:30:24	3.80	-12.6	1, 3, 1	
d1006p67	10:06:46.2	+67:12:04	3.61	-9.4	1, 3, 1	
d0939p71	09:39:15.9	+71:18:42	3.65	-9.0	1, 3, 1	
KDG 63	10:05:07.3	+66:33:18	3.65	-12.6	1, 3, 1	
d0958p66	09:58:48.5	+66:50:59	3.82	-12.8	1, 3, 1	
ddo78	10:26:27.9	+67:39:24	3.48	-12.4	1, 3, 1	
d1028p70	10:28:39.7	+70:14:01	3.84	-12.0	1, 3, 1	
d1015p69	10:15:06.9	+69:02:15	4.07	-8.4	1, 3, 1	
d0955p70*	09:55:13.6	+70:24:29	3.45	-9.4	1, 3, 1	
d1041p70	10:41:16.8	+70:09:03	3.70	-8.9	1, 3, 1	
HS117	10:21:25.2	+71:06:58	3.96	-11.7	1, 3, 1	
d0944p71	09:44:34.4	+71:28:57	3.47	-12	1, 3, 1	
d1012p64	10:12:48.4	+64:06:27	3.7	-12.9	1, 3, 1	
d0926p70	09:26:27.9	+70:30:24	3.4	-9.4	1, 3, 1	
Ho1	09:40:32.3	+71:11:11	4.02	-14.2	1, 3, 1	
BK6N	10:34:31.9	+66:00:42	3.31	-11.3	1, 3, 1	
d0934p70	09:34:03.7	+70:12:57	3.02	-9.0	1, 3, 1	

**Note.** Known satellites of M81. Satellites marked with \* are below the  $\mu_{0,V} = 26.5$  mag arcsec<sup>-2</sup> surface brightness limit we assume throughout this work. Sources for position, distance, and luminosity (in order): (1) Chiboucas et al. (2013), (2) Gil de Paz et al. (2007), (3) Karachentsev et al. (2013), (4) Okamoto et al. (2019).

Table 27 CenA Satellites

CenA, $M_* = 8 \times 10^{10} M_{\odot}$ (Karachentsev & Kudrya 2014)					
Name	R.A. (deg)	Decl. (deg)	$D_{\odot}$ (Mpc)	$M_V$	Source
CenA	201.3650	-43.0191	3.77	-21.04	1, 1, 1
KK189	198.1875	-41.8319	4.23	-11.2	1, 1, 1
ESO269-066	198.2875	-44.8900	3.75	-14.1	1, 1, 1
NGC 5011C	198.2958	-43.2656	3.73	-13.9	1, 1, 1
CenA-Dw11	199.4550	-42.9269	$3.52\pm0.35$	-9.4	2, 2, 2
CenA-Dw5	199.9667	-41.9936	$3.61 \pm 0.33$	-8.2	2, 2, 2
KK196	200.4458	-45.0633	3.96	-12.5	1, 1, 1
KK197	200.5042	-42.5356	3.84	-12.6	1, 1, 1
KKs55	200.5500	-42.7308	3.85	-12.4	1, 1, 1
CenA-Dw10*	200.6214	-39.8839	$3.27 \pm 0.44$	-7.8	2, 2, 2
dw1322-39	200.6558	-39.9084	$2.95 \pm 0.05$	-10.0	1, 1, 1
CenA-Dw4	200.7583	-41.7861	$4.09 \pm 0.26$	-9.9	2, 2, 2
dw1323-40b	201.0000	-40.8367	$3.91 \pm 0.6$	-9.9	1, 1, 1
dw1323-40	201.2421	-40.7622	$3.73 \pm 0.15$	-10.4	1, 1, 1
CenA-Dw6	201.4875	-41.0942	$4.04 \pm 0.20$	-9.1	2, 2, 2
CenA-Dw7	201.6167	-43.5567	$4.11 \pm 0.27$	-9.9	2, 2, 2
ESO324-024	201.9042	-41.4806	3.78	-15.5	1, 1, 1
KK203	201.8667	-45.3525	3.78	-10.5	1, 1, 1
dw1329-45	202.3121	-45.1767	$2.90 \pm 0.12$	-8.4	1, 1, 1
CenA-Dw2	202.4875	-41.8731	$4.14 \pm 0.23$	-9.7	2, 2, 2
CenA-Dw1	202.5583	-41.8933	$3.91 \pm 0.12$	-13.8	2, 2, 2
CenA-Dw3	202.5875	-42.19255	$3.88 \pm 0.16$	-13.1	2, 2, 2
CenA-Dw9*	203.2542	-42.5300	$3.81 \pm 0.36$	-9.1	2, 2, 2
CenA-Dw8*	203.3917	-41.6078	$3.47 \pm 0.33$	-9.7	2, 2, 2
dw1336-44	204.2033	-43.8578	$3.50 \pm 0.28$	-8.6	1, 1, 1
NGC5237	204.4083	-42.8475	3.33	-15.3	1, 1, 1
KKs57	205.4083	-42.5819	3.83	-10.6	1, 1, 1
dw1341-43	205.4221	-44.4485	$3.53 \pm 0.02$	-10.1	1, 1, 1
dw1342-43	205.7029	-43.8561	$2.90 \pm 0.14$	-9.8	1, 1, 1
KK213	205.8958	-43.7692	3.77	-10.0	1, 1, 1

**Note.** Known satellites of CenA. Satellites marked with \* are below the  $\mu_{0,V} = 26.5$  mag arcsec<sup>-2</sup> surface brightness limit we assume throughout this work. Sources for position, distance, and luminosity (in order): (1) Müller et al. (2019), (2) Crnojević et al. (2019).

Table 28 M101 Satellites

M101, $M_* = 4 \times 10^{10} M_{\odot}$ (Cook et al. 2014)						
Name	R.A. (deg)	Decl. (deg)	$D_{\odot}$ (Mpc)	$M_V$	Source	
M101	14:03:12.5	+54:20:56	$6.52 \pm 0.19$	-21.1	1, 3, 1	
NGC 5474	14:05:01.6	+53:39:44	$6.82 \pm 0.41$	-18.24	1, 1, 1	
NGC 5477	14:05:33.3	+54:27:40	$6.77 \pm 0.40$	-15.37	1, 1, 1	
HolmIV	13:54:45.7	+53:54:03	$6.93 \pm 0.48$	-15.98	1, 1, 1	
DF1	14:03:45.0	+53:56:40	$6.37 \pm 0.35$	-11.5	5, 5, 5	
DF2	14:08:37.5	+54:19:31	$6.87 \pm 0.26$	-10.4	5, 5, 5	
DF3	14:03:05.7	+53:36:56	$6.52 \pm 0.26$	-10.1	5, 5, 5	
dwa	14:06:49.9	+53:44:30	$6.83 \pm 0.27$	-9.5	2, 4, 4	
dw9	13:55:44.8	+55:08:46	$7.34 \pm 0.38$	-8.2	2, 4, 4	
UGC8882	13:57:14.7	+54:06:03	$7.0\pm0.5$	-14.59	6, 6, 6	

**Note.** Known satellites of M101. Sources for position, distance, and luminosity (in order): (1) Tikhonov et al. (2015), (2) Bennet et al. (2017), (3) Beaton et al. (2019), (4) Bennet et al. (2019), (5) Danieli et al. (2017), (6) current work.

**Table 29** M94 Satellites

M94, $M_* = 3 \times 10^{10} M_{\odot}$ (Cook et al. 2014)						
Name	R.A. (deg)	Decl. (deg)	$D_{\odot}$ (Mpc)	$M_V$	Source	
M94	12:50:53.1	+41:07:13	4.2	-19.95	1, 1, 2	
dw1 dw2	12:55:02.5 12:51:04.4	+40:35:22 +41:38:10	$4.1 \pm 0.2$ $4.7 \pm 0.3$	-10.1 $-9.7$	3, 3, 3 3, 3, 3	

**Note.** Known satellites of M94. Sources for position, distance, and luminosity (in order): (1) Karachentsev et al. (2013), (2) Gil de Paz et al. (2007), (3) Smercina et al. (2018).

# Appendix D Extrapolation of TNG to Lower-mass Subhalos

As mentioned in the main text, the resolution of TNG is fully adequate for use with the fiducial (low-scatter) SHMR but is not for the alternative, high-scatter SHMR. In this section, we

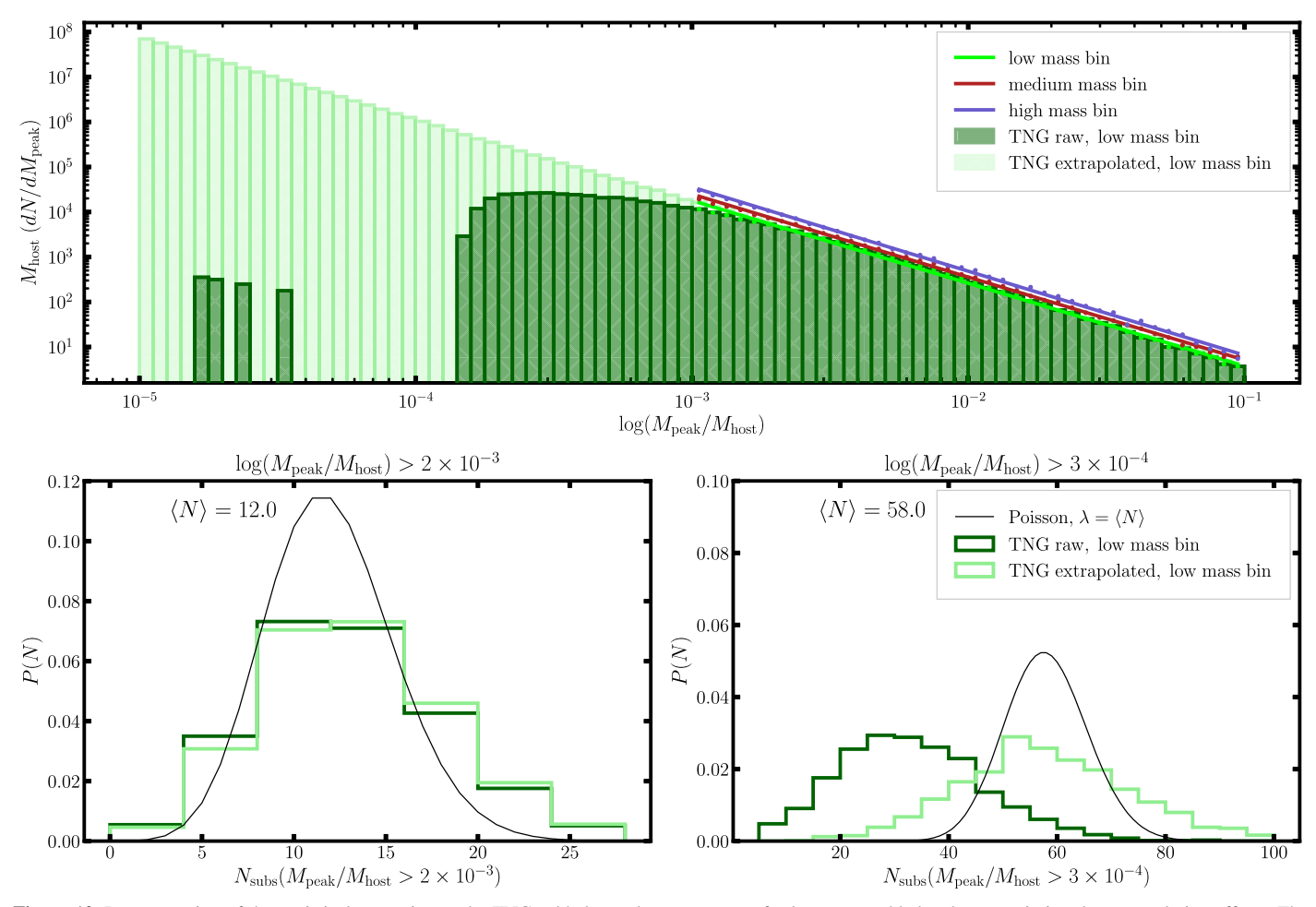


Figure 12. Demonstration of the statistical correction to the TNG subhalo catalogs to account for low-mass subhalos that are missing due to resolution effects. The host halos are split into three bins in halo mass, as described in the text. The top panel shows the subhalo mass function of the TNG subhalos of hosts in the low-mass bin, showing that resolution starts to be inadequate around subhalo masses of  $M_{\text{peak}}/M_{\text{host}} \lesssim 10^{-3}$ . The subhalo mass functions are fit with power laws, which are shown for each of the three bins. These power laws are used to extrapolate the subhalo mass function to lower subhalo masses, by inserting subhalos statistically. The bottom plots show the distributions of subhalo abundance for different hosts in different subhalo mass ranges. On the right, when including low-mass subhalos, the "patched" TNG catalog shows many more subhalos than the raw catalog and also demonstrates the super-Poisson host-to-host scatter.

describe our method for "patching" the TNG subhalo catalogs, effectively correcting them for inadequate resolution. This is done by extrapolating the SMF to lower masses than is possible from the *n*-body results. The process is shown in Figure 12.

We first collect a list of all host halos that are considered in the various comparisons we do throughout the paper, including all of the different matched stellar mass comparisons to the individual observed hosts. To account for the fact that the SMF mildly depends on the host halo mass (Gao et al. 2004; Giocoli et al. 2008), with more massive hosts having a higher SMF, we divide these hosts into three mass bins. These mass bins are chosen so that they each account for roughly one-third of the hosts. They have median host halo masses of 0.7, 1.3, and  $3.5 \times 10^{12} M_{\odot}$ . The top panel of Figure 12 shows the raw SMF for the low-mass bin of hosts scaled by the mass of the host, using the peak (i.e., accreted) subhalo masses. We include all subhalos within 2 virial radii of the hosts. We do this because we take a generous LOS distance cut when selecting subhalos to compare with observations, meaning that we need to patch the TNG subhalo catalog not just within the virial

radius of the hosts, but also in the surrounding area. The fact that the SMF is a power law with slope  $\sim$ -1.9 is a standard result of *n*-body simulations (e.g., Springel et al. 2008). It is clear that resolution starts to cause a deviation from the power law around subhalo masses of  $M_{\text{most}}/M_{\text{host}} \leq 10^{-3}$ .

law around subhalo masses of  $M_{\rm peak}/M_{\rm host} \lesssim 10^{-3}$ . To characterize the SMF, we fit a power law in the mass range  $10^{-3} < M_{\rm peak}/M_{\rm host} < 10^{-1}$  to each of the host bins. We then use this power law to predict the expected number of subhalos in the mass range  $10^{-5} < M_{\rm peak}/M_{\rm host} < 10^{-1}$ . We account for the fact that the host-to-host scatter in subhalo abundance is super-Poissonian (Boylan-Kolchin et al. 2010; Lu et al. 2016) by drawing a random number out of a negative binomial distribution using the parameters given in Boylan-Kolchin et al. (2010) for each host representing the actual number of subhalos in this mass range for that host. With this in hand, we count the current number of subhalos in the catalog in this mass range for each host. The difference between these gives the number of subhalos that need to be added to the catalogs. For each of these subhalos, a mass is drawn from a distribution derived from the difference between the expected and raw TNG SMF. In this way, the added subhalos, combined with the raw catalog, will exhibit the expected SMF. The subhalos are placed randomly around the host at a 3D radius drawn from the ensemble of radial separations of catalog

<sup>&</sup>lt;sup>19</sup> Note that since we often select hosts based on *stellar* mass, not halo mass, the low- and high-mass bins have significant tails to low and high halo masses, respectively.

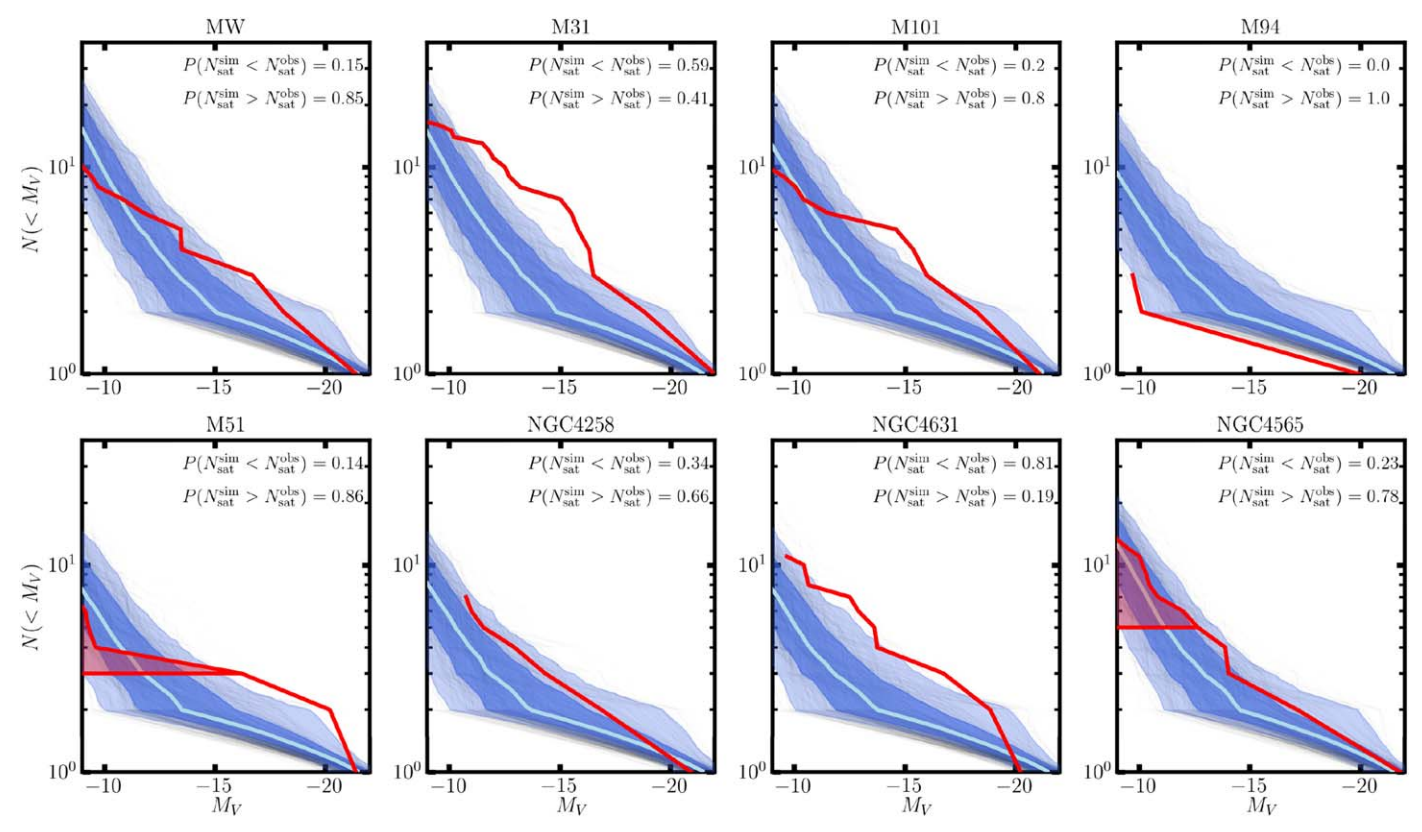


Figure 13. Cumulative luminosity functions for the eight "MW-sized" hosts that have been well surveyed for satellites (red). The thin black lines show the predicted LFs from the abundance matching model described in the text combined with the ELVIS zoom DMO simulation. The ELVIS hosts have halo masses in the range  $1-3\times10^{12}~M_{\odot}$ . The blue regions show the  $\pm$  1,  $2\sigma$  spread in the models. The luminosity completeness is different for each host but is  $M_V\lesssim-9$  in all cases. For each host, the model satellite systems have been forward modeled considering the survey area selection function for that specific host.

subhalos in each host mass bin. This way the inserted subhalos will exhibit the same radial distribution as the raw catalog subhalos (implicitly assuming that the radial distribution does not change with subhalo mass).

The resulting SMF for the low-mass hosts is shown in the top panel of Figure 12, where it is seen as an accurate extrapolation of the power-law fit from the TNG catalogs. The host-to-host scatter in subhalo abundance among the low-mass hosts is shown in the bottom panels. On the left, the abundance of subhalos above  $M_{\rm peak}/M_{\rm host} > 2 \times 10^{-3}$  is shown for both the original and patched TNG catalogs. In this mass range, the expected number of subhalos is 12, and the two distributions are both similar to each other and to a Poisson distribution with a mean of 12. On the right, the abundance of subhalos above  $M_{\rm peak}/M_{\rm host} > 3 \times 10^{-4}$  is shown. In this case, the patched catalog shows significantly more subhalos and exhibits a significantly super-Poisson variance, as expected.

## Appendix E Luminosity Function Checks with the ELVIS Simulation Suite

Figure 13 shows the analogous plot to Figure 5 for the ELVIS (Garrison-Kimmel et al. 2014) zoom DMO simulation. The observed "MW-sized" host satellite systems are compared with those predicted by the ELVIS DMO simulations combined with our fiducial SHMR and a prescription for disruption by a central disk from Samuel et al. (2020). We consider all ELVIS hosts here, which are evenly distributed in halo mass between 1 and  $3\times 10^{12}~M_{\odot}$ . Note that this is quite different from the way we select TNG halos in the main text to

have roughly the same stellar mass as the observed LV hosts. The thin black lines show the predicted LFs for the ELVIS hosts mock-observed from a random direction and forward modeled through the survey area selection function for a specific host, as described in Section 8. For each of the 48 ELVIS hosts, 10 random directions are used.

The ELVIS LFs are somewhat richer in satellites than the LFs predicted by TNG using the same SHMR. As explained in the main text, this is because the ELVIS hosts are, on average, more massive than the TNG "MW-like" hosts.

#### **ORCID iDs**

Scott G. Carlsten https://orcid.org/0000-0002-5382-2898
Annika H. G. Peter https://orcid.org/0000-0002-8040-6785
Rachael L. Beaton https://orcid.org/0000-0002-1691-8217
Johnny P. Greco https://orcid.org/0000-0003-4970-2874

#### References

Agertz, O., Pontzen, A., Read, J. I., et al. 2020, MNRAS, 491, 1656
Astropy Collaboration, Price-Whelan, A. M., Sipőcz, B. M., et al. 2018, AJ, 156, 123
Baldry, I. K., Driver, S. P., Loveday, J., et al. 2012, MNRAS, 421, 621
Barbary, K. 2016, JOSS, 1, 58
Beaton, R. L., Seibert, M., Hatt, D., et al. 2019, ApJ, 885, 141
Behroozi, P., Wechsler, R. H., Hearin, A. P., & Conroy, C. 2019, MNRAS, 488, 3143
Behroozi, P. S., Wechsler, R. H., & Conroy, C. 2013, ApJ, 770, 57
Bell, E. F., & de Jong, R. S. 2001, ApJ, 550, 212
Bellazzini, M., Ferraro, F. R., Origlia, L., et al. 2002, AJ, 124, 3222
Bellazzini, M., Gennari, N., & Ferraro, F. R. 2005, MNRAS, 360, 185
Bennet, P., Sand, D. J., Crnojević, D., et al. 2017, ApJ, 850, 109

```
Bennet, P., Sand, D. J., Crnojević, D., et al. 2019, ApJ, 885, 153
Bennet, P., Sand, D. J., Crnojević, D., et al. 2020, ApJL, 893, L9
Bertin, E. 2010, SWarp: Resampling and Co-adding FITS Images Together
   v2.38.0, Astrophysics Source Code Library, ascl:1010.068
Bertin, E., & Arnouts, S. 1996, A&AS, 117, 393
Bertin, E. 2006, in ASP Conf. Ser. 351, Astronomical Data Analysis Software
   and Systems XV, ed. C. Gabriel et al. (San Francisco, CA: ASP), 112
Blakeslee, J. P., Jordán, A., Mei, S., et al. 2009, ApJ, 694, 556
Bland-Hawthorn, J., & Gerhard, O. 2016, ARA&A, 54, 529
Bonanos, A. Z., Stanek, K. Z., Szentgyorgyi, A. H., Sasselov, D. D., &
   Bakos, G. Á. 2004, AJ, 127, 861
Bosch, J., Armstrong, R., Bickerton, S., et al. 2018, PASJ, 70, S5
Boulade, O., Charlot, X., Abbon, P., et al. 2003, Proc. SPIE, 4841, 72
Boylan-Kolchin, M., Bullock, J. S., & Kaplinghat, M. 2011, MNRAS,
Boylan-Kolchin, M., Bullock, J. S., & Kaplinghat, M. 2012, MNRAS,
   422, 1203
Boylan-Kolchin, M., Springel, V., White, S. D. M., & Jenkins, A. 2010,
   MNRAS, 406, 896
Bressan, A., Marigo, P., Girardi, L., et al. 2012, MNRAS, 427, 127
Brook, C. B., di Cintio, A., Knebe, A., et al. 2014, ApJL, 784, L14
Brooks, A. M., Kuhlen, M., Zolotov, A., & Hooper, D. 2013, ApJ, 765, 22
Buck, T., Macciò, A. V., Dutton, A. A., Obreja, A., & Frings, J. 2019,
          S, 483, 1314
Byun, W., Sheen, Y.-K., Park, H. S., et al. 2020, ApJ, 891, 18
Callingham, T. M., Cautun, M., Deason, A. J., et al. 2019, MNRAS, 484, 5453
Cantiello, M., Blakeslee, J. P., Ferrarese, L., et al. 2018, ApJ, 856, 126
Carlsten, S. G., Beaton, R. L., Greco, J. P., & Greene, J. E. 2019a, ApJL,
Carlsten, S. G., Beaton, R. L., Greco, J. P., & Greene, J. E. 2019b, ApJ, 879, 13
Carlsten, S. G., Greco, J. P., Beaton, R. L., & Greene, J. E. 2020a, ApJ, 891, 144
Carlsten, S. G., Greene, J. E., Peter, A. H. G., Greco, J. P., & Beaton, R. L.
   2020b, ApJ, 902, 124
Carlsten, S. G., Strauss, M. A., Lupton, R. H., Meyers, J. E., & Miyazaki, S.
   2018, MNRAS, 479, 1491
Carrera, R., Aparicio, A., Martínez-Delgado, D., & Alonso-García, J. 2002, AJ,
   123, 3199
Chiboucas, K., Jacobs, B. A., Tully, R. B., & Karachentsev, I. D. 2013, AJ,
Chiboucas, K., Karachentsev, I. D., & Tully, R. B. 2009, AJ, 137, 3009
Choi, J., Dotter, A., Conroy, C., et al. 2016, ApJ, 823, 102
Cohen, Y., van Dokkum, P., Danieli, S., et al. 2018, ApJ, 868, 96
Conn, A. R., Ibata, R. A., Lewis, G. F., et al. 2012, ApJ, 758, 11
Cook, D. O., Dale, D. A., Johnson, B. D., et al. 2014, MNRAS, 445, 881
Coppola, G., Marconi, M., Stetson, P. B., et al. 2015, ApJ, 814, 71
Crnojević, D., Sand, D. J., Bennet, P., et al. 2019, ApJ, 872, 80
Crnojević, D., Sand, D. J., Caldwell, N., et al. 2014, ApJ, 795, L35
Dalcanton, J. J., Spergel, D. N., Gunn, J. E., Schmidt, M., & Schneider, D. P.
   1997, AJ, 114, 635
Dalcanton, J. J., Williams, B. F., Seth, A. C., et al. 2009, ApJS, 183, 67
Danieli, S., van Dokkum, P., Merritt, A., et al. 2017, ApJ, 837, 136
Dey, A., Schlegel, D. J., Lang, D., et al. 2019, AJ, 157, 168
D'Onghia, E., Springel, V., Hernquist, L., & Keres, D. 2010, ApJ, 709, 1138
Errani, R., Peñarrubia, J., Laporte, C. F. P., & Gómez, F. A. 2017, MNRAS,
   465, L59
Erwin, P. 2015, ApJ, 799, 226
Fillingham, S. P., Cooper, M. C., Wheeler, C., et al. 2015, MNRAS, 454, 2039
Fiorentino, G., Contreras Ramos, R., Tolstoy, E., Clementini, G., & Saha, A.
   2012, A&A, 539, A138
Fitts, A., Boylan-Kolchin, M., Elbert, O. D., et al. 2017, MNRAS, 471, 3547
Fritz, T. K., Battaglia, G., Pawlowski, M. S., et al. 2018, A&A, 619, A103
Fukugita, M., Shimasaku, K., & Ichikawa, T. 1995, PASP, 107, 945
Gao, L., White, S. D. M., Jenkins, A., Stoehr, F., & Springel, V. 2004,
     INRAS, 355, 819
Garrison-Kimmel, S., Boylan-Kolchin, M., Bullock, J. S., & Lee, K. 2014,
   MNRAS, 438, 2578
Garrison-Kimmel, S., Bullock, J. S., Boylan-Kolchin, M., & Bardwell, E.
   2017a, MNRAS, 464, 3108
Garrison-Kimmel, S., Hopkins, P. F., Wetzel, A., et al. 2019, MNRAS,
  487, 1380
Garrison-Kimmel, S., Wetzel, A., Bullock, J. S., et al. 2017b, MNRAS,
Geha, M., Wechsler, R. H., Mao, Y.-Y., et al. 2017, ApJ, 847, 4
Gil de Paz, A., Boissier, S., Madore, B. F., et al. 2007, ApJS, 173, 185
Gilhuly, C., Hendel, D., Merritt, A., et al. 2020, ApJ, 897, 108
Giocoli, C., Tormen, G., & van den Bosch, F. C. 2008, MNRAS, 386, 2135
```

```
González, R. E., Kravtsov, A. V., & Gnedin, N. Y. 2014, ApJ, 793, 91
Graus, A. S., Bullock, J. S., Kelley, T., et al. 2019, MNRAS, 488, 4585
Greco, J. P., Greene, J. E., Strauss, M. A., et al. 2018, ApJ, 857, 104
Greco, J. P., van Dokkum, P., Danieli, S., Carlsten, S. G., & Conroy, C. 2020,
  arXiv:2004 07273
Gullieuszik, M., Held, E. V., Rizzi, L., et al. 2008, MNRAS, 388, 1185
Gwyn, S. D. J. 2012, AJ, 143, 38
Hamanowicz, A., Pietrukowicz, P., Udalski, A., et al. 2016, AcA, 66, 197
Hilditch, R. W., Howarth, I. D., & Harries, T. J. 2005, MNRAS, 357, 304
Huchtmeier, W. K., Karachentsev, I. D., & Karachentseva, V. E. 2009, A&A,
Irwin, J. A., Hoffman, G. L., Spekkens, K., et al. 2009, ApJ, 692, 1447
Jensen, J. B., Tonry, J. L., Barris, B. J., et al. 2003, ApJ, 583, 712
Jerjen, H. 2003, A&A, 398, 63
Jerjen, H., Binggeli, B., & Barazza, F. D. 2004, AJ, 127, 771
Jerjen, H., Freeman, K. C., & Binggeli, B. 1998, AJ, 116, 2873
Jerjen, H., Freeman, K. C., & Binggeli, B. 2000, AJ, 119, 166
Jerjen, H., Rekola, R., Takalo, L., Coleman, M., & Valtonen, M. 2001, A&A,
  380, 90
Karachentsev, I. D., & Kudrya, Y. N. 2014, AJ, 148, 50
Karachentsev, I. D., Makarov, D. I., & Kaisina, E. I. 2013, AJ, 145, 101
Karachentsev, I. D., Riepe, P., Zilch, T., et al. 2015, AstBu, 70, 379
Karunakaran, A., Spekkens, K., Zaritsky, D., et al. 2020, ApJ, 902, 39
Kelley, T., Bullock, J. S., Garrison-Kimmel, S., et al. 2019, MNRAS, 487, 4409
Kim, E., Kim, M., Hwang, N., et al. 2011, MNRAS, 412, 1881
Kim, S. Y., Peter, A. H. G., & Hargis, J. R. 2018, PhRvL, 121, 211302
Kinemuchi, K., Harris, H. C., Smith, H. A., et al. 2008, AJ, 136, 1921
Klypin, A., Kravtsov, A. V., Valenzuela, O., & Prada, F. 1999, ApJ, 522, 82
Kuehn, C., Kinemuchi, K., Ripepi, V., et al. 2008, ApJL, 674, L81
Leroy, A. K., Sandstrom, K. M., Lang, D., et al. 2019, ApJS, 244, 24
Liu, L., Gerke, B. F., Wechsler, R. H., Behroozi, P. S., & Busha, M. T. 2011,
      733, 62
Lu, Y., Benson, A., Mao, Y.-Y., et al. 2016, ApJ, 830, 59
Mao, Y.-Y., Geha, M., Wechsler, R. H., et al. 2020, arXiv:2008.12783
Marigo, P., Girardi, L., Bressan, A., et al. 2017, ApJ, 835, 77
Marinacci, F., Vogelsberger, M., Pakmor, R., et al. 2018, MNRAS, 480, 5113
Martin, N. F., Ibata, R. A., Lewis, G. F., et al. 2016, ApJ, 833, 167
Martin, N. F., Schlafly, E. F., Slater, C. T., et al. 2013a, ApJL, 779, L10
Martin, N. F., Slater, C. T., Schlafly, E. F., et al. 2013b, ApJ, 772, 15
Martínez-Delgado, D., D'Onghia, E., Chonis, T. S., et al. 2015, AJ, 150, 116
Martínez-Vázquez, C. E., Monelli, M., Bernard, E. J., et al. 2017, ApJ,
  850, 137
Martínez-Vázquez, C. E., Stetson, P. B., Monelli, M., et al. 2016, MNRAS,
  462, 4349
Mateo, M., Fischer, P., & Krzeminski, W. 1995, AJ, 110, 2166
McConnachie, A. W. 2012, AJ, 144, 4
McConnachie, A. W., Ibata, R., Martin, N., et al. 2018, ApJ, 868, 55
McConnachie, A. W., Irwin, M. J., Ferguson, A. M. N., et al. 2005, MNRAS,
   356, 979
McConnachie, A. W., Irwin, M. J., Ibata, R. A., et al. 2009, Natur, 461, 66
Mieske, S., Hilker, M., & Infante, L. 2006, A&A, 458, 1013
Mieske, S., Hilker, M., Infante, L., & Mendes de Oliveira, C. 2007, A&A, 463, 503
Monachesi, A., Trager, S. C., Lauer, T. R., et al. 2011, ApJ, 727, 55
Moore, B., Ghigna, S., Governato, F., et al. 1999, ApJ, 524, L19
Moster, B. P., Naab, T., & White, S. D. M. 2013, MNRAS, 428, 3121
Moster, B. P., Naab, T., & White, S. D. M. 2018, MNRAS, 477, 1822
Müller, O., Jerjen, H., & Binggeli, B. 2015, A&A, 583, A79
Müller, O., Jerjen, H., & Binggeli, B. 2017, A&A, 597, A7
Müller, O., Jerjen, H., & Binggeli, B. 2018, A&A, 615, A105
Müller, O., Rejkuba, M., Pawlowski, M. S., et al. 2019, A&A, 629, 18
Muñoz, R. R., Côté, P., Santana, F. A., et al. 2018, ApJ, 860, 66
Munshi, F., Brooks, A. M., Applebaum, E., et al. 2017, arXiv:1705.06286
Munshi, F., & Macri, L. 2007, BAAS, 39, 827
Nadler, E. O., Wechsler, R. H., Bechtol, K., et al. 2020, ApJ, 893, 48
Naiman, J. P., Pillepich, A., Springel, V., et al. 2018, MNRAS, 477, 1206
Nelson, D., Pillepich, A., Springel, V., et al. 2018, MNRAS, 475, 624
Nelson, D., Springel, V., Pillepich, A., et al. 2019, ComAC, 6, 2
Nierenberg, A. M., Treu, T., Menci, N., et al. 2016, MNRAS, 462, 4473
Ocvirk, P., Gillet, N., Shapiro, P. R., et al. 2016, MNRAS, 463, 1462
Okamoto, S., Arimoto, N., Ferguson, A. M. N., et al. 2019, ApJ, 884, 128
Okamoto, T., & Frenk, C. S. 2009, MNRAS, 399, L174
Okamoto, T., Gao, L., & Theuns, T. 2008, MNRAS, 390, 920
Park, H. S., Moon, D.-S., Zaritsky, D., et al. 2017, ApJ, 848, 19
Park, H. S., Moon, D.-S., Zaritsky, D., et al. 2019, ApJ, 885, 88
Peñarrubia, J., Ma, Y.-Z., Walker, M. G., & McConnachie, A. 2014, MNRAS,
  443, 2204
```

```
Pietrzyński, G., Gieren, W., Szewczyk, O., et al. 2008, AJ, 135, 1993
Pietrzyński, G., Graczyk, D., Gallenne, A., et al. 2019, Natur, 567, 200
Pillepich, A., Nelson, D., Hernquist, L., et al. 2018, MNRAS, 475, 648
Radburn-Smith, D. J., de Jong, R. S., Streich, D., et al. 2014, ApJ, 780, 105
Read, J. I., & Erkal, D. 2019, MNRAS, 487, 5799
Read, J. I., Iorio, G., Agertz, O., & Fraternali, F. 2017, MNRAS, 467, 2019
Rekola, R., Jerjen, H., & Flynn, C. 2005, A&A, 437, 823
Richardson, J. C., Irwin, M. J., McConnachie, A. W., et al. 2011, ApJ, 732, 76
Rizzi, L., Held, E. V., Saviane, I., Tully, R. B., & Gullieuszik, M. 2007,
    INRAS, 380, 1255
Rodríguez-Puebla, A., Primack, J. R., Avila-Reese, V., & Faber, S. M. 2017,
      RAS, 470, 651
Sabbi, E., Calzetti, D., Ubeda, L., et al. 2018, ApJS, 235, 23
Sales, L. V., Wang, W., White, S. D. M., & Navarro, J. F. 2013, MNRAS,
  428, 573
Samuel, J., Wetzel, A., Tollerud, E., et al. 2020, MNRAS, 491, 1471
Sanna, N., Bono, G., Stetson, P. B., et al. 2008, ApJL, 688, L69
Sarajedini, A., Yang, S. C., Monachesi, A., Lauer, T. R., & Trager, S. C. 2012,
   MNRAS, 425, 1459
Sawala, T., Frenk, C. S., Fattahi, A., et al. 2016a, MNRAS, 457, 1931
Sawala, T., Frenk, C. S., Fattahi, A., et al. 2016b, MNRAS, 456, 85
Schaye, J., Crain, R. A., Bower, R. G., et al. 2015, MNRAS, 446, 521
Sérsic, J. L. 1963, BAAA, 6, 41
Sharina, M. E., Karachentsev, I. D., & Tikhonov, N. A. 1999, AstL, 25, 322
Sick, J., Courteau, S., Cuillandre, J.-C., et al. 2015, in IAU Symp. 311, Galaxy
   Masses as Constraints of Formation Models, ed. M. Cappellari &
   S. Courteau (Cambridge: Cambridge Univ. Press), 82
```

```
Smercina, A., Bell, E. F., Price, P. A., et al. 2018, ApJ, 863, 152
Spencer, M., Loebman, S., & Yoachim, P. 2014, ApJ, 788, 146
Springel, V., Pakmor, R., Pillepich, A., et al. 2018, MNRAS, 475, 676
Springel, V., Wang, J., Vogelsberger, M., et al. 2008, MNRAS, 391, 1685
Stetson, P. B., Fiorentino, G., Bono, G., et al. 2014, PASP, 126, 616
Tanaka, M., Chiba, M., & Komiyama, Y. 2017, ApJ, 842, 127
Tikhonov, N. A., Lebedev, V. S., & Galazutdinova, O. A. 2015, AstL, 41, 239
Tinker, J., Kravtsov, A. V., Klypin, A., et al. 2008, ApJ, 688, 709
Tollerud, E. J., Boylan-Kolchin, M., Barton, E. J., Bullock, J. S., &
  Trinh, C. Q. 2011, ApJ, 738, 102
Tonry, J. L., Dressler, A., Blakeslee, J. P., et al. 2001, ApJ, 546, 681
Trentham, N., & Tully, R. B. 2009, MNRAS, 398, 722
Vivas, A. K., & Mateo, M. 2013, AJ, 146, 141
Walterbos, R. A. M., & Kennicutt, R. C. J. 1987, A&AS, 69, 311
Wang, W., & White, S. D. M. 2012, MNRAS, 424, 2574
Watkins, L. L., Evans, N. W., & An, J. H. 2010, MNRAS, 406, 264
Watkins, L. L., Evans, N. W., & van de Ven, G. 2013, MNRAS, 430, 971
Watkins, L. L., van der Marel, R. P., Sohn, S. T., & Evans, N. W. 2019, ApJ,
  873, 118
Weisz, D. R., Dolphin, A. E., Martin, N. F., et al. 2019, MNRAS, 489, 763
Wetzel, A. R., Hopkins, P. F., Kim, J.-h., et al. 2016, ApJL, 827, L23
Wheeler, C., Hopkins, P. F., Pace, A. B., et al. 2019, MNRAS, 490, 4447
Woo, J., Courteau, S., & Dekel, A. 2008, MNRAS, 390, 1453
Woodley, K. A. 2006, AJ, 132, 2424
Zhang, D., Luo, Y., & Kang, X. 2019, MNRAS, 486, 2440
Zschaechner, L. K., Rand, R. J., Heald, G. H., Gentile, G., & Józsa, G. 2012,
   ApJ, 760, 37
```